THE UNIVERSITY OF MELBOURNE

Department of Infrastructure Engineering

Ocean Engineering

DETERMINATION OF OCEANIC EXTREMES USING A SPATIAL ENSEMBLE OF SATELLITE DATA

by

Alicia Takbash

ORCID ID: 0000-0001-7024-0286

Principal supervisor

Prof. Ian R. Young

Submitted in total fulfilment of the requirements of the degree of

Doctor of Philosophy

February 2020

Abstract

In this thesis, the application of extreme-value analysis to long-duration (30-year) global altimeter and radiometer datasets is considered. In contrast to previous extreme-value analyses of satellite data, the dataset is sufficiently long to enable a Peaks over Threshold (PoT) analysis to be undertaken. When applied to altimeter data for wind speed and significant wave height, this analysis produces values consistent with buoy validation data and previous numerical model reanalysis datasets. The spatial distributions produced are also consistent with the model reanalysis data. However, the altimeter data shows a much greater fine-scale structure for wind speed, which is consistent with known tropical cyclone activity. Nevertheless, these results still show spatial variability of estimates as a result of relatively high statistical variability.

The greater data density provided by radiometer measurements offers the potential to address altimeter under-sampling. However, issues associated with the radiometer's inability to measure wind speed in heavy rain events appears to create an unacceptable "fair-weather" bias at extreme wind speeds. This renders the radiometer data of wind speed largely unusable for the investigation of wind speed extremes. The study also clearly demonstrates the limitations of the Initial Distribution Method (IDM) for extreme-value analysis, which is heavily biased by mean conditions.

Based on these outcomes, the aim was to investigate approaches to reduce potential errors and the size of confidence intervals on the resulting estimates of extremes when applying the PoT approach to altimeter data. Therefore, a novel approach to the estimation of extreme-value ocean significant wave height is investigated, in which data from adjacent regions are pooled to form a spatial ensemble. The equivalent duration of this ensemble region is the sum of the duration of the data pooled to form the ensemble. To create such a spatial ensemble, data from regions to be pooled must be independent and identically distributed.

ERA-Interim ["ERA" refers to ECMWF (European Centre for Medium-Range Weather Forecasts) ReAnalysis] global atmospheric reanalysis data are used to investigate the requirement of independent and identically distributed data on a global basis. As a result, typical spatial ensembles are defined for 18 regions of the world, and the 100-yr return period significant wave height is calculated for these regions. It is shown that the method can result in a reduction in the confidence interval for such extreme-value estimates of between 30% and 60%. The method is demonstrated both with ERA-Interim data and altimeter data.

Declaration

I, Alicia Takbash, hereby declare that:

(i) This submission comprises only my original work towards the degree of Doctor of Philosophy except where indicated in the Preface;

(ii) Due acknowledgement has been made in the text to all other material used;

(iii) The thesis is fewer than 100,000 words in length, exclusive of tables, figures/maps, bibliographies and appendices.

Alicia Takbash *14^{th} February, 2020*

Preface

This thesis has been written in the Department of Infrastructure Engineering, at The University of Melbourne. A stipend, The Graduate Research Scholarship, has been provided by The University of Melbourne to complete this work.

The chapters declared below are based on manuscripts that are published or under review for publication. I declare that I am the primary author and have contributed 80% to each of these papers.

Chapter 1 is based on the following papers:

1) Takbash, A., Young, I. R., and Breivik, Ø. (2019). Global wind speed and wave height extremes derived from long-duration satellite records. *Journal of Climate*, 32(1):109–126. `https://doi.org/10.1175/JCLI-D-18-0520.1`. **© American Meteorological Society. Used with permission.**

2) Takbash, A. and Young, I. R. (2019). Global Ocean Extreme Wave Heights from Spatial Ensemble Data. *Journal of Climate*, 32(20):6823–6836. `https://doi.org/10.1175/JCLI-D-19-0255.1`. **© American Meteorological Society. Used with permission.**

Chapter 2 is based on the following papers:

1) Takbash, A., Young, I. R., and Breivik, Ø. (2019). Global wind speed and wave height extremes derived from long-duration satellite records. *Journal of Climate*, 32(1):109–126. `https://doi.org/10.1175/JCLI-D-18-0520.1`. **© American Meteorological Society. Used with permission.**

2) Takbash, A. and Young, I. R. (2019). Global Ocean Extreme Wave Heights from Spatial Ensemble Data. *Journal of Climate*, 32(20):6823–6836. `https://doi.org/10.1175/JCLI-D-19-0255.1`. **© American Meteorological Society. Used with permission.**

Chapter 3 is based on the following paper:

1) Takbash, A., Young, I. R., and Breivik, Ø. (2019). Global wind speed and wave height extremes derived from long-duration satellite records. *Journal of Climate*, 32(1):109–126. https://doi.org/10.1175/JCLI-D-18-0520.1. **© American Meteorological Society. Used with permission.**

Chapter 4 is based on the following paper:

1) Takbash, A., Young, I. R., and Breivik, Ø. (2019). Global wind speed and wave height extremes derived from long-duration satellite records. *Journal of Climate*, 32(1):109–126. https://doi.org/10.1175/JCLI-D-18-0520.1. **© American Meteorological Society. Used with permission.**

Chapter 5 is based on the following paper:

1) Takbash, A., Young, I. R., and Breivik, Ø. (2019). Global wind speed and wave height extremes derived from long-duration satellite records. *Journal of Climate*, 32(1):109–126. https://doi.org/10.1175/JCLI-D-18-0520.1. **© American Meteorological Society. Used with permission.**

Chapter 6 is based on the following paper:

1) Takbash, A. and Young, I. R. (2019). Global Ocean Extreme Wave Heights from Spatial Ensemble Data. *Journal of Climate*, 32(20):6823–6836. https://doi.org/10.1175/JCLI-D-19-0255.1. **© American Meteorological Society. Used with permission.**

Chapter 7 is based on the following papers:

1) Takbash, A., Young, I. R., and Breivik, Ø. (2019). Global wind speed and wave height extremes derived from long-duration satellite records. *Journal of Climate*, 32(1):109–126. https://doi.org/10.1175/JCLI-D-18-0520.1. **© American Meteorological Society. Used with permission.**

2) Takbash, A. and Young, I. R. (2019). Global Ocean Extreme Wave Heights from Spatial Ensemble Data. *Journal of Climate*, 32(20):6823–6836. https://doi.org/10.1175/JCLI-D-19-0255.1.

Acknowledgments

~ To myself.

~ To my primary supervisor Prof. Ian Young:
Ian, thank you for all your support and guidance throughout my PhD candidature. Your way of supervising kept me always motivated and contributed to my personal and professional growth. I always enjoyed working with you as you have always provided a kind, respectful and pleasant working atmosphere. I couldn't have imagined a better supervisor for this process.

~ To my team at Research Computing Services:
I was fortunate to find this welcoming and supportive digital community at the very beginning of my PhD. I not only found support for mastering my digital research tool but was also privileged to work with this fantastic team and was trained to be able to teach and help other researchers. Thank you for enabling me to learn so much about myself, my abilities, my values and goals.

I also gratefully acknowledge the support of Prof. Alexander Babanin and A/Prof. Alessandro Toffoli during my candidature, especially during the PhD coursework.

I'm also grateful for my colleagues at the School of Engineering and the Climate College, as well as for friends and family members who have supported me during this time.

The raw altimeter and buoy datasets used in this work were supplied by Globwave and are archived on the Australian Ocean Data Network [(AODN), `https://portal.aodn.org.au/`]. The radiometer dataset was provided by Remote Sensing Systems (RSS). Without these public domain archives, this study would have been challenging.

A part of this research was undertaken using the High-Performance Computing (HPC) Facility hosted at the University of Melbourne:
Meade, B., Lafayette, L., Sauter, G., and Tosello, D. (2017). Spartan HPC-Cloud Hybrid: Delivering Performance and Flexibility. *University of Melbourne*. Online resource. `https://doi.org/10.4225/49/58ead90dceaaa`.
Without this facility, obtaining some of the results would have been demanding.

With appreciation,
Alicia Takbash

Contents

List of Symbols and Abbreviations

$\approx$	Approximately equal to.
cm yr^{-1}	Centimetre per annum.
cm s^{-1} yr^{-1}	Centimetre per second per annum.
$^\circ$	Decimal degree.
$^\circ$ N	Degrees at or north of the Equator (latitude in the Northern Hemisphere).
$^\circ$ S	Degrees at or south of the Equator (latitude in the Southern Hemisphere).
$^\circ$ E	Degrees east of the prime meridian (longitude).
h	Hour.
km h^{-1}	Kilometre per hour.
m s^{-1}	Metre per second.
H_s	The significant wave height.
H_s^{100}	The 100-yr return period significant wave height.
$\overline{H_s}$	Mean quantities of H_s that have been evaluated via various means.
$\pm$	Plus or minus.
$r(i,j)$	The sample correlation coefficient between points i and j.
$\overline{RPD}(i,j)$	The mean Relative Percentage Difference between locations i and j.
$RPD^{99}(i,j)$	The 99th percentile Relative Percentage Difference between locations i and j.

U_{10}	The 10-m surface wind speed.
U_{10}^{100}	The 100-yr return period wind speed.
yr	Year.

AMM	Annual Maximum Method.
AMSR-E	Advanced Microwave Scanning Radiometer - Earth Observing System.
AODN	Australian Ocean Data Network.
CE	Correlation Ellipses.
CI	Confidence Interval.
CL	Confidence Limit.
CMEMS	Copernicus Marine Environment Monitoring Service.
ECMWF	European Centre for Medium-Range Weather Forecasts.
Envisat	Environmental satellite.
ERA-	ECMWF ReAnalysis-.
ERAI	ERA-Interim.
ERM	Exact Repeat Misson.
ERS-	European Remote-Sensing Satellite-.
EVA	Extreme-Value Analysis.
EXP	EXPonential distribution.
FT-1	Fisher-Tippett Type 1.
Geosat	Geodetic satellite.
GEV	Generalized Extreme-Value distribution.
GFO	Geosat Follow-On.
GPD	Generalized Pareto Distribution.
IBTrACS	International Best Track Archive for Climate Stewardship.
IDM	Initial Distribution Method.
IID	Independent and Identically Distributed.

ITCZ	The Inter-Tropical Convergence Zone.
KNMI	The Royal Netherlands Meteorological Institute.
NDBC	The National Data Buoy Center.
NetCDF	Network Common Data Form.
NOAA	National Oceanic and Atmospheric Administration.
PDF	Probability Distribution Function.
PoT	Peaks over Threshold.
QQ	Quantile-Quantile.
REMSS	REMote-Sensing Systems.
SAR	Synthetic-Aperture Radar.
SKIM	Sea surface KInematics Multiscale monitoring.
SSM/I	Special Sensor Microwave/Imager.
SWIM	Surface Waves Investigation and Monitoring.
TMI	The Tropical Rainfall Measuring Mission's (TRMM) Microwave Imager.
TOPEX	TOPographic EXperiment.
TRC	Tropical Cyclone Regions.
TS	Transformed-Stationary.
WAM	Wave Advanced Modelling.
WAVERYS	Global ocean WAVEs ReanalYsiS.
W3P	Weibull three-Parameter distribution.

List of Figures

List of Tables

Chapter 1

Introduction

The catastrophic impact of metocianic extreme events on coastlines, coastal and offshore structures, as well as commercial shipping loss can be reduced by improving the accuracy of the statistical estimates of oceanic extremes. In that sense, the most commonly used design parameters are the 10-m surface wind speed U_{10} and the significant wave height H_s (the average of the highest third of the waves). The determination of extreme-value estimates of environmental parameters such as wind speed and wave height is a common requirement for many coastal and offshore applications. In the present context "extreme-value" is used to describe the statistical estimate of the wind speed or wave height, which, for instance may be expected to be exceeded once in say 100 years. That is, the 100-yr return period wind speed U_{10}^{100} or wave height H_s^{100}. Alternatively, it can be described as the wind speed or wave height that has a probability of occurrence of 0.01 in any year.

The typical approach for the estimation of such extreme-value parameters is to analyse a long-duration [greater than 20 years (c.f., Vinoth, 2011; Vinoth and Young, 2011)] time series of measured wind speed or wave height. As the record is almost always shorter than the desired return period, the procedure used is to fit a chosen form for the Probability Distribution Function (PDF) to the recorded data and then extrapolate to the desired probability level (e.g., 0.01 for a 100-yr return level).

A number of practical challenges arise in this form of analysis. As the focus is on the extreme-value "tail" of the PDF, how well this part of the PDF is defined and how well the, often arbitrary, analytical form for the PDF fits the

data is critical. Obviously, it is desirable to reduce the extent of the required extrapolation of the PDF as much as possible. As a result, there is a strong requirement to have the longest measured time series possible at the location or locations of interest. Extrapolation is almost always required as the desired return period is longer than the data record. The accuracy of the extreme-value estimate is dependent on how well the chosen analytical PDF fits the low probability tail of the PDF of the recorded data and the extent of the extrapolation. To lessen the extrapolation and hence reduce the Confidence Limits (CLs) on the extreme-value estimate, the recorded time series should be as long as possible.

The most obvious approach to obtain long-duration measured records is to use buoy or fixed offshore platform data. Although suitable long-duration records exist at specific sites (Evans et al., 2003), the key shortcoming of such data is that it has very limited spatial distribution and hence is seldom at the location required. One approach to overcome both the temporal duration and spatial distribution issues is to use numerical model data. Indeed, long-duration reanalyses of wind speed and wave height, which include data assimilation from satellites, are available [e.g., ERA-40 (Uppala et al., 2005), superseded by ERA-Interim (Dee et al., 2011), which has been recently migrated to ERA-5 reanalysis (`https://www.ecmwf.int/en/forecasts/datasets/reanalysis-datasets/era5`); "ERA" refers to ECMWF (European Centre for Medium-Range Weather Forecasts) ReAnalysis]. In addition to ERA-5, the CMEMS (Copernicus Marine Environment Monitoring Service) global ocean WAVEs ReanalYsiS (WAVERYS) (`https://resources.marine.copernicus.eu/?option=com_csw&task=results?option=com_csw&view=details&product_id=GLOBAL_REANALYSIS_WAV_001_032`), and the NOAA (National Oceanic and Atmospheric Administration) WAVEWATCH III® hindcasts with reanalysis winds (`https://polar.ncep.noaa.gov/waves/hindcasts/nopp-phase2.php`) rank among the new products. Naturally, these datasets are only as good as the models used to produce them. Although present-day atmospheric circulation and surface wave models are remarkably reliable, for records longer than approximately 30 years, the quality of the wind fields forcing the model declines (Dee et al., 2011), and their performance under extreme conditions is still limited.

The advent of Earth-observing satellites has provided a long [approximately 30-year (Young et al., 2017; Ribal and Young, 2019)] record of global wind speed and wave height, and a number of previous studies (Alves and

Young, 2003; Vinoth, 2011; Vinoth and Young, 2011; Young et al., 2012) have examined the suitability of such data for Extreme-Value Analysis (EVA) or extreme trend analysis. Although these studies have shown potential, they highlight a number of issues with such data. These issues include the following: as data invariably come from multiple satellites, careful long-term calibrations are required; the datasets considered were not sufficiently long to apply statistically sound approaches to extrapolation of the PDF; there were questions about the extreme-value performance of such satellite systems; and the spatial separation of satellite ground tracks means that the radar altimeters used may under-sample extremes.

The first aim of the present study considers the examination of a long-term (almost 30-year) calibrated and validated dataset of wind speed and wave height obtained from both altimeter and radiometer systems (published in Takbash et al., 2019). As will be shown, the duration of the record is now such that the Peaks over Threshold (PoT) method can be used for EVA of the data. The resulting global distributions are consistent with the limited point measurements of extreme wind speeds and wave heights from buoys, as well as with numerical reanalyses. In addition, for the first time, global distributions clearly show dominant storm tracks and tropical cyclone activity. As radiometer systems simultaneously measure a broad swath of the ocean, they have the potential to significantly enhance the quantity of data available and hence address issues of perceived under-sampling. However, limitations in the performance of radiometer data when applied to EVA will also be highlighted.

Nevertheless, the Takbash et al. (2019) results still showed spatial variability of estimates as a result of relatively high statistical variability of these estimates (i.e. large confidence limits), which was examined by Takbash and Young (2019) using the case of global extreme wave height obtained from altimeter systems.

All such studies of altimeter wave height data divide the world into spatial regions (grids) and pool all altimeter data in each grid region. These grid regions are then considered as independent observation regions and EVA is applied independently for each region. This raises the question of whether it is possible to use multiple spatial regions to obtain greater confidence in the extreme-value estimates. Breivik et al. (2014) and Meucci et al. (2018) have

addressed a similar problem using forecast model data. These forecast models run multiple ensembles predicting the future sea state, each initiated with slightly different initial conditions. Under certain conditions, they show that data from these ensemble forecasts can be pooled, creating a synthesised data series, the equivalent length of which is longer than the length of the individual ensemble datasets.

The second aim of the present work is to consider the data as a spatial ensemble (published in Takbash and Young, 2019). Criteria are developed which identify regions which can be pooled to create effective data sets the equivalent length of which is longer than the 30-year record of the original data. As a result, confidence limits for the resulting estimates can be significantly reduced, resulting in greater statistical confidence in the values of H_s^{100}.

The thesis is organised as follows. Chapter 2 provides a brief review of extreme-value theory, previous studies of global extreme-value estimates and the statistical approaches adopted. The role of the confidence interval in such analyses will be considered here. This is followed in Chapter 3 by a description of the satellite dataset used in this work and its calibration, particularly under extreme conditions. Chapter 4 compares extreme-value estimates from the present satellite measurements with buoy observations. A discussion of global distributions of extreme-value wind speed and wave height using a variety of statistical techniques and both satellite data types (altimeter and radiometer) is provided in Chapter 5. Chapters 3-5 represent an expanded version of the material published in Takbash et al. (2019). Chapter 6 outlines criteria which must be met to form spatial ensembles of data. This chapter also provides results for the extreme-value estimates of significant wave height using such spatial ensembles, and a discussion of these results. The material in this chapter represents an expanded version of the material published in Takbash and Young (2019). Finally, conclusions are summarised and discussed in Chapter 7.

Chapter 2

Global estimates of extreme wind speed and wave height

A lack of long-term [greater than 20 years (Vinoth, 2011; Vinoth and Young, 2011)] data is a limiting factor (regarding the confidence interval) in extreme-value estimates for metoceanic parameters, such as U_{10} and H_s. Point measurements, such as buoy data, provide reliable long-term observations but are spatially poorly resolved (Table 2.1). Hence, it is common to use buoy data for calibration of other meteorological and oceanographic data platforms, or validation of metoceanic analyses using these platforms. Buoy data are used, for example, for validation of numerical model data (Caires and Sterl, 2005; Breivik et al., 2013, 2014; Ponce de León and Guedes Soares, 2014; Amrutha et al., 2016), for calibration of satellite data (Zieger et al., 2009; Young et al., 2017), or validation of satellite-based metoceanic analyses (Alves and Young, 2003; Vinoth, 2011; Vinoth and Young, 2011; Young et al., 2011). Numerical model data have the advantage of providing long-term datasets but are questionable as "random realizations of a realistic model climate" (Breivik et al., 2013). That is, the results are only as good as the physics used in the prediction model (model data as the source for estimation of global oceanic extreme-values is discussed in Section 2.2). Although model-based wave height data can be assessed against reliable satellite altimeter and buoy wave data, there exist limitations for the proper assessment of the wind data (Caires and Sterl, 2003; Dee et al., 2011). As Young et al. (2017) outline, altimeters potentially underestimate wind speed above 15 m s^{-1} because of under-sampled storm events due to an Exact Repeat Misson (ERM) of between 5 to 20 days, and separation between ground tracks of 100 to 400 km. Moreover, radiometers and scatterometers fail to measure wind

speed accurately in heavy rain as shown in Table 2.1. There is also evidence that buoys underestimate wind speed at high values (Bender et al., 2010; Young et al., 2017).

Despite the limitations of satellite measurements, the use of this data platform for U_{10} and H_s analyses is favoured in applications, such as global climatology (Young and Holland, 1996; Young, 1999; Kong et al., 2016), global trends (Young et al., 2011, 2012; Young and Ribal, 2019), extreme-value analysis (Cooper and Forristall, 1997; Alves and Young, 2003; Vinoth and Young, 2011) and composite analysis (Ponce de León and Bettencourt, 2019). However, once again, Young et al. (2015) point out that achieving reliable results depends on having sufficient quality data, i.e., a long-term calibrated and validated dataset. Such a dataset was provided by Young et al. (2017) [recently updated by Ribal and Young (2019)]. The mentioned data sources and their features are raised further in the following sections and chapters.

This chapter provides an overview of common methods used in EVA to estimate the 100-yr return level of environmental parameters (Section 2.1). Following this, Section 2.2 summarises previous studies dealing with the determination of global oceanic wave/wind extreme-values. The role of the confidence interval in such analyses will be outlined in Section 2.3 based on the estimate of global extreme wave height. The content of Chaper 2 is based on the publications Takbash et al. (2019) and Takbash and Young (2019).

Table 2.1: Data sources and features for wind speed and wave height observations [based on Young et al. (2012, 2015, 2017) and Young and Ribal (2019)].

Data source	Data type	Wave height	Wind speed	Duration of ime series	Scale
Satellite data	Altimeters	Yes	Yes (from σ_0)	Greater than 30 yrs	Global
	Scatterometers	–	Yes (+ wind direction)	Greater than 20 yrs	Global (wind speed not available in areas with heavy rain)
	Microwave Radiometers SSM/I	–	Yes	Greater than 20 yrs	Global (wind speed not available in areas with heavy rain)
	SAR	Yes (full direct. wave spectrum	Yes	Greater than 20 yrs (not presently compiled into a single database)	Global (low spatial and temporal resolution)
Model data	Reanalysis data from Wave Advanced Modelling (WAM) & WAVEWATCH Models	Yes	Yes	Up to 40 yrs	Global
Offshore in-situ data	Buoy networks	Yes	Yes	Greater than 30 yrs	Only at point locations
	Microseism	Yes	–	Greater than 50 yrs	Only at point locations
	Ships	Yes	Yes	Greater than 100 yrs	Confined to shipping routes (of variable quality)
In-situ data	Anemometers	–	Yes		
	Accelerometers	Yes	–		

2.1 Extreme-value theory

As outlined by Goda (1988) and Coles (2001), the aim of EVA is to estimate the probability distribution of the extreme values of a variable from a record of empirical samples. To achieve valid estimates of the extremes, the data should be Independent and Identically Distributed (IID). For the present applications, the requirement of independence means that successive observed data points should be statistically uncorrelated. As a result, there should not be multiple data points associated with the same storm. As typical storms may have a duration of many hours, this means that successive data points may need to be separated by up to 48 hours to ensure independence (Lopatoukhin et al., 2000; Caires and Sterl, 2005; Vinoth and Young, 2011). The requirement to be identically distributed is satisfied when data points in a sample show a common parent distribution in a population. Should an area be subjected to quite different meteorological phenomena (e.g., trade winds and tropical cyclones), it is likely that these systems will have quite different PDFs and the data should be partitioned and each PDF considered separately (Vinoth and Young, 2011). It should be noted that as the present dataset does not provide a mechanism to separate independent storm climate systems, no attempt has been made to partition the data.

In ocean applications, the required return period for EVA is commonly 100 years (cf. Vinoth and Young, 2011; Breivik et al., 2014; Meucci et al., 2018). According to Jonathan and Ewans (2013), the required return period needs to be determined dependending on the application in marine design. Return periods of between 500 years and 10,000 years are applied in some cases; e.g., Van den Brink and Können (2011) have adopted a return period of 10,000 years for EVA of meteorological parameters using relatively short records. However, in the case of larger return periods, Bitner-Gregersen et al. (2014) emphasise the use of more extensive time series that are derived from numerical model data to extend the performance of EVA. Such datasets can be comparable to periods as long as 226 years (Breivik et al., 2013), 229 years (Breivik et al., 2014), or even 750 years (Meucci et al., 2018). The present study, however, relies on the formulated "rule of thumb" by Vinoth and Young (2011; based on Hogben (1988)), which implies that a reasonable extrapolation for EVA is possible to three times the length of the observation. Thus, it is expected that the choice of a return period of 100 years is compatible with the use of the satellite dataset of Young et al. (2017) (30 years of records) and will derive consistent results in

this work.

In wind/wave EVA applications, some studies [e.g., Jonathan et al. (2013); Ewans and Jonathan (2014); Mazas and Hamm (2017)] consider the estimation of joint extremes (that is, the probability of experiencing two or more extreme parameters together, e.g., extreme waves and extreme currents). In addition, the influence of dependency factors on extreme significant wave height and extreme wind speed can be investigated as well. For example, both the directionality of the sea state and the time of the year can impact the intensity of extreme significant wave height (Bitner-Gregersen et al., 2014). Hence, joint modelling (Jonathan et al., 2013; Ewans and Jonathan, 2014; Mazas and Hamm, 2017), and incorporating directionality and covariate effects (Jonathan et al., 2014; Jones et al., 2016; Randell et al., 2016) in EVA is a recommended practice. For these purposes, new satellite missions such as Sea surface KInematics Multiscale monitoring (SKIM) (Ardhuin et al., 2018) and Surface Waves Investigation and Monitoring (SWIM) (Hauser et al., 2017) projects that are providing detailed ocean wave properties are advantageous. However, such extensional extreme-value analyses are not considered in this work. This study examines the determination of extremes of single parameters, H_s^{100} and U_{10}^{100}.

There are three general approaches to EVA that have been used in wind/wave applications – the Initial Distribution Method (IDM; Goda, 1988, 1992; Ochi, 1992; Tucker, 1991; Lopatoukhin et al., 2000; Vinoth, 2011; Vinoth and Young, 2011), the Annual Maximum Method (AMM; Coles, 2001; Vinoth, 2011), and the PoT (Goda, 1992; Ferreira and Soares, 1998; Van Gelder and Vrijling, 1999; Alves and Young, 2003; Vinoth, 2011; Vinoth and Young, 2011). These methods will be discussed in the following subsections.

2.1.1 Initial Distribution Method (IDM)

The most obvious means of forming the PDF is to simply create a histogram of recorded wind/wave data. Such data, when obtained from in situ instruments, is typically measured at hourly (or 3 hourly) intervals. A parametric PDF can then be selected, fitted to the data, and extrapolated to the desired probability level $P(x < x^{100})$, where x can be either wind speed U_{10} or significant wave height H_s. For the present application $P(x < x^{100})$ represents the probability level associated with the 100-yr event (i.e., probability of exceedance of 0.01 in any year). For the IDM approach (Tucker, 1991; Cooper and Forristall, 1997;

Teng, 1998), $P(x < x^{100})$ is given by

$$P(x < x^{100}) = 1 - D/T_{100}, \tag{2.1}$$

where D is a decorrelation time scale in hours for observations of x, and T_{100} is the number of hours in 100 years. There is little theoretical guidance on the choice of the value for D. Studies using buoy data (Tucker, 1991; Cooper and Forristall, 1997; Teng, 1998) have usually adopted $D = 3$ hours, although it is almost certain that actual decorrelation scales for ocean waves are considerably longer. Rather, it seems that D might better be described as a calibration term. The empirical nature of the IDM extends beyond the choice of D. There is also no theoretical guidance in terms of the PDF that should be used to fit the data. Gumbel and Weibull distributions are often used, the ultimate choice being the form that best fits the observed PDF. The Gumbel distribution is defined as

$$F(x) = exp\left[-exp\left(-\frac{x-A}{B}\right)\right], \tag{2.2}$$

where $F(x)$ is the cumulative distribution function; the Weibull distribution takes the form

$$F(x) = 1 - exp\left[-\left(\frac{x-A}{B}\right)^{k}\right], \tag{2.3}$$

and k, A, and B are shape, location, and scale parameters, respectively.

According to Caires (2011), the standard numerical methods for the estimation of the parameters are the method of moments, method of probability-weighted moments and the maximum likelihood method, which is classified as a general and more flexible approach (Forbes et al., 2011; Mathiesen et al., 1994). However, it is recommended that the method is chosen based on the sample size of the variable and its tail distribution (i.e., there is no statistical theory). Based on Evans et al. (2000), Vinoth (2011) and Vinoth and Young (2011) apply the method of moments for parameter estimation, and hence use the term FT-1 (Fisher-Tippett Type 1; Fisher and Tippett, 1928) distribution instead of Gumbel distribution, which uses the maximum likelihood method for fitting. For a detailed statistical overview about parameter estimation of fitting models, see Embrechts et al. (1997), Goda (2010), and Vinoth (2011).

There are still further limitations with the IDM approach. First, in most

cases, the approach violates the requirement for independent and identically distributed data. When using in situ data measured at 1- or 3-h intervals, it is almost certain that such data are correlated. As the distribution is fitted to the full PDF, it is highly likely that data at the peak of the PDF (mean conditions) and that in the extreme tail (storms) will be from different meteorological events and hence not identically distributed. Finally, the fit of the chosen PDF to the data is always dominated by the bulk of the data, which is near the peak of the PDF, rather than the extreme tails where interest lies. Hence, the IDM tends to be an extrapolation of these more benign conditions than a model of the extremes. Despite these very significant shortcomings, the IDM has been extensively used (Goda, 1992, 1988; Tucker, 1991; Ochi, 1992), as it is the only alternative when only short time series are available (i.e., less than 15 years). In the case of Earth-observing satellites, the observational record has been so short that previous attempts at EVA have only yielded reasonable results when the IDM has been used (Alves and Young, 2003; Chen et al., 2004; Challenor et al., 2005; Wimmer et al., 2006; Vinoth and Young, 2011).

2.1.2 Annual Maximum Method (AMM)

One method to overcome the many limitations of the IDM approach is to use so-called block maxima. In this approach, the maximum value from a meteorologically appropriate period is considered, rather than all the data. The period might be a season or, more commonly, a year (the annual maximum). In such a case, it can be shown that these maxima will follow a Generalized Extreme-Value (GEV) distribution (Castillo, 1988; Coles, 2001):

$$F(x) = exp\left\{-\left[1 + k\left(\frac{x - A}{B}\right)\right]^{-1/k}\right\}. \tag{2.4}$$

Depending on the value of the shape parameter k the GEV takes on three forms:

Type 1 or Gumbel distribution $k = 0$, (unbounded)
Type 2 or Fréchet distribution $k > 0$, (unbounded)
Type 3 or Weibull distribution $k < 0$, (bounded)

For $k \geq 0$, there is no upper bound to the distribution, and values of x can take on infinitely large values, although at very low probability levels. In

contrast, for $k < 0$ there is an upper bound to the magnitude of x. In addition, it should be noted that (2.4) is a distribution of maxima, whereas (2.3) is actually a distribution of minima (although used for maxima by considering the distribution of negative values $-x$). Although the AMM has the advantage of a sound theoretical basis and ensures that the data are IID, it has the very significant limitation of requiring very long time series (greater than 30 years) to form stable estimates of the PDF (i.e., only one value per year). In practice, such long time series are seldom available for the case of wind/wave data.

Goda (1988) proposes for oceanic storm applications the employment of the total sample method (i.e., IDM) or the peak value method (i.e., PoT), as the annual maximum method causes an increase in the confidence interval (Goda, 2010). However, the application of AMM using 23 years of satellite data are investigated by Vinoth (2011). The PoT method will be presented in the following.

2.1.3 Peaks over Threshold (PoT)

A compromise that addresses the data availability limitation of the AMM is the PoT approach (Castillo, 1988; Coles, 2001). Here, a threshold is set and only exceedences above this threshold considered. In such a case, it can be shown that data will follow a three-Parameter Weibull distribution (W3P; as applied by Vinoth, 2011), or a Generalized Pareto Distribution (GPD; Coles, 2001) as defined below,

$$F(x) = 1 - \left[1 + k\left(\frac{x - A}{B}\right)^{-1/k}\right], \tag{2.5}$$

where A becomes the value of the threshold. In this approach, there is no theoretical guidance on the selection of the threshold parameter A and it is usually a trade-off between stability and bias. That is, it must be low enough to ensure sufficient data are available to fit a stable PDF, whilst not so low that it biases the fit to the extreme values in the distribution. It is common to select a value at a chosen high percentile (e.g., 90th or 95th percentile; Anderson et al., 2001; Caires and Sterl, 2005; Challenor et al., 2005; Alves and Young, 2003; Vinoth and Young, 2011). It should be noted, however, that the selection of the threshold does affect the extreme-value estimates. In addition, the values chosen above the threshold must still be independent (i.e., from separate storms). This

is often achieved by ensuring data are separated by some defined time period (e.g., 48 h; Lopatoukhin et al., 2000; Caires and Sterl, 2005).

In the case of the PoT approach, the desired probability level for a 100-yr return period is

$$P(x < x^{100}) = 1 - N_Y / (100 N_{PoT}) , \tag{2.6}$$

where N_{PoT} is the number of data points in the PoT analysis, and N_Y is the number of years covered by the analysis.

2.2 Previous global extreme-value studies

The literature on extreme-value studies of wind speed and wave height is extensive. The vast majority of these studies, however, refer to point locations. We have not attempted to review this literature here, rather we concentrate on the more limited global studies. As a result, attention is confined to either numerical reanalysis model or satellite datasets.

EVA of wind speed and significant wave height can be based on model data obtained from hindcasts or reanalyses (Aarnes et al., 2012, 2015; Caires and Sterl, 2005). In this terminology, reanalysis is used to indicate that the model results include assimilation of measured data, whereas hindcasts do not include assimilation. A number of long-duration reanalyses combining numerical models of the atmosphere with data assimilation are now available in public archives. The European Centre for Medium-Range Weather Forecasts (ECMWF) has generated a series of increasingly sophisticated reanalyses. The first of these was the ECMWF 15-yr Re-Analysis (ERA-15; Gibson et al., 1997), covering the period 1979–93. ERA-40 (Uppala et al., 2005) covered the period 1957–2002. Several global oceanic extreme-value analyses have been based on the ERA-40 dataset [e.g., the Royal Meteorological Institute of the Netherlands (KNMI) Atlas; Caires and Sterl, 2005]. However, as demonstrated by Sterl and Caires (2005), ERA-40 model results generally underestimate wind speed and wave height extremes. The most commonly used reanalysis for EVA has been ERA-Interim (Dee et al., 2011), which covers the period from 1979 until 2018. For both, ERA-40 and ERA-Interim, a wave model

(WAM; WAMDI Group, 1988; Hasselmann et al., 1988) is incorporated into the model system. It should be pointed out that the issue of model resolution is being continually improved as computational capabilities improve. Note that ERA-Interim (hereinafter ERAI) was phased-out in August 2019 and replaced by the higher resolution ERA-5. The ERA-5 re-analysis reduces spatial resolution to 30 km (`https://www.ecmwf.int/en/forecasts/datasets/archive-datasets/reanalysis-datasets/era5`). ERAI has been used to evaluate ocean extremes by Aarnes et al. (2012, 2015). However, ERAI still underestimates wind speed and wave height extremes, and according to Stopa and Cheung (2014) particular attention must be paid to the analysis of the upper percentiles of the data, which may not be well represented by the model.

The length of the reanalysis model records allows the use of threshold methods (PoT) to determine global distributions of the 100-yr return period wind speed U_{10}^{100} and significant wave height H_s^{100}. Such datasets have three significant limitations: the spatial resolution means that intense small-scale events such as tropical cyclones are not well resolved, the ability of the models to reliably model extreme events has been questioned (Stopa and Cheung, 2014), and the quantity of data assimilated into the models varies with time, meaning that reanalysis data may not be temporally stationary (Breivik et al., 2014; Aarnes et al., 2015, 2012).

An innovative alternative to the use of reanalysis data is to create very long-duration equivalent time series using forecast ensembles (Breivik et al., 2013, 2014; Meucci et al., 2018). By considering ensemble forecasts at long forecast lead times (9–10 days), synthetic datasets of durations longer than 300 years can be formed. With such data, EVA can be performed without the need of any assumed PDF form (the probability level is "in sample" and can be determined directly from the ranked data). This effectively removes issues of extrapolation to the desired probability level, but questions about stationarity and tail biases (the ability of a coarse model to represent extreme events) remain.

As the satellite records lengthened (the most recent satellite altimeter time series is now 33-years long, covering the period 1985–2018; Ribal and Young, 2019), a number of studies investigated global values of extreme wind speed and wave height [previous EVA studies on wind speed and wave height are discussed extensively in Vinoth (2011)]. These include Alves and Young

(2003; 10 years of data), Chen et al. (2004; 8 years of data), Challenor et al. (2005; 11 years of data), Wimmer et al. (2006; 11 years of data), and Vinoth and Young (2011; 23 years of data). Vinoth and Young (2011) investigated the use of PoT analyses in which the extreme tail of the PDF is modelled. However, with 23 years of data, they found results were unusable for wind speed but showed some promise when applied to significant wave height. Hence, they adopted an IDM analysis, as did all the previous studies (Tucker, 1991; Cooper and Forristall, 1997; Teng, 1998). As the IDM approach uses the full PDF it is relatively stable when only short time series are available, but its modelling of the low probability tail of the distribution is poor and hence it can produce unreliable extreme-value estimates (Takbash et al., 2019).

Although these analyses produce plausible global distributions of U_{10}^{100} and H_s^{100} and comparable values to point buoy measurements, there are again doubts about whether the instruments accurately measure extreme conditions and, perhaps more importantly, whether they undersample extreme events due to the satellite orbit and footprint size (i.e., storm peaks or whole storms may be missed as altimeter ground tracks can be separated by hundreds of kilometers). It should be noted that all of the previous studies use radar altimeters with very narrow swaths on the Earth's surface. Instruments such as radiometers and scatterometers, which measure over a broad swath, have not previously been used for global extreme-value analysis. However, Takbash et al. (2019) examined a long-term dataset of both altimeter and radiometer systems for EVA of oceanic parameter (Chapters 3, 4, and 5).

2.3 The relevance of the confidence interval: The case of global extreme wave height

The uncertainty in the estimation of extreme values is commonly represented in terms of confidence limits, where $CL^{0.025}$ and $CL^{0.975}$ represent the 95% lower and upper confidence limits, respectively, of the values of the 100-yr return period significant wave height H_s^{100}. The difference between these values, $CI^{0.95} = CL^{0.975} - CL^{0.025}$ is the 95% confidence interval; statistically, there is a 95% probability that the true value of the 100-yr return period significant wave height lies within this interval around the estimate H_s^{100} (Muir and El-Shaarawi, 1986; Mathiesen et al., 1994). A primary concern in the estimation

of extreme values is reducing the CI and hence increasing the confidence in the extreme-value estimates (Mathiesen et al., 1994; Breivik et al., 2013, 2014; Breivik and Aarnes, 2017; Meucci et al., 2018). As a result, a number of recent studies have examined approaches to reduce the CI (Bulgakov et al., 2018; Meucci et al., 2018; Takbash et al., 2019). The magnitude of the CI can be reduced by either increasing the number of observations of extreme events, thus improving confidence that the tail of the PDF is well defined or by increasing the duration of the record, thus reducing the magnitude of the extrapolation to the desired probability level. The desire to increase the length of the data record is common to extreme-value applications for in situ, model, and satellite remote sensing data and has been discussed in numerous studies (Caires and Sterl, 2005; Mazas and Hamm, 2011; Young et al., 2017; Takbash et al., 2019). In the context of satellite remote sensing data, increasing the amount of data points is achieved by combining data values observed over a wider region. This is typically achieved by pooling data from a region around a given point (Young, 1994; Cooper and Forristall, 1997; Alves and Young, 2003; Vinoth and Young, 2011). In pooling data in this manner, there is an implicit assumption that the additional data is not statistically independent and hence all data is assumed to apply to a point at the centre of the region. Obviously, as the region over which data is pooled increases, there is a reduction in the spatial resolution (Chen et al., 2004; Vinoth and Young, 2011).

Present-day weather prediction systems include a stochastic element to account for the intrinsic uncertainty in initial conditions by running an ensemble of forecasts, each initiated with slightly perturbed initial conditions, rather than a single deterministic forecast (Lewis, 2005). Breivik et al. (2013, 2014) and Meucci et al. (2018) have taken advantage of the fact that at long lead time (9–10 days) these forecasts diverge to the point where they have low correlation. In such circumstances, each forecast in the ensemble potentially becomes an independent realisation of a potential sea state. They show that provided the ensemble members are independent and identically distributed, they can be pooled to create a dataset with an equivalent duration much longer than the duration of the forecast time series. Using this approach, Meucci et al. (2018) created a dataset from ensemble forecasts equivalent to 750 years from a 6-yr archive taken between 2010 and 2016. As the equivalent duration of the dataset is longer than the desired return period (100 years), the extreme-value estimates can be obtained without the need for extrapolation.

This approach produced H_s^{100} estimates consistent with buoy data and with plausible spatial distributions. Importantly, due to the length of the synthesized dataset the $CI^{0.95}$ was reduced by more than 70% compared to a traditional PoT extreme-value analysis (Meucci et al., 2018).

Chapter 3

Satellite data

Chapter 3 provides an overview of the satellite altimeter dataset (Section 3.1) and the radiometer dataset (Section 3.2) used in this work. The performance of such data under extreme conditions is examined in Section 3.3. This chapter is based on the publication Takbash et al. (2019).

The present study is based on the calibrated and validated satellite database of Young et al. (2017). This database consists of altimeter (H_s and U_{10}) and radiometer (U_{10}) data over the period 1984–2014 (approximately 30 years). The data come from a total of 23 different satellites over this period. Each of these satellite datasets was individually calibrated (i.e., linear regression correction – slope and offset) against NDBC buoy data, validated against an independent buoy dataset, and cross validated at crossover points with other satellite systems. In addition, the satellites were examined for any discontinuities or drifts in calibration over time, and where these were detected, the data were corrected.

A full description of the manner in which altimeters measure wind speed and wave height and radiometers measure wind speed can be found in Young et al. (2017) and Young and Donelan (2018). These details are not repeated here. However, there are a number of issues that are important when such data are subjected to EVA. These issues will be approached in the following sections.

3.1 Altimeter data

Ribal and Young (2019) recently introduced an updated version of the Young et al. (2017) altimeter dataset, which now covers 33 years (1985 to 2018), obtained from 13 altimeters, and with convenient access for users. The Young et al. (2017) altimeter data used in this work includes nine missions [in order of launch: Geosat, ERS-1, TOPEX, ERS-2, Geosat Follow-On (GFO), Jason-1, Envisat, Jason-2, CryoSat] and covers a period of 30 years, from 31 March 1985 until 1 April 2015 with a gap of one year and eight months between 1991 and 1992 (Figure 3.1). Drifts or discontinuities of satellite data (drifts of GFO for U_{10} and TOPEX for H_s) were corrected. For extreme-value estimation, the altimeter data were used without the duplicated CryoSat missions, since deficiencies were detected in the results due to CryoSat tracks. Zieger et al. (2009) describe the calibration and validation process of an older version of this altimeter dataset.

Values of H_s were taken directly from Globwave (`http://globwave.ifremer.fr/`) NetCDF-files and calibrated as described in Young et al. (2015, 2017). U_{10} was determined from the Globewave values of σ_0 using a combination of algorithms formulated by Abdalla (2007) in (3.1) for U_{10} smaller than 18 m s^{-1} and a modified Young (1993) relation for U_{10} greater than 18 m s^{-1} in (3.2).

$$U_{10} = U_m + 1.4U_m^{0.096}\ exp\left(-0.32U_m^{1.096}\right), \tag{3.1}$$

where

$$U_m = \begin{cases} 46.5 - 3.6\sigma_0 & \text{for } \sigma_0 \leq 10.917\ dB \\ 1690\ exp\left(-0.5\sigma_0\right) & \text{for } \sigma_0 > 10.917\ dB \end{cases}$$

$$U_{10} = -6.4\sigma_0 + 69 \tag{3.2}$$

Altimeters are “nadir looking” instruments and measure along a line directly below the satellite. The footprint is approximately 8–10 km in diameter with roughly one measurement per second. As a result, altimeters have very good along-track resolution (approximately every 10 km) but relatively low across-track measurement density. Depending on the orbit, ground tracks are 100–400 km apart at the equator. The exact repeat cycle or time until the satellite repeats the same ground track varies from 3 to 10 days. As a result, altimeters in polar

orbits observe the globe from about 80° S to 80° N but may undersample or completely miss small- to medium-size storms. Although there have been very few studies on the impact of rain on altimeter measurements, it appears that they are not greatly affected by rain (Young and Donelan, 2018).

3.2 Radiometer data

The REMSS radiometer data used (`http://www.remss.com/`) include 12 missions (SSM/I F8-F17, AMSR-E, AMSRJ, TMI, and WindSat) with a total time period of 26 years from July 1987 until June 2013 (Figure 3.1).

Values of U_{10} were taken directly from the REMSS data files and calibrated as described in Young et al. (2015, 2017). In contrast to altimeter systems, radiometers (which measure only wind speed), measure over a broad swath, approximately 1400 km wide. Across this swath, they provide data at approximately 25 km resolution. Therefore, a typical radiometer in a polar orbit will visit most points on Earth's surface twice per day. At a particular location, the radiometer will typically produce approximately 30 times more data than an altimeter. Hence, radiometers should be much less affected by undersampling than altimeters. However, radiometer measurements are heavily influenced by rain and typically cannot measure under heavy rain conditions. As a result, it is very common for radiometers to miss the peaks of storms where there is commonly heavy rain. As a result, this may introduce a "fair-weather" bias in radiometer data (Young et al., 2017; Young and Donelan, 2018).

3.3 Performance of the satellite data at extreme conditions

In addition to calibrating the instruments, Young et al. (2017) also examined their performance at extreme conditions. This was accomplished by examining quantile–quantile (QQ) plots between altimeter/radiometer and buoy data, as well as QQ-plots between altimeter and radiometer winds at crossover points. They concluded that compared to buoys, altimeters measure H_s accurately up to 10 m and U_{10} to 25 m s^{-1}. This was as high as reliable matchup data were available, and it is likely that this good performance extends beyond these values. It should be noted that the choice of algorithm relating radar cross

section to wind speed for altimeters is critical to their high-wind performance. Young et al. (2017) used a combination of the form proposed by Abdalla (2007) in (3.1) with the high wind speed correction of Young (1993) in (3.2). This same combination has been used here.

In contrast to altimeters, radiometers appeared to overestimate wind speed compared to buoys above 20 m s^{-1}. However, there is evidence (Large et al., 1995; Zeng and Brown, 1998; Taylor and Yelland, 2001; Howden et al., 2008; Bender et al., 2010; Jensen et al., 2015) that buoys may underestimate extreme wind speeds and waves due to tilting of the buoy and sheltering by large waves. It is therefore questionable to assume that buoys represent "ground truth" under extreme conditions.

As high-wind performance is critical for EVA, therefore alternative wind observations to conventional buoys were sought. The obvious alternative is offshore platform data. Data were obtained from the Norwegian Meteorological Institute for offshore oil platforms. The locations where data were available are shown in Figure 3.2. Offshore platform data are known to have a number

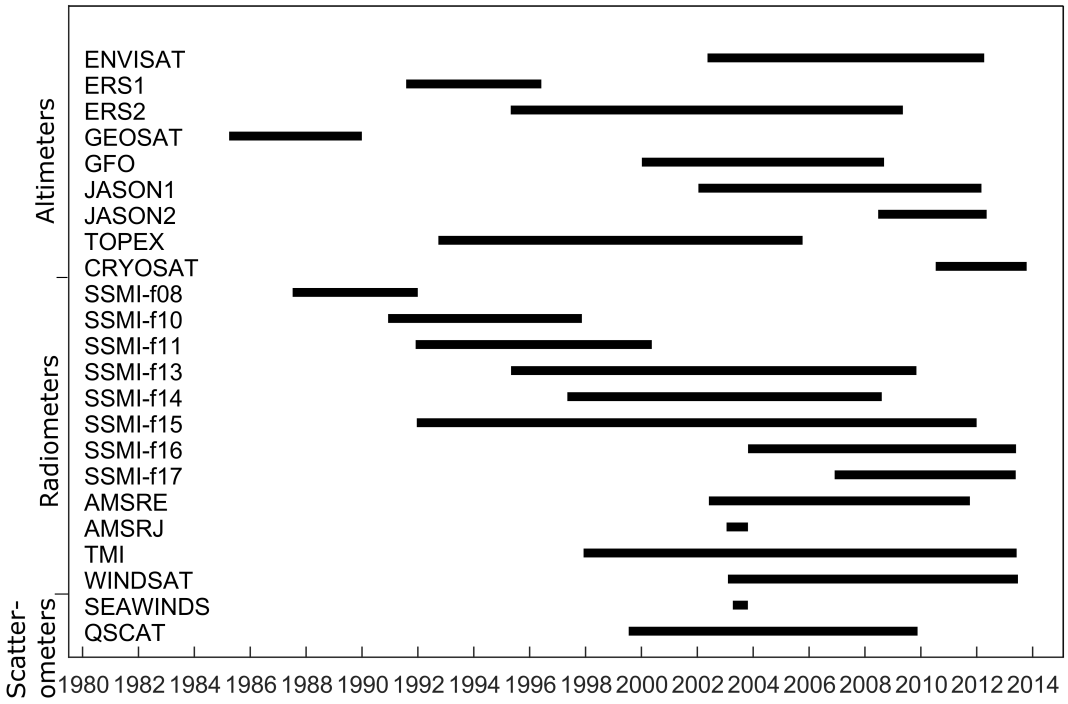

Figure 3.1: The duration of each of the altimeter and radiometer missions used.

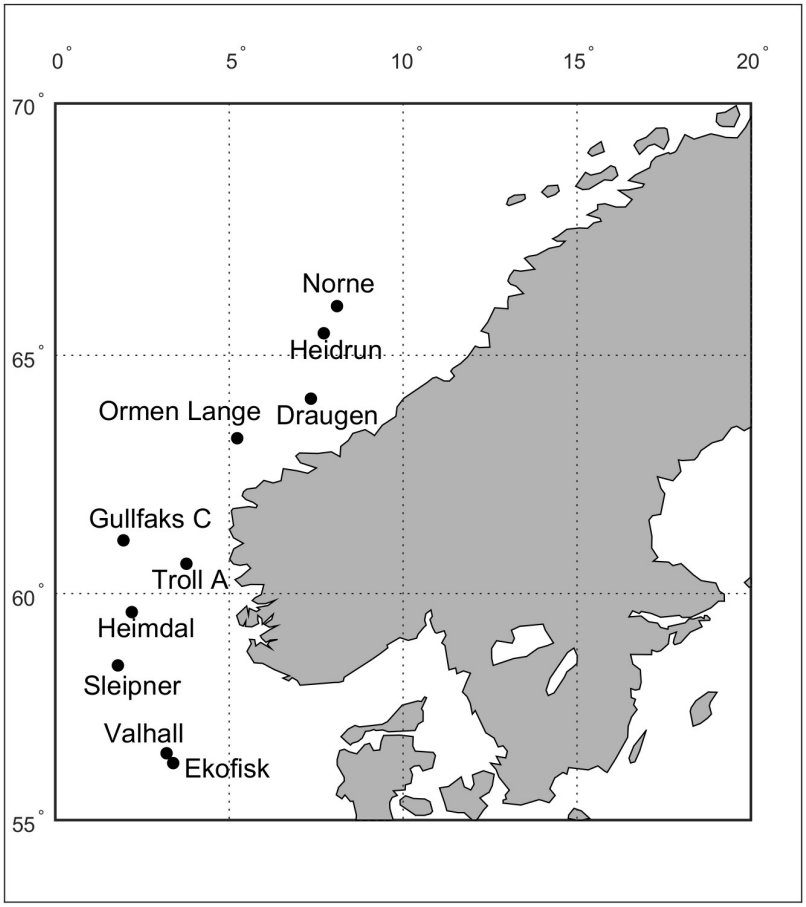

Figure 3.2: Locations of offshore platforms used to obtain anemometer data for high wind speed calibration of the radiometer instruments.

of issues, most notably flow distortion caused by the structure. However, this dataset has been extensively studied by the Norwegian oil industry, and power-law corrections were available for each of the anemometers to correct the data to a standard reference height of 10 m. The same matchup criteria adopted by Young et al. (2017) were used. That is, the satellite data needed to be within 50 km of the platform, and the mismatch in measurement time must be less than 30 min. One of the challenges in carrying out a high wind speed calibration is obtaining sufficient data under these conditions (i.e., there are few collocated observations at high winds).

To maximize the available data, only radiometer passes were considered (30 times more data than for the altimeter). In addition, as the results of Young et al. (2017) showed that there was little calibration difference between the various radiometers, these were all pooled to form a single composite dataset.

The dataset consisted of more than 280,000 matchups, but only 1% of the wind measurements exceeded 20 m s^{-1}. Figure 3.3 shows both scatterplots of platform and radiometer winds and the corresponding QQ-plots. Figure 3.3(a) shows the relationship between radiometer wind speed with the Young et al. (2017) calibration applied and the platform anemometer winds. Below 20 m s^{-1}, the data agree remarkably well, indicating that the boundary layer corrections applied to the platform data were valid and there was minimal impact from flow distortion around the platforms. Above approximately 20 m s^{-1}, however, a gradual rolloff in the data is apparent (radiometer winds are higher than platform winds). This is more clearly seen in the corresponding QQ-plot [Figure 3.3(b)]. To address this issue, the following empirical correction was applied to data above 18 m s^{-1}:

$$U_{10}^{*} = U_{10}\left[1 - 0.013\left(U_{10} - 18\right)^{0.79}\right], \tag{3.3}$$

where U_{10} is the radiometer wind speed, after the calibration relations of Young et al. (2017) are applied, and U_{10}^{*} is the corrected wind speed. In (3.3), units for wind speed are meters per second. Figures 3.3(c) and 3.3(d) show the results once the correction in (3.3) has been applied. It should be noted that (3.3) is based entirely on the data from the Norwegian sites shown in Figure 3.2. It has been assumed that this calibration holds generally and has subsequently been applied globally.

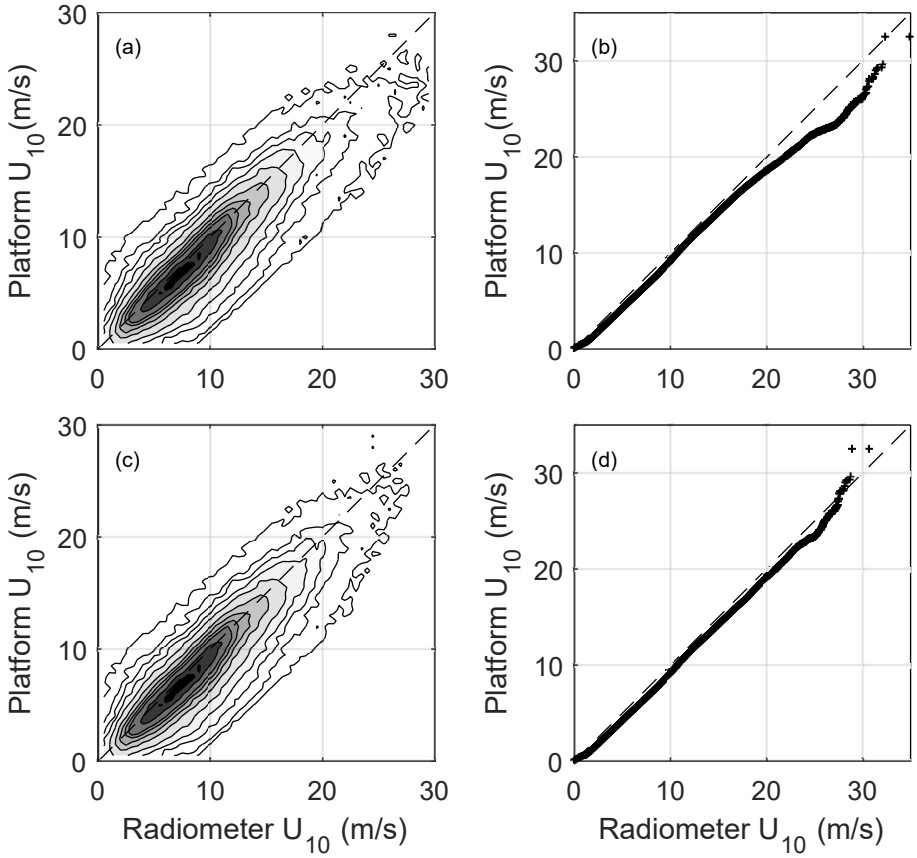

Figure 3.3: Radiometer–platform anemometer comparisons: (left) scatterplots and (right) QQ plots with (a),(b) no high wind speed correction and (c),(d) high wind speed correction [(3.3)].

Chapter 4

Validation of satellite EVA against buoys

To investigate the accuracy of satellite high wind speed and high wave height measurements and to validate the resulting 100-yr return levels, the performance of each platform (altimeter and radiometer) was investigated by comparing extreme-values driven from satellite data to extreme-values driven from buoy data. Chapter 4 describes the buoy data used (Section 4.1) and the validation process (Section 4.2). The content of this chapter is based on the publication Takbash et al. (2019).

4.1 NOAA buoy data

Wind speed and wave height data at a 1-h interval were taken from ten deep-water buoys of the National Data Buoy Center (NDBC; Evans et al., 2003), subordinated to U. S. National Oceanic and Atmospheric Administration's (NOAA). Figure 4.1 shows the locations of the used buoys.

The H_s and U_{10} values were taken directly from the NDBC NetCDF files. These are the same subset used by Vinoth and Young (2011; see their Fig. 2), but with a longer duration of approximately 38 years. These buoys were selected, as they are all more than 200km from shore, have a water depth exceeding 300 m, and were operational for the full duration of the combined satellite datasets (1984–2014).

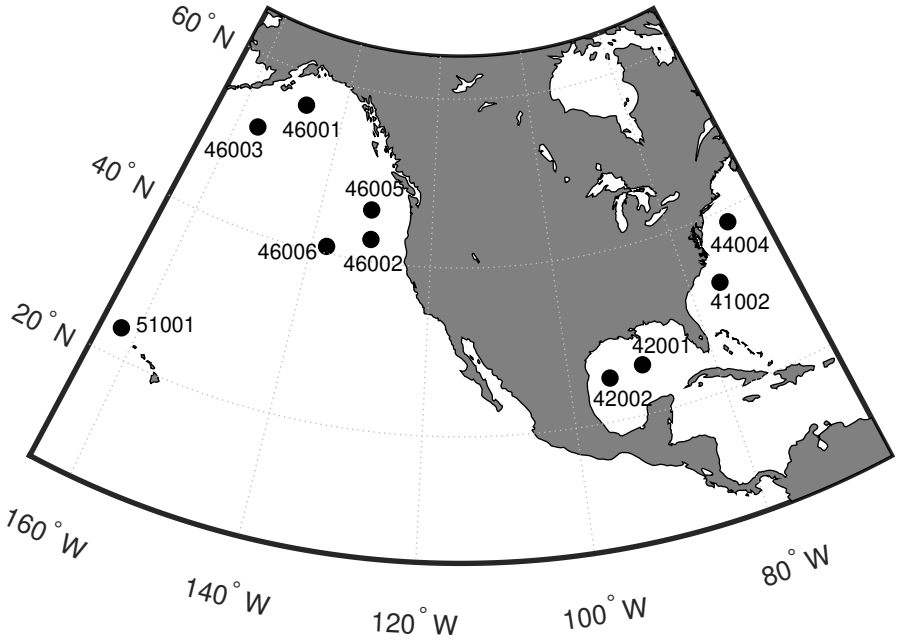

Figure 4.1: Locations of NDBC buoys covering the geographical regions North Pacific (46001, 46002, 46003, 46005, and 46006), North Atlantic (41002 and 44004), Gulf of Mexico (42001 and 42002), and the Pacific trade wind belt (Hawaii, 51001) which were used for validation of the satellite extreme-value estimates.

4.2 Application of satellite database to global estimates of extreme wave height and wind speed

The irregularly sampled satellite data used in this work is available on a 1° spatial grid on the globe's surface. Previous EVA studies, (e.g., Vinoth and Young, 2011), divided the world into spatial (grid) regions and pooled all satellite data in each grid region. These grid regions are then considered as independent observation regions, and EVA is applied independently for each region. For this study, the aim is to consider maximum sample values for each event, rather than all observations. Alves and Young (2003) and Vinoth and Young (2011) showed that a coarser spatial resolution improves the results of global extreme-value estimation, especially when considering the PoT approach as a larger sampling region means more data can be considered. Therefore, for EVA in this study, the data from four 1° bins on the globe's surface were added (pooled) together into a 2° x 2° data grid, and only

maximum values for each pass, i.e. event (sequential in time) were selected (the quality control processes successfully eliminated any data spikes). In Chapter 5, this binned dataset is used to investigate global distributions of extreme values.

The process of declustering the data for satellite measurements was applied similarly to the NDBC buoy data. As such, the time was sorted in sequential order, and maximum values were selected for each time sequence (which correspond to each satellite track). That is, for each satellite track across a 2° x 2° grid square, the maximum value was selected.

To validate the regionally sampled satellite data against point measurements from buoys, firstly, those 2° bins were determined, which most closely matched each buoy location (buoy location centred on the 2° bin). The validation approach used by (Vinoth and Young, 2011) consisted of determining extreme-value estimates (U_{10}^{100}, H_s^{100}) using both IDM and PoT approaches for both buoy and satellite (altimeter in their case). They then compared IDM estimates from buoy with altimeter and PoT estimates for buoy with altimeter (i.e., they compared IDM buoy with IDM altimeter and PoT buoy with PoT altimeter). What this showed was that the IDM results agreed well, but the PoT approach exhibited significant differences. This is not surprising as the IDM fit is dominated by the body of the distribution rather than the tail. As long as buoys and altimeters produced similar mean conditions, the IDM approach will give extremes of comparable magnitude.

As the time series in this study is longer than in the previous studies, a more challenging validation approach was adapted. With 30 years of data, PoT estimates from buoys can be obtained with reasonable confidence. Therefore, the PoT estimates from the buoys are taken as the baseline (ground truth) and satellite estimates from PoT and IDM are compared with these values. An important issue in applying the PoT analysis is to select an appropriate threshold parameter [A in (2.5)]. To investigate the sensitivity of extreme-value estimates from the GPD [(2.5)] to the threshold value, a 2° x 2° region centred on 40° N, 180° E (North Pacific) was selected as a representative test point. The values of U_{10}^{100} and H_s^{100} were calculated using the PoT approach and the altimeter data for a number of different values of threshold, each specified as a percentile value. The results, normalized by the value with a threshold at the 75th percentile, are shown in Figure 4.2. For both wind speed and wave height,

the extreme-value estimates increase as the threshold value is increased before reaching a peak and then decreasing. Depending on the threshold choice, the resulting extreme values can vary by up to 30%. The values of H_s^{100} are more sensitive to the choice of a threshold than U_{10}^{100}. Ultimately, the 90th percentile was adopted for the subsequent calculations. This choice was primarily dictated by a desire to avoid the region of Figure 4.2, where the values seem most sensitive to the choice while keeping the threshold value as high as possible. Other locations were also tested and, although there are differences, Figure 4.2 is broadly representative.

When applying a PoT analysis to the satellite data, care must still be exercised to ensure that the data taken above the selected threshold are independent. In the case of altimeter passes, this is seldom an issue as, even with multiple satellites in orbit, satellite passes at a location are typically separated by at least two days (48 h). Radiometer data are potentially more problematic, as a single radiometer will image each location twice a day (12-h separation). To test the sensitivity to these issues, data were filtered such that only values separated by chosen times were considered (e.g., data separated by 48 h). The calculated extreme values were quite insensitive to the chosen time separation, and, hence, data separated by a minimum of 48 h have been used here.

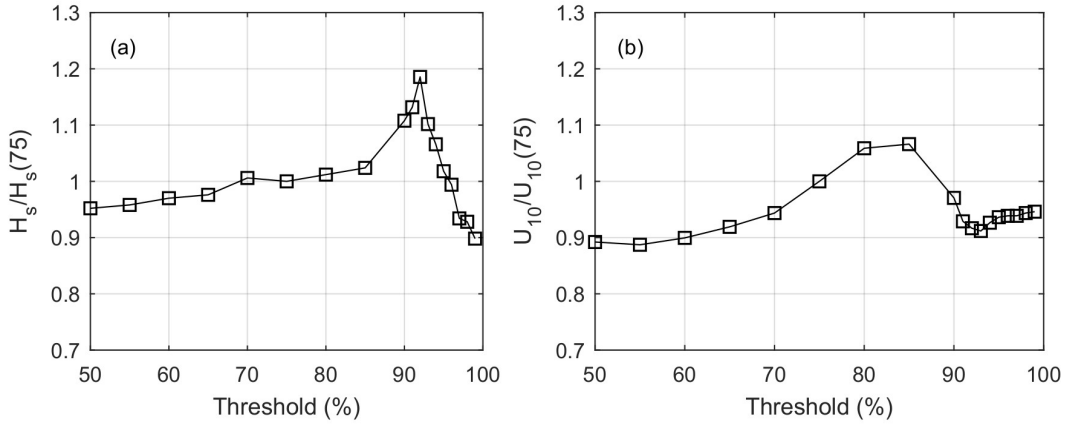

Figure 4.2: Values of (a) H_s^{100} and (b) U_{10}^{100} as a function of the threshold used for the PoT analysis, expressed as a percentile. Values are shown normalized by the value at the 75th percentile. Data were taken from a representative 2° x 2° region centred on 40° N, 180° E (North Pacific).

Table 4.1 shows the values of H_s^{100} and U_{10}^{100} for buoys calculated using the PoT approach (values shown in italics columns of the table). These are compared to

altimeter values calculated with both PoT and IDM (H_s, U_{10}) and radiometer values calculated with IDM (U_{10}). As will be outlined in detail in Chapter 5, the radiometer data proved unsuitable for the application of the PoT approach and hence are not considered here. The values of H_s^{100} and U_{10}^{100} calculated for buoys using the PoT are in agreement with those of Vinoth and Young (2011). The differences can be attributed to the longer duration of measurements used here and a different threshold for the PoT analysis. To determine the differences between buoys and satellites, the mean error was calculated as

$$\Delta r = \left(H_{s,Alt}^{100} - H_{s,Buoy}^{100}\right) / H_{s,Buoy}^{100}, \tag{4.1}$$

for each buoy and then summed over all n buoys as $r = 1/n \sum \Delta r$. The mean error was calculated for U_{10}^{100} in a similar fashion. The altimeter PoT values are in reasonable agreement with the buoys with $r = -7.5\%$ for H_s^{100} and $r = +14.6\%$ for U_{10}^{100}. These values compare to Vinoth and Young (2011), who obtained $r = -17.31\%$ for H_s^{100} and $r = +40.61\%$ for U_{10}^{100}. Vinoth and Young (2011) ultimately concluded that the PoT approach could not be applied to determine extreme values using their dataset. The results in Table 4.1 seem to indicate that, at least at these buoy locations, the altimeter yields extreme-value estimates in reasonable agreement with buoys using the PoT approach.

Table 4.1: EVA of NDBC buoy and satellite data. Buoy data shown with italics.

Buoy No.	Lat (° N), lon (° E)	H_s buoy (PoT) (m)	H_s altimeter (PoT) (m)	H_s altimeter (IDM) (m)	U_{10} buoy (PoT) ($m\ s^{-1}$)	U_{10} altimeter (PoT) ($m\ s^{-1}$)	U_{10} altimeter (IDM) ($m\ s^{-1}$)	U_{10} radiometer (IDM) ($m\ s^{-1}$)
46001	56.23, 212.05	*13.8*	12.7	14.5	*24.9*	28.9	33.9	34.2
46002	42.61, 229.46	*14.7*	13.1	12.7	*24.4*	26.3	30.4	29.9
46003	51.33, 204.15	*16.1*	14.8	15.7	*26.1*	29.2	34.8	29.2
46005	46.14, 228.93	*14.6*	14.4	14.6	*25.3*	27.9	31.1	30.9
46006	40.78, 222.60	*15.4*	13.4	14.8	*27.2*	27.5	27.5	31.2
51005	24.42, 197.90	*11.9*	10.4	9.9	*18.9*	26.7	25.8	26.9
44004	38.48, 289.57	*13.5*	13.8	13.6	*27.3*	34.4	37.0	34.4
41002	31.76, 285.16	*13.5*	11.6	10.4	*25.9*	33.2	33.2	30.4
42001	25.90, 270.33	*11.5*	11.3	11.3	*28.1*	26.4	26.4	26.2
42002	26.09, 266.24	*11.5*	10.8	7.1	*26.3*	31.0	26.0	27.2
Error	—	—	-7.5%	-8.7%	—	+14.6%	+20.3%	+18.1%

As noted earlier, IDM estimates for buoys are not presented. An examination of the results of Vinoth and Young (2011) shows that H_s^{100} for the buoys are in reasonable agreement between PoT and IDM analyses using $D = 3\ h$. However, U_{10}^{100} buoy calculations with IDM were between 30% and 50% larger than the corresponding PoT calculations. This is perhaps not surprising, as the value of 3 h was developed for use with buoy data of H_s. When applied to U_{10} and other data, this value of D is questionable. This raises very significant doubts about

the use of the IDM approach. To obtain values of H_s^{100} and U_{10}^{100} with satellite data that were comparable to satellite or buoy PoT calculations, the values of D needed to be significantly increased. To obtain values of comparable magnitude for the use in comparative plots in Chapter 5, these values were arbitrarily increased to $D = 500\ h$ for wind speed (both altimeter and radiometer) and $D = 30\ h$ for significant wave height (altimeter). For completeness, calculations in Table 4.1 for IDM have also used these values. As will be shown in Chapter 5, the use of the IDM will not be advocated, and the arbitrary nature of the selection of D is just one of its limitations.

Chapter 5

Global distribution of extreme wind speed and wave height

In order to obtain the global distribution of extreme wave height (from altimeter) and wind speed (from altimeter and radiometer), sensitivity tests were performed, which are principally relevant to the case of the PoT approach. These tests considered the data quality, the number of data points available for each 2° region, and the threshold parameter (see Section 4.2 and Appendices A.1 and A.2). Regarding the quality control flag, it was found that a relaxation of the data quality by one level effects primarily the number of data points (larger number of data points available) rather than the quality of the data itself. Nevertheless, only data with a "good" quality control flag were considered for both PoT and IDM analyses. Overall, the EVA was found not to be excessively sensitive to these changes. EVA was performed when the number of data points for each region was greater than 1,000 to ensure stable GPD fits the data. In addition, the threshold parameter was set at the 90th percentile for H_s data and to a lower value of the 70th percentile for U_{10}. The lower percentile value for U_{10} led to a more stable fit for the "noisier" wind speed data.

The results from the PoT analysis are presented and discussed in Section 5.1 for altimeter data and in Section 5.2 for radiometer data. Section 5.3 focuses on the results from the IDM analysis of both altimeter and radiometer data as these results show similar features. In addition, a GEV analysis was performed for altimeter data (see Appendix A.3), however, these results are not further discussed here. PDF's from PoT and IDM fits are discussed and compared in Section 5.4. In Section 5.5, a discussion concerning the EVA in a time of

changing (extreme) wind and wave climates is provided. The content of the present chapter is based on the publication Takbash et al. (2019).

5.1 Altimeter PoT analysis

To investigate the global distribution of U_{10}^{100} and H_s^{100}, the data were binned using 2° x 2° bins, and the PoT analysis was applied to both wind speed and wave height for the altimeter data and wind speed for the radiometer data. Vinoth and Young (2011) attempted a similar analysis with the result showing extremely noisy distributions. They concluded that the distributions of H_s^{100} showed promise but that the U_{10}^{100} estimates were unusable.

Figure 5.1 shows colour-filled contour plots of U_{10}^{100} (Figure 5.1a) and H_s^{100} (Figure 5.1b) for the altimeter (PoT). The contours have been drawn on the 2° x 2° grid without further smoothing. In comparison to the findings of Vinoth and Young (2011), the results show a far smoother spatial distribution. The contours of U_{10}^{100} show much greater zonal structure than H_s^{100}. This is consistent with mean monthly climatology (Young, 1994, 1999; Young and Donelan, 2018) and is caused by the dispersive nature of waves. Once generated, waves propagate across oceanic basins as swell (Young et al., 2013), ensuring a smoother distribution of H_s than U_{10}. This is also the case for extreme values, as shown in Figure 5.1.

Figure 5.1a shows the maxima of U_{10}^{100} of approximately 38 m s^{-1} occur in the North Atlantic and North Pacific. Although the Southern Ocean is consistently windy year-round and monthly means in winter are comparable to the Northern Hemisphere (Young, 1999; Young and Donelan, 2018), the extremes are not as great. The maximum values of U_{10}^{100} in the Southern Ocean are approximately 34 m s^{-1}. This maximum tends to occur south of the Indian Ocean (between Australia and South Africa). The maxima in the North Atlantic and North Pacific tend to be displaced toward the western boundaries of these basins. The reason for this can be seen by examining Figure 5.2, which shows the storm tracks of tropical cyclones (and tropical low-pressure systems) over the period 1984–2014, obtained from the IBTrACS data archive (Knapp et al., 2010). For clarity, only every second storm track is shown in Figure 5.2.

Figure 5.2 shows that North Atlantic and Pacific tropical storms track

east to west across the tropics of each ocean basin, respectively, before turning north along the western boundary of each basin. Because of the small spatial scale of tropical cyclones and the relatively large distance between altimeter tracks, it is likely that these systems are under-sampled in the present analysis. As such systems move north, they tend to increase in size, making it more likely that they are observed by the altimeter. This is clear in the region of the western North Atlantic, where extreme winds are predicted (Figure 5.1a) north of 30° N, but there is no clear indication of tropical cyclones moving across the tropical regions of the Atlantic (east to west). In contrast, extreme winds

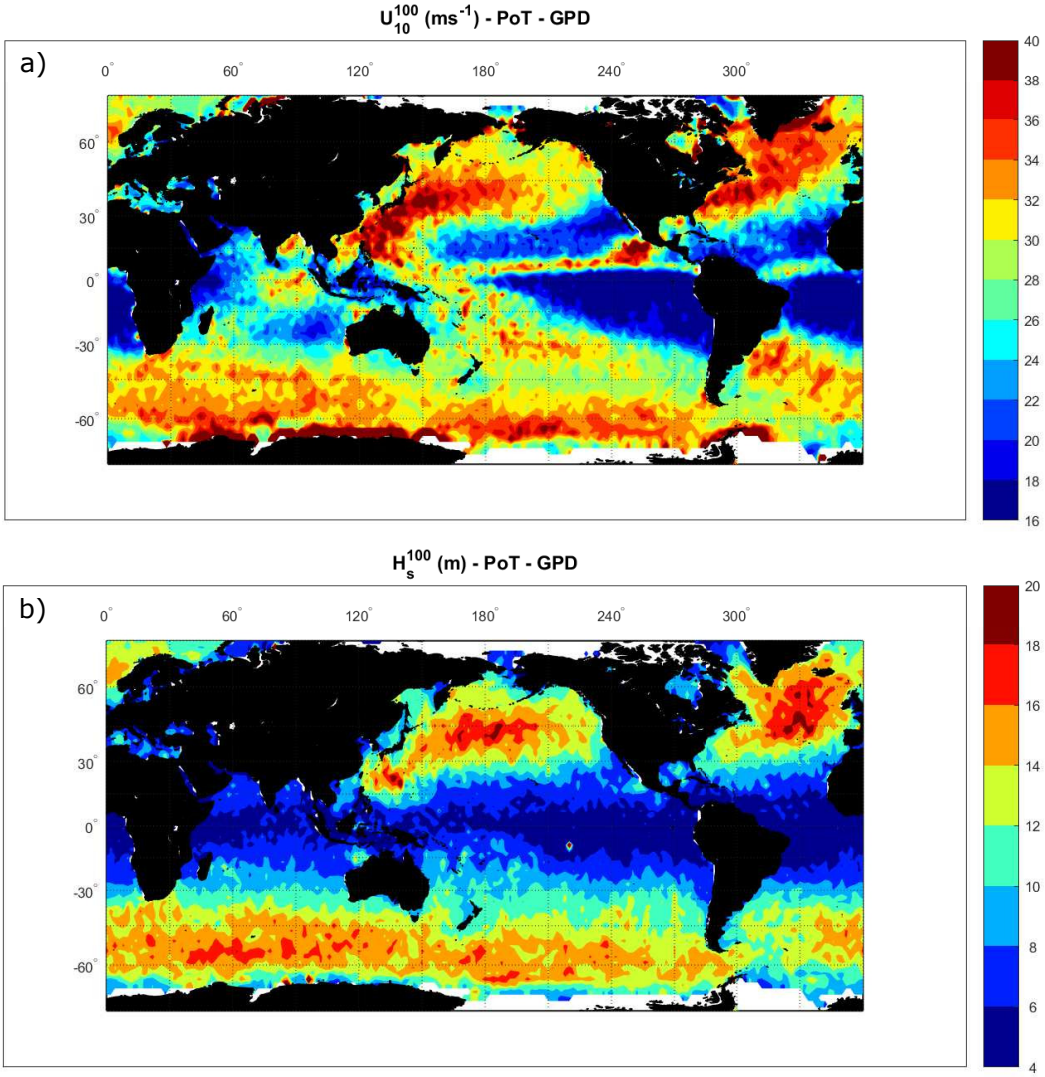

Figure 5.1: Global values of (top) U_{10}^{100} (m s^{-1}) and (bottom) H_s^{100} (m) obtained with a PoT analysis and a GPD distribution. Data obtained from altimeter missions.

along the western boundary of the Pacific are predicted as far south as 10° N. There is then a clear path of intense winds shown across the Pacific equatorial regions. North Pacific tropical cyclones (typhoons) tend to be larger in spatial extent than North Atlantic tropical cyclones (hurricanes; Knapp et al., 2010). They are also more frequent, as shown in Figure 5.2, making them less affected by under-sampling in the altimeter dataset. This explains why the east–west tropical track is clear in the western Pacific (10° N) but not the western Atlantic.

A number of other storm track features can also be seen in the values of U_{10}^{100} in Figure 5.1a. The region of high occurrence of tropical cyclones near the central American Pacific coast is reflected in a "hot spot" of extreme wind of approximately 38 m s^{-1} in that region. There is a region of reduced U_{10}^{100} in the central Indian Ocean. Figure 5.2 shows that this corresponds to a region almost devoid of tropical cyclones between the western Australian and eastern African basins. Less clearly, there is also a band of slightly elevated U_{10}^{100} from northeast of New Zealand to east of New Guinea. Again, this corresponds to the track regions for South Pacific storms. A further hot spot of elevated U_{10}^{100} can be seen in the Bay of Bengal, another region of high occurrence of tropical cyclones.

The eastern side of the South Atlantic (off Africa) shows relatively low

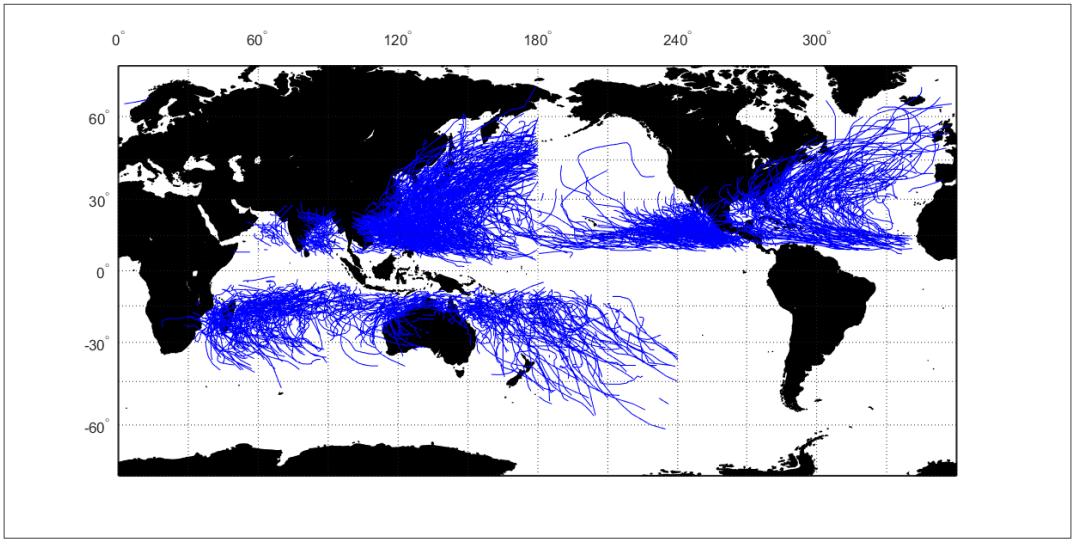

Figure 5.2: Storm tracks of tropical cyclones (and tropical low pressure systems) over the period 1984–2014, obtained from the IBTrACS data archive (Knapp et al., 2010). For clarity, only every second track is plotted.

values of U_{10}^{100} with the exception of a band of slightly increased values along the equator between South America and North Africa. It is probable that this is the signature of storm activity in the Inter-Tropical Convergence Zone (ITCZ). A triangular region of low U_{10}^{100} bounded by the equator west of South America is also clear in Figure 5.1a.

Many of the same features described above are also apparent in model calculations of U_{10}^{100} (Breivik et al., 2014; Meucci et al., 2018). Both the location and magnitudes of the maximum values in the North Atlantic and Pacific Oceans are comparable to Figure 5.1a. Also, the relatively low values in the triangular region west of South America and across the Atlantic west of Africa are found in both the model and altimeter data in Figure 5.1a. However, features that are attributed here to small-scale tropical cyclone activity are not clear in the model results. This includes tropical cyclone activity across the Pacific north of the equator, or in the Pacific Ocean east of Australia or the low-extremes area in the central Indian Ocean. It should be pointed out that neither the model results nor the altimeter dataset are optimal for investigating tropical cyclone extremes. The spatial resolution of the models (e.g., of order 100 km) means that tropical cyclone winds will not be resolved. In contrast, the altimeter will measure tropical cyclone winds (Young, 1993), provided there is a ground track close to the tropical cyclone. However, as noted above, these storms will be under-sampled. Therefore, the differences between U_{10}^{100} from model data and altimeter are as one would expect.

Figure 5.1b shows colour-filled contours of H_s^{100} calculated using the PoT method and altimeter data. As noted previously, there is much less small-scale variability than for U_{10}^{100} (Figure 5.1a). The largest values of H_s^{100} are once again in the North Atlantic and North Pacific, with values of approximately 18 m. Again, the regions with the largest extreme waves are displaced toward the western boundaries of these basins, but not to the same extent as the wind U_{10}^{100} (Figure 5.1a). Similar to the extreme winds, the largest values of H_s^{100} in the Southern Hemisphere are found south of the Indian Ocean between Australia and South Africa, with values of approximately 16 m. Values of H_s^{100} gradually decrease from these maximum regions in each hemisphere toward the equator. In the equatorial regions, H_s^{100} reaches only approximately 4 m. These results are much smoother (spatially) than the PoT results of (Vinoth and Young, 2011) and agree well with model results (Breivik et al., 2014; Meucci et al.,

2018) both in magnitude and spatial distribution.

Figure 5.1 represents the first ever plausible published estimates of U_{10}^{100} and H_s^{100} obtained from altimeter using a PoT analysis. These results suffer from the under-sampling of small-scale meteorological systems (e.g., tropical cyclones, storms) but are probably less affected than low-resolution model data.

5.2 Radiometer PoT analysis

Because of the much higher data rates (30 times more data) the radiometer has the potential to address the under-sampling issues noted above for altimeter U_{10}^{100} estimates with the PoT analysis. However, the radiometer also has features that are undesirable at high wind speeds. First, as noted in Chapter 4, collocation between anemometer and radiometer measurements shows that the radiometers overestimate wind speed above approximately 20 m s^{-1}. This issue was attempted to be addressed by the high wind speed correction in (3.3). In addition, however, the radiometer cannot measure while there is heavy rain. Examination of numerous cases of radiometer passes over tropical cyclones in the present dataset indicated that in almost all cases, a data "hole" exists around the centre of the storm with no usable data and, importantly, the high wind speeds being missed by the radiometer. The same characteristic is clear in many high-latitude storms with a data gap near the center of the storm.

Figure 5.3 shows colour-filled contours of U_{10}^{100} obtained from the radiometer and the PoT analysis. Figure 5.3a shows the result without the high wind speed correction [(3.3)] and Figure 5.3b with the inclusion of the correction. In comparing the radiometer U_{10}^{100} result with the altimeter values, it should be noted that the colour scale in Figure 5.3a (radiometer) is 26–58 m s^{-1} compared to Figure 5.1a (altimeter) of 16–40 m s^{-1}. That is, the radiometer without the high wind speed correction gives values of U_{10}^{100} much higher than the altimeter, previous model results (Breivik et al., 2014; Meucci et al., 2018), and the buoy data of Table 4.1. With the high wind speed correction (Figure 5.3b), the results are now of comparable magnitude to the altimeter (Figures 5.1a and 5.3b have the same colour scale). Also, Figure 5.3b shows many of the same spatial features as Figure 5.1a – highest values in the North Atlantic and Pacific, low-wind triangular region in the Pacific west of South America, tropical cyclone belt across the Pacific (but less distinct), ITCZ band across the equatorial

Atlantic (but less distinct), and the low wind speed region in the Indian Ocean. There are, however, a number of features in Figure 5.3b that differ from the altimeter results. The largest values of U_{10}^{100} do not occur in the storm belts at about 45° N, rather they occur in distinct separate belts at around 30° N. Similarly, a belt of high values of U_{10}^{100} exists across the Southern Hemisphere at approximately 30° S, rather than farther south in the Southern Ocean as in the altimeter data. Examination of the PDFs of the radiometer showed that at the higher latitudes, ±45°, the tail was abruptly truncated (i.e., no high values).

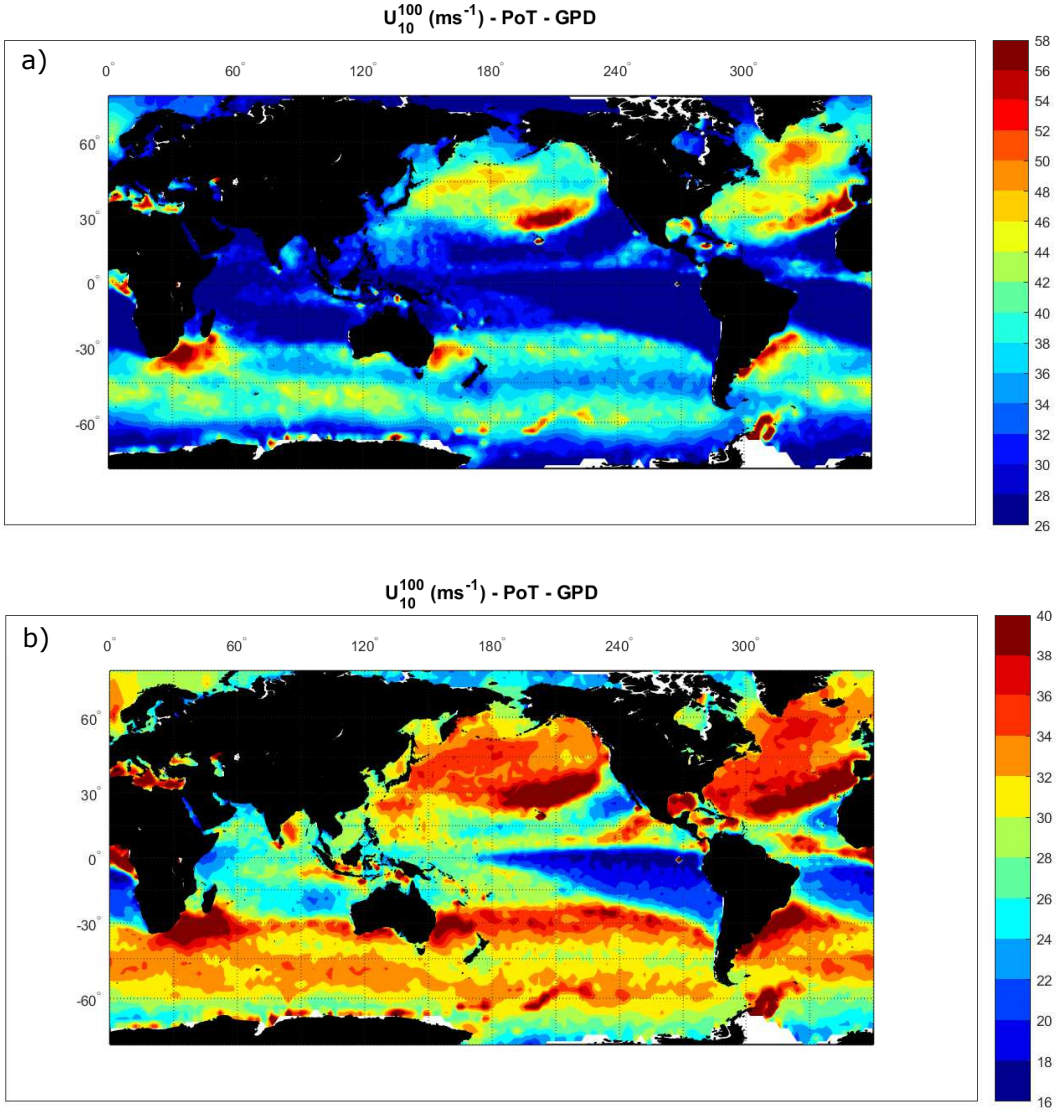

Figure 5.3: Global values of U_{10}^{100} (m s^{-1}) obtained with a PoT analysis and a GPD distribution. Data obtained from radiometer missions. (top) No high wind speed correction applied to the data. (bottom) The high wind speed correction [(3.3)] applied to the data.

This resulted in a GPD [(2.5)] fit to the data with a negative shape parameter k. This places an upper bound on U_{10}^{100}. In contrast, at lower latitudes k remained positive, producing no upper bound and the larger values of U_{10}^{100} produced at $\pm 30°$. It is speculated here that the lack of high wind speed data at $\pm 45°$ is caused by the extreme winds not being sensed by the radiometer because of high rain rates. As the spatial distributions in Figure 5.3b (or Figure 5.3a) are not plausible, an alternative fit to the radiometer PDFs was sought.

In an attempt to address the issues raised above, an exponential (EXP) distribution was used with the PoT analysis rather than a GPD. The EXP distribution is a special case of the GPD [(2.5)] with $k = 0$. This produces an unbounded distribution but without the variability caused by having k determined by the fit to the data (which is problematic in the tail of the radiometer PDF). The resulting values of U_{10}^{100} are shown in Figure 5.4. As in Figure 5.3b, the high wind speed correction [(3.3)] has been used but with the EXP distribution.

Although the use of the EXP has produced results that vary spatially in a smooth manner, the spatial distributions are quite different from the altimeter GPD (and previously published results; Vinoth and Young, 2011; Breivik et al.,

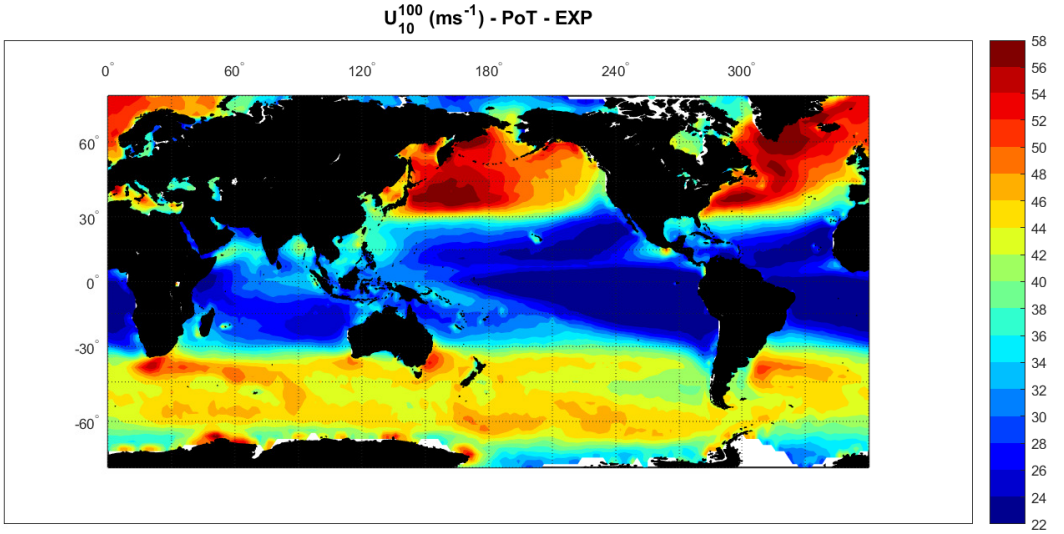

Figure 5.4: Global values of U_{10}^{100} (m s^{-1}) obtained with a PoT analysis and an EXP distribution. Data obtained from radiometer missions. The high wind speed correction [(3.3)] applied to the data.

2014). Although the high wind speed correction [(3.3)] was used for the data in Figure 5.4, the magnitude of the values of U_{10}^{100} are much greater than Figure 5.1a (altimeter, GPD)—scale 22–58 m s^{-1}. As a result, it is concluded that the EXP distribution produces unsatisfactory results.

The results of Figure 5.3 and 5.4 indicate that, despite the greater sampling density provided by the radiometer, its inability to provide data during rain events introduces an unacceptable fair-weather bias for extreme-value applications.

5.3 IDM analyses of altimeter and radiometer

As noted earlier, all previous studies of extreme-value estimates from satellite data (altimeter) have opted for an IDM analysis. This is despite the many shortcomings of the approach outlined in Section 2.1.1 (value of decorrelation scale D, independent and identically distributed data). As the present analysis provides, for the first time, stable estimates of both U_{10}^{100} and H_s^{100} from a PoT analysis, these can be used as a basis to assess the usefulness of an IDM analysis.

Figures 5.5a and 5.5b show U_{10}^{100} and H_s^{100}, respectively, for an IDM analysis of altimeter data. As noted in Table 4.1, the decorrelation scales D were chosen so as to give results of comparable magnitudes to the altimeter and buoy PoT results ($U_{10}^{100}, D = 500\ h; H_s^{100}, D = 30\ h$).

As expected, the results (Figures 5.5a and 5.5b) show smooth spatial distributions. Also, the values of U_{10}^{100} produced by both altimeter and radiometer (see Figure 5.6) are very similar. This is in stark contrast to the results for the PoT analysis. Although this may seem a positive feature of the IDM, this occurs because the IDM fit to the PDF is controlled by the body of the PDF rather than the tail. The altimeters and radiometers produce mean monthly wind speeds in similar patterns (Young and Donelan, 2018). Therefore, they will produce IDM fits to the data that are also similar. The fact that the tails of the respective distributions are quite different has little impact on the resulting values of U_{10}^{100}. The spatial distributions of U_{10}^{100} are also very similar to the mean monthly distributions. For instance, the maximum values in each hemisphere are of similar magnitude (not the case for the PoT), and the distributions in the North Atlantic and Pacific are more centrally located, rather than being in the

storm belts. Although there is some suggestion of a tropical cyclone belt across the Pacific, this is much less distinct than for the PoT analysis and all other tropical cyclone signatures are absent in the IDM analysis. Another interesting difference is that the PoT analysis did not show a local maximum in the area of the Horn of Africa, as a result of the Somali/Oman coastal low-level jet (CLLJ; Ranjha et al., 2015). In contrast, the IDM shows a distinct local maximum (cf. Figure 5.5a and 5.6).

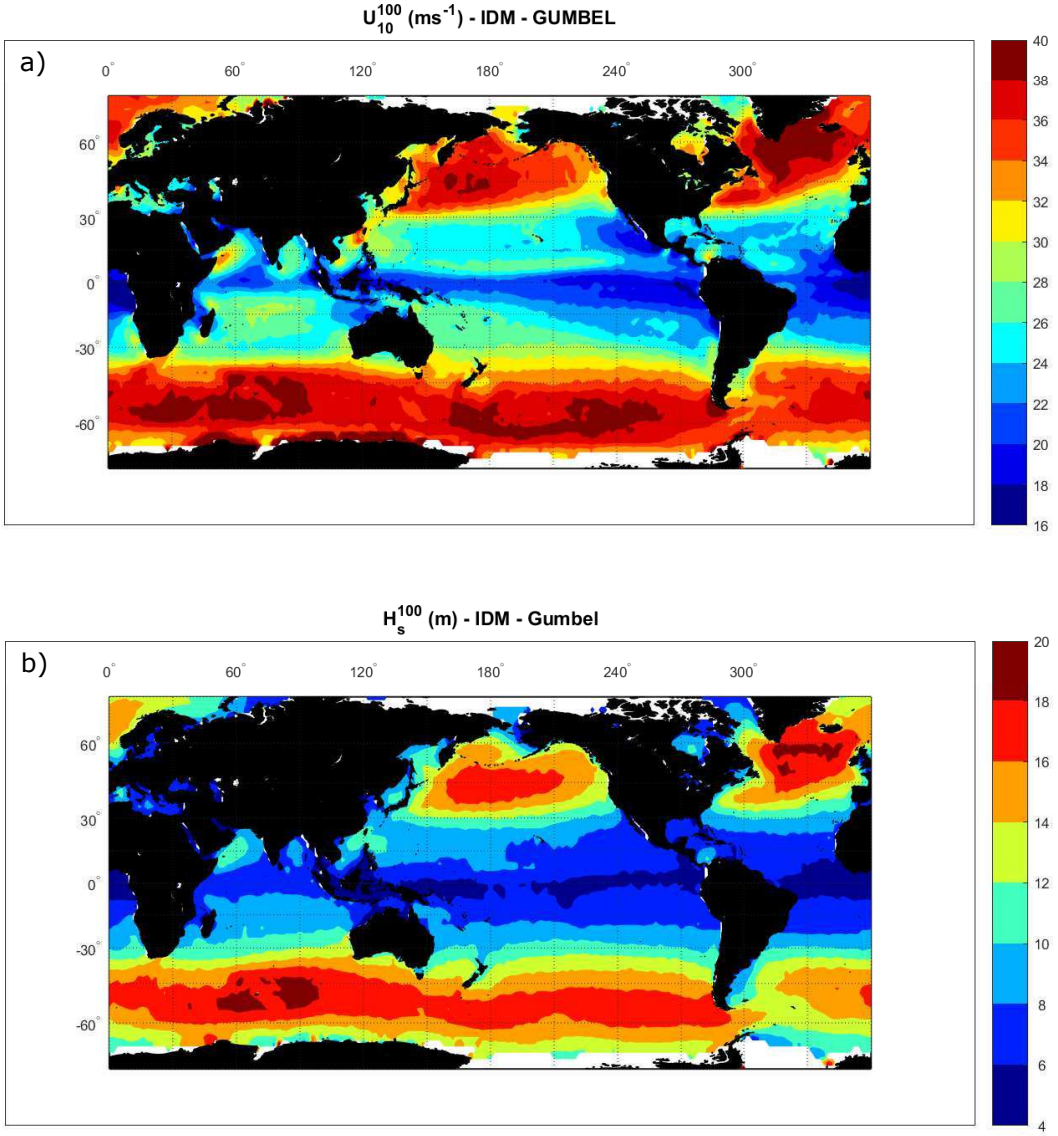

Figure 5.5: Global values of (top) U_{10}^{100} (m s^{-1}) and (bottom) H_s^{100} (m) obtained with an IDM analysis and a Gumbel distribution. Data obtained from altimeter missions.

The values of H_s^{100} largely follow the same spatial distributions as U_{10}^{100} (cf. Figure 5.5a and 5.5b). This again occurs because the spatial distributions of mean wind speeds and wave heights are similar.

Extreme-value estimates from radiometer data using an IDM analysis are shown in Figure 5.6 for U_{10}^{100}. This result is very similar to the results shown above for altimeter data in combination with an IDM analysis. Therefore, the arguments raised above (in this section) apply here as well.

To highlight the differences between the two EVA methods more in detail, Section 5.4 provides a comparison between PDFs from PoT and IDM analyses for both wind speed and wave height at two specific locations. The unsuitability of the radiometer data (U_{10}) for PoT EVA was shown in the previous section. Therefore, Section 5.4 will concentrate on altimeter data.

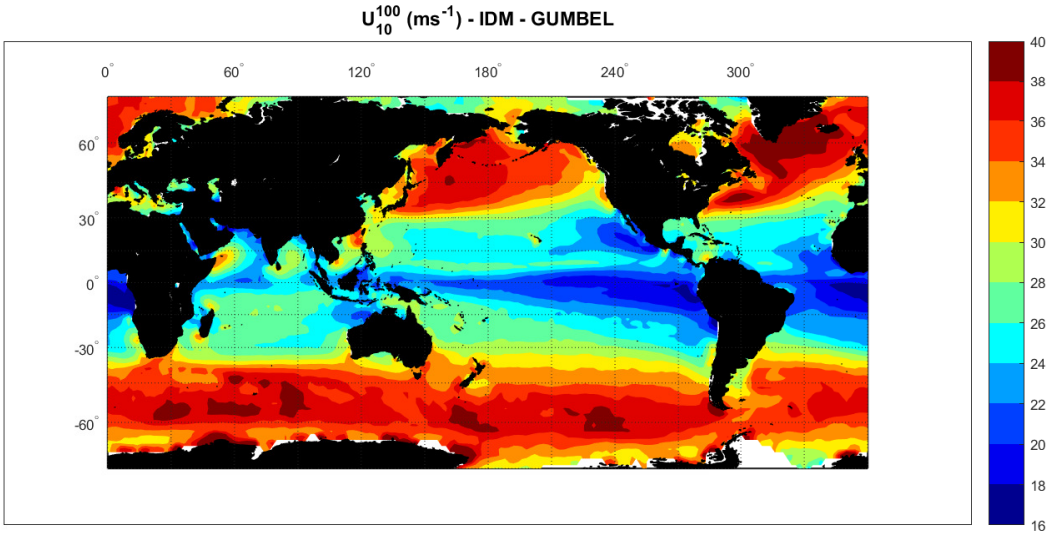

Figure 5.6: Global values of U_{10}^{100} (m s^{-1}) obtained with an IDM analysis and a Gumbel distribution. Data obtained from radiometer missions. The high wind speed correction [(3.3)] applied to the data.

5.4 Comparison of Probability Distribution Functions (PDFs) from PoT and IDM analyses (altimeter)

A location in the Pacific Ocean tropical cyclone belt (6° N, 214° E) and a location off the Horn of Africa (14° N, 60° E) were chosen to emphasise the differences between PDFs from PoT and IDM analyses for wind speed and wave height derived from altimeter data. Figure 5.7 and 5.8 show the PDFs for both wind speed and wave height, together with both IDM and PoT fits to the data. Figure 5.7 shows results from a location in the Pacific Ocean tropical cyclone belt (6° N, 214° E; Figures 5.7a-d, U_{10}; Figures 5.7e-h, H_s), and Figure 5.8 shows results from a location off the Horn of Africa (14° N, 60° E; Figures 5.8a-d, U_{10}; Figures 5.8e-h, H_s). These are two locations where the IDM and PoT analyses give very different results. Figures 5.7a-d show that the PDF of U_{10} has a relatively low wind speed peak at $U_{10} \approx 8$ m s^{-1}, however, an extended high wind speed tail caused by the presence of tropical cyclones. The IDM fits poorly to the tail and underestimates U_{10}^{100}. In contrast, the PoT with a GPD fit to the tail region more accurately approximates the data. The differences for H_s are not as great because the wave field is more uniformly distributed (no local maximum band). As such, the PDF is reasonably well modelled by both IDM and PoT, and the values of H_s^{100} from the two approaches do not differ greatly.

The PDFs for the Horn of Africa (Figure 5.8) are clearly affected by the strong winds of the Somali/Oman CLLJ. The PDFs (both wind speed and wave height) are clearly bimodal and there are clearly two populations of wind speed and wave height. It is also clear that the high wind speed peak (Somali/Oman CLLJ) has a very sharp drop-off with increasing U_{10}. This indicates that, although the winds in the jet are high, there are few really extreme events. Both approaches struggle to model the tail of the PDF. However, the IDM greatly overestimates the tail of the distribution, resulting in a localised peak in U_{10}^{100}, which is not supported by the shape of the PDF, as well as not predicted by the PoT analysis. A similar situation exists for H_s, with the IDM again overestimating the tail of the PDF.

The comparisons between the PoT and IDM analyses above clearly show the limitations of the IDM approach. Although this approach has found favour

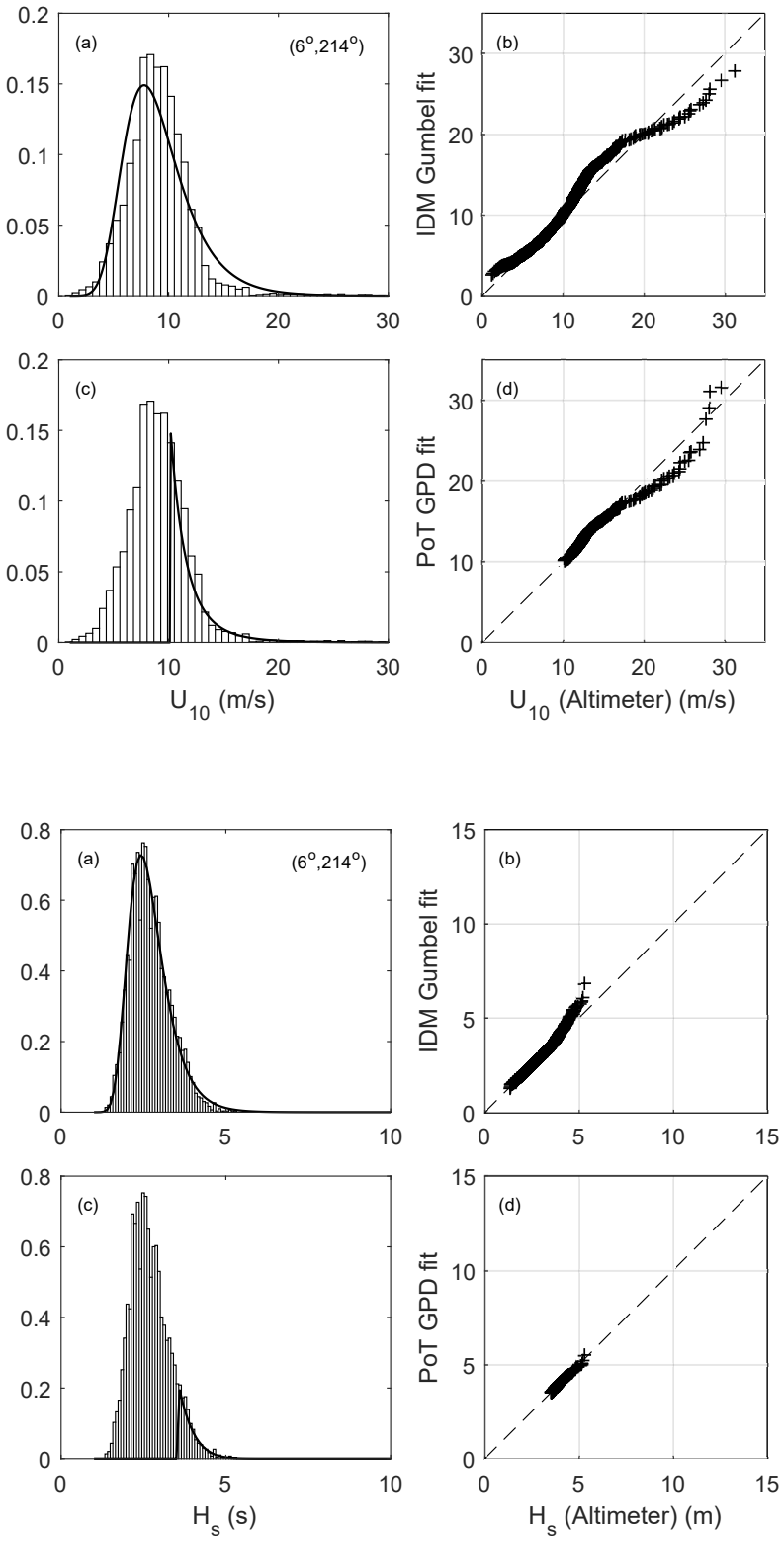

Figure 5.7: The altimeter (left) PDF and (right) QQ-plot at a 2° x 2° square centred on 6° N, 214° E (Pacific tropical cyclone belt) for wind speed U_{10}. (a),(b) The IDM fit to the PDF and (c),(d) the PoT fit to the PDF. (e)–(h) As in (a)–(d), but for wave height H_s.

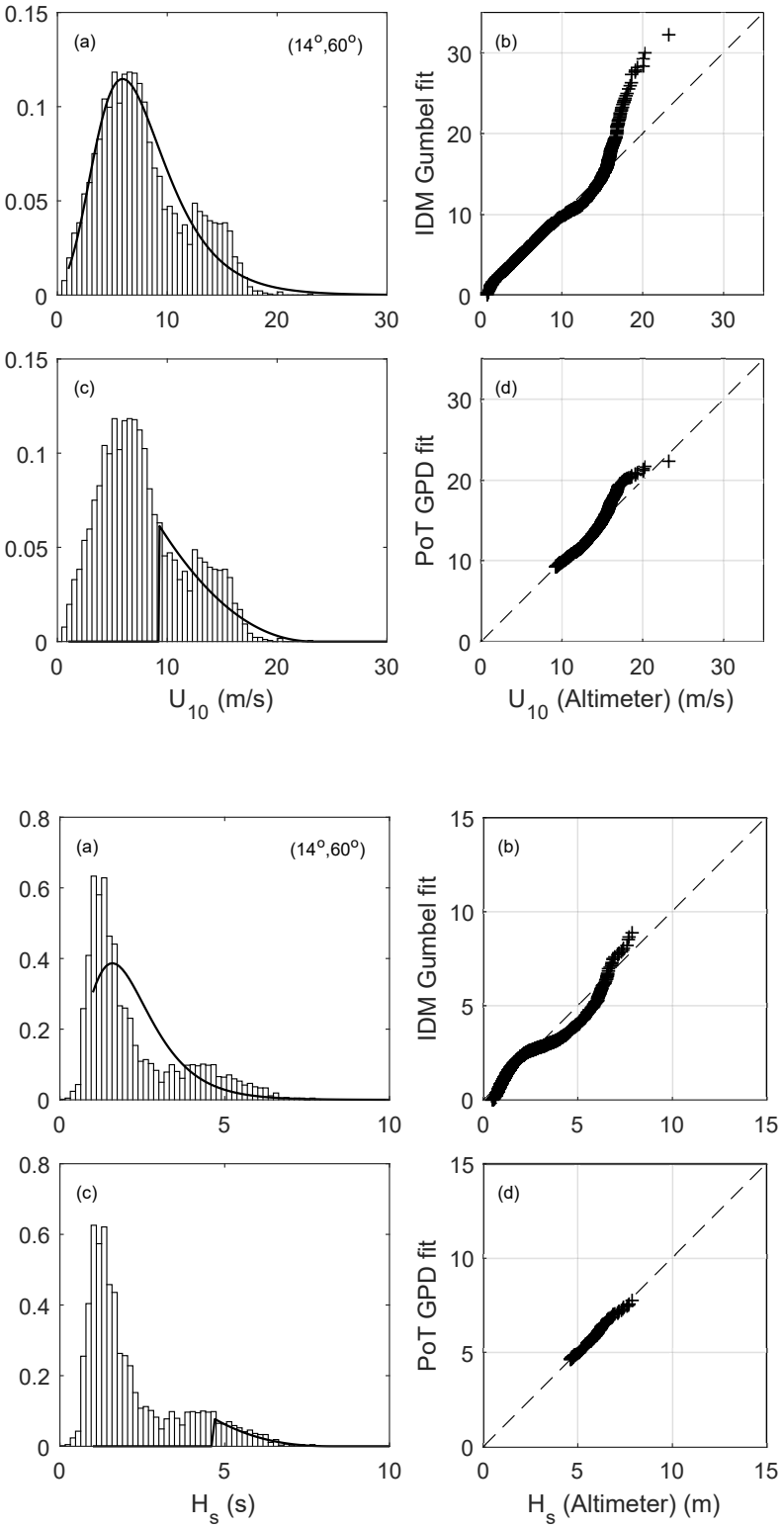

Figure 5.8: As in Figure 5.7, but for a 2° x 2° square centered on 14° N, 60° E (Horn of Africa).

when working with short datasets, the results shown here clearly indicate its significant theoretical and practical shortcomings. As long-duration satellite and model reanalysis datasets are now available, there seems little justification for its continued use.

5.5 Changing wind and wave climates

The above analysis assumes that the time series considered are stationary. That is, there is no change in the mean conditions over the approximately 30-yr measurement period. In addition, applying such extreme-value analysis to determine probable extremes also assumes that mean conditions will not change in the future. There is evidence to suggest that there have been changes in both wind and wave mean climate over this period (Young et al., 2011; Young and Ribal, 2019). In addition, there is also some evidence that extreme conditions have also changed over this period (Young et al., 2011, 2012; Zieger et al., 2014; Young and Ribal, 2019; Ribal and Young, 2019). Further, model studies (Hemer et al., 2013; Morim et al., 2019) indicate that wave climate may also change in the future. At present, there is still a significant level of uncertainty in these trend estimations. The present estimates of both historical and future trends are relatively small (mean H_s trends of approximately 0.5 cm yr^{-1}; mean U_{10} approximately 2 cm s^{-1} yr^{-1}). To date, no reliable assessment of the potential impact on extreme conditions exists.

Using the extensive satellite database of Ribal and Young (2019), Young and Ribal (2019) determined trends in U_{10} and H_s over the 33-year period from 1985 to 2018. They observed small increases in mean wind speed and wave height (similar to values indicated above). However, they showed stronger trends in extremes – the 90th percentiles. Crucial is the regional variability of the trends, especially in the case of U_{10}; The Southern Ocean shows the strongest positive trend for extreme U_{10} with +5 cm s^{-1} yr^{-1} (see their Figure 1B). For H_s, a broad region across the Southern Ocean indicates the highest positive trends of approximately +1 cm yr^{-1} in the 90th percentiles (see their Figure 2B). The regional variation in tends was also observed by Zieger et al. (2014) using altimeter and radiometer measurements.

As the dataset of Ribal and Young (2019) represents an updated version of the database used here, the description above accounts for the observed

non-stationarity of the time series in the present analysis. With that in mind, the impact of the changing (ocean) climate signal on the determination of extreme wave height and wind speed needs further investigations. A potential statistical approach for non-stationary EVA is the transformed-stationary (TS) methodology proposed and described by Mentaschi et al. (2016), which could be a scope of future studies.

At this point, this study will continue with the aim of reducing the confidence interval for the resulting estimates of oceanic extremes (the case of global extreme wave height) by creating a spatial ensemble of data (see Chapter 6).

Chapter 6

The application of EVA to spatial ensembles of wave height data

As discussed in Chapter 5, the first acceptable global estimates of 100-year return period wind speed U_{10}^{100} and significant wave height H_s^{100} were produced using the full 30-year altimeter record in combination with a PoT analysis [cf. Takbash et al. (2019)]. Previous studies that have attempted to apply traditional PoT EVA approaches to such altimeter data (e.g., Vinoth and Young, 2011) have generally not been successful. This is because the time series have been too short to produce estimates of 100-yr wind speed and wave height with acceptable confidence limits. Nevertheless, the present results still show spatial variability of estimates as a result of relatively high statistical variability of these estimates [i.e., large confidence limits (CLs)].

The relevance of the confidence interval (CI) was outlined in Section 2.3 for the case of global extreme wave height. The aim in Chapter 6 is to increase the statistical confidence in the values of H_s^{100} by a significant reduction of the CI on the resulting estimates of these extreme-values. This can be achieved by creating effective (satellite) datasets the equivalent length of which is much longer than the 30-year record of the original data. This has a potential to address the limitations of datasets from buoys and models. As in the case of ocean waves, the time series of measured buoy data in some locations are only as long as 40 years (Evans et al., 2003). Model data can be of any length for which the model is run, although for records longer than approximately 30 years the quality of the wind fields forcing the model declines (Dee et al., 2011).

Following the general concept developed by Breivik et al. (2013, 2014) and Meucci et al. (2018) (see Section 2.3), this chapter explores whether a spatial ensemble of data can be used to reduce potential errors and the magnitude of confidence limits for estimates of H_s^{100}. Both the ERAI reanalysis model dataset and the altimeter dataset of Young et al. (2017) and Ribal and Young (2019) are used as well as the EVA methods described in previous chapters (i.e., PoT analysis) [published in Takbash et al. (2019)]. Rather than pooling independent model forecasts (Breivik et al., 2013, 2014; Meucci et al., 2018), this study explores whether data from a number of independent spatial domains can be combined (pooled) to create a synthetic dataset with an equivalent duration that is the sum of the durations of the separate areas pooled.

To be able to pool data from spatial regions, the data must be independent and identically distributed (Goda, 1988; Coles, 2001; Breivik et al., 2013, 2014). In the present context, these requirements become the following:

1) The regions must be far enough apart that the data from each of the regions are independently distributed (i.e., uncorrelated/poorly correlated). This essentially means that the extreme values are largely generated by different storms.

2) The wave climate in the regions to be pooled must be similar and representative of the larger aggregated region (i.e., identically distributed).

The present approach of pooling spatial ensembles has similarities to the Bayesian hierarchical models (Wikle et al., 1998) used to represent the spatial and temporal variations of H_s through conditional probabilities. These approaches have been used to examine trends in wave height by Vanem et al. (2012a,b).

Criteria that must be met to form such spatial ensembles of data are investigated in detail in Section 6.1. Section 6.2 focuses on the determination of extreme-value estimates of significant wave height using the created spatial ensembles of ERAI and satellite data. This section also examines the resulting CIs from such EVA analysis. The content of Chapter 6 is based on the publication Takbash and Young (2019).

6.1 Spatial ensemble data selection

As outlined above, regions can potentially be pooled for extreme-value analysis if 1) wave heights between regions have low correlation and 2) the regions have comparable wave climate. This section will investigate these criteria globally.

6.1.1 Spatial coherence of waves

To assess the spatial coherence of wave height on a global basis, an approach similar to that adopted by Greenslade and Young (2005), for the analysis of anomaly correlation length scales, is used. In this approach, the aim is to determine the correlation coefficients between specified locations. The low spatial and temporal resolution of the altimeter data (Young et al., 2017), together with the irregular sampling, makes such data difficult to use for such an analysis. Therefore, as an alternative, ERAI reanalysis data (Dee et al., 2011) are investigated for this purpose. The ERAI wave height data are available at 6-hourly intervals on a regular 0.75° spatial grid over the period 1984–2014 (Stopa and Cheung, 2014). ERAI wave height data have been used in several studies to investigate climatology and/or variability of wave height as well as wave height extremes (Shanas and Kumar, 2014, 2015; Aarnes et al., 2015; Kumar et al., 2016; Young and Donelan, 2018). As these studies show reasonable agreement between ERAI and altimeter data both in terms of the magnitude and spatial distribution of wave height, it is adopted here to determine spatial coherence (and climate). The global distribution of oceanic extremes from ERAI data with IDM and PoT analysis are shown in Appendix A.4 on a 0.75° x 0.75° spatial grid.

Specific points (on the 0.75° x 0.75° ERAI grid) in the Pacific, Atlantic, Indian, and Southern Ocean were selected, and the decorrelation length scales of wave height in both zonal and meridional directions were calculated by using the Pearson correlation coefficient (Pearson, 1895; Lee Rodgers and Nicewander, 1988):

$$r(i,j) = \frac{\sum_{l=1}^{m}[H_s(i,l) - \overline{H_s(i)}][H_s(j,l) - \overline{H_s(j)}]}{\sqrt{\sum_{l=1}^{m}[H_s(i,l) - \overline{H_s(i)}]^2}\sqrt{\sum_{l=1}^{m}[H_s(j,l) - \overline{H_s(j)}]^2}}. \tag{6.1}$$

In (6.1), the sample correlation coefficient between points i and j is $r(i,j)$ and the summations are conducted over all $l = 1 : m$ observations of $H_s(l)$ at each location. The overbar terms in (6.1) represent mean quantities that have been evaluated in a number of manners, as described below. The spatial coherence of the wave height field was evaluated using three different approaches. Initially, the monthly variation (monthly mean) was removed from the time series, leading to deseasonalised time series. Thus, time series of fluctuations about the seasonal mean (storms) and any long-term trend (Young and Ribal, 2019) were obtained. Values of $r(i,j)$ were then determined between spatially separated points. That is, from the selected point, $r(i,j)$ was calculated for adjacent points at successively larger spatial separation. This spatial separation was successively increased in all radial directions from the selected point. This process continued until $r(i,j)$ fell below 0.5. Values of constant $r(i,j)$ between 1 and 0.5 were calculated and drawn for representative points in Figure 6.1. The resulting correlation ellipses (CEs) demonstrate the gradual decorrelation of the wave height field with distance for various regions of the globe. As one might expect, the CEs in Figure 6.1 decay more rapidly in the meridional direction than in the zonal direction, indicating larger spatial correlation scales in the zonal direction. This result is similar to the findings of Greenslade and Young (2005).

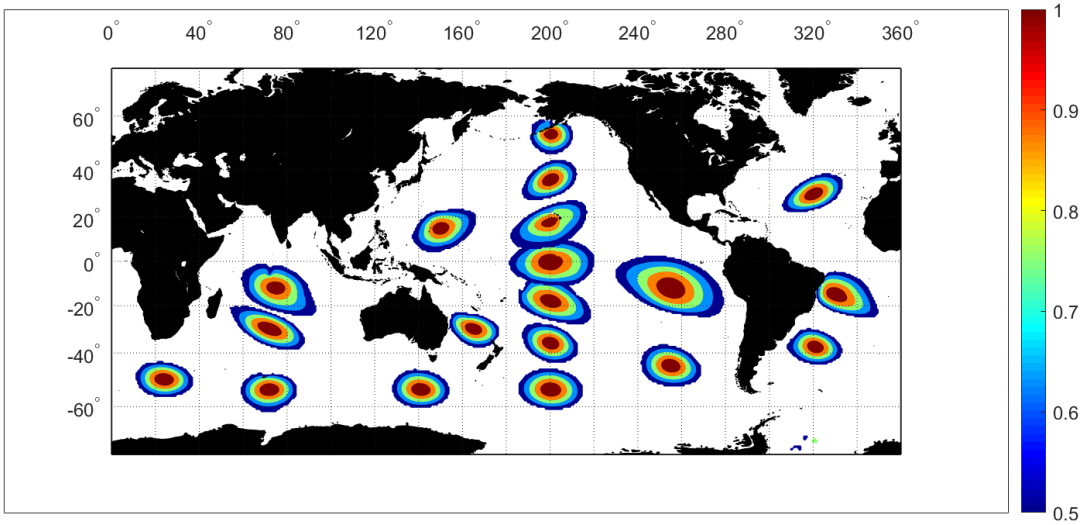

Figure 6.1: Correlation ellipses calculated at specified locations [monthly means subtracted from the time series for application in (6.1)].

The CEs in Figure 6.1 reflect patterns of both swell and wind speed directions: either the predominant direction of propagation of the swell, or the predominant

surface wind direction for local wind sea. In high wind speed zones (storm zones), the predominant wind speed direction aligns with the longest axis of the CE. This is clear for the Southern Ocean, where the correlation length scale is longest along the direction of the strong westerlies. For much of the global oceans, however, it is swell that dominates (Semedo et al., 2011) and the CE longest axis is approximately aligned with the swell crests. This is clear in the Indian and South Pacific Oceans. Here, the great circle propagation paths for swell radiating out from storms in the Southern Ocean align from southwest to northeast. The CE long axis is approximately perpendicular to these great circles, indicating higher spatial correlations in these directions. As one moves from south to north along the line of points through the central Pacific Ocean the CEs change orientation as the wave climate changes from being dominated by Southern Ocean swell to being dominated by North Pacific swell.

The largest CE of these samples (in Figure 6.1) occurs in the eastern Pacific, where the wave field is influenced both by Southern Ocean swell and also southeasterly trade winds. Both of these wave conditions tend to result in CEs with a long axis aligned from northwest to southeast. As both swell and local winds reinforce this orientation, the resulting CE is relatively large.

Areas where local winds dominate the shapes of the CEs (in Figure 6.1) include the central North Atlantic where the CE long axis is aligned from southwest to northeast, the South Atlantic (off South America) where the trade winds result in a CE long axis aligned from northwest to southeast, and the Pacific off the Asian coast where the northeast trades result in a CE long axis aligned from southwest to northeast.

Where the trade winds from both hemispheres converge at the equator (the doldrums) the shape of the CE (in Figure 6.1) becomes symmetric, with the longest axis parallel to the equator. A decrease in anisotropy (see Greenslade and Young, 2005) for the sampled CEs can be seen in the mid-latitudes (centred on 54° N, 200° E) of the Pacific Ocean. The more circular shape of the CE reflects the anticlockwise movement of wind speed in cyclonic systems in the Northern Hemisphere.

In the second approach for calculation of the CEs, the long-term mean was subtracted from time series, rather than the monthly mean. As a result,

the seasonal variation in the time series is retained and, hence the size of the CEs increases (Figure 6.2). This is particularly the case in the mid-latitudes of the Northern Hemisphere, where the seasonal variation is relatively large. At similar latitudes in the Southern Hemisphere, the seasonal variation is much smaller (Young and Donelan, 2018) and hence the CEs are similar in size to Figure 6.1. The general shape and spatial variations of the CEs are, however, still similar to the case where the monthly means were removed (Figure 6.1).

As the focus of this chapter is on extreme wave heights, the third approach used only data greater than the 90th percentile. Again, the monthly mean of the values was subtracted before determining the correlation coefficients. The 90th percentile corresponds to the threshold which was subsequently used in the PoT extreme-value analysis. Therefore, this approach investigates the decorrelation scales of the storm events, rather than all the data. As the amount of data is significantly reduced by applying this threshold, the noise level increases in these calculations (see Appendix A.5). However, the spatial distributions for these approaches remain very similar to Figures 6.1 and 6.2, although the sizes of the CEs are reduced. The reduced correlation scale is as could be expected when considering only extreme conditions. That is, extreme conditions have shorter decorrelation scales than mean conditions. For the present application, large CEs represent a more demanding condition, as this limits the regions that can potentially be pooled for EVA. Therefore, the case shown in Figure 6.1 is

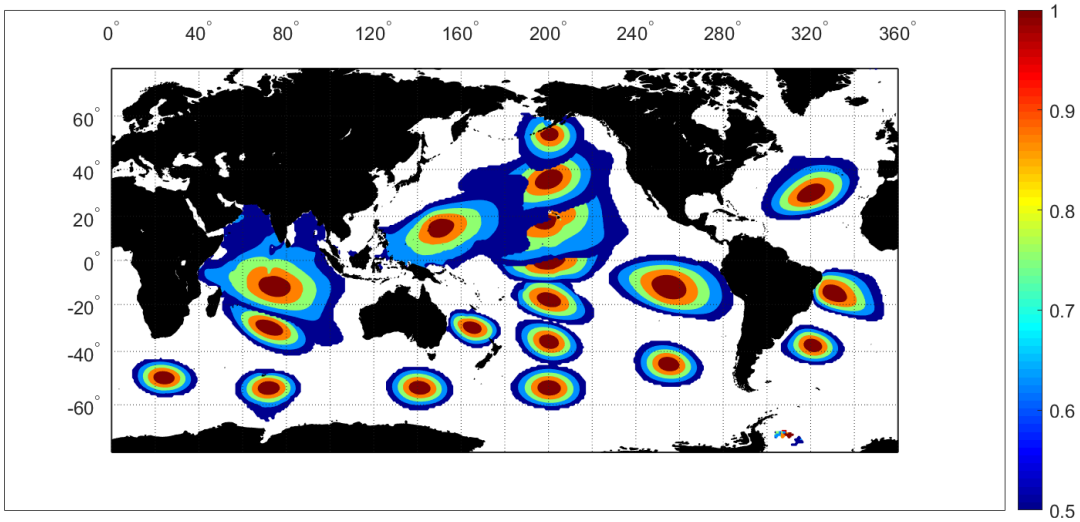

Figure 6.2: Correlation ellipses calculated at specified locations [long-term means subtracted from the time series for application in (6.1)].

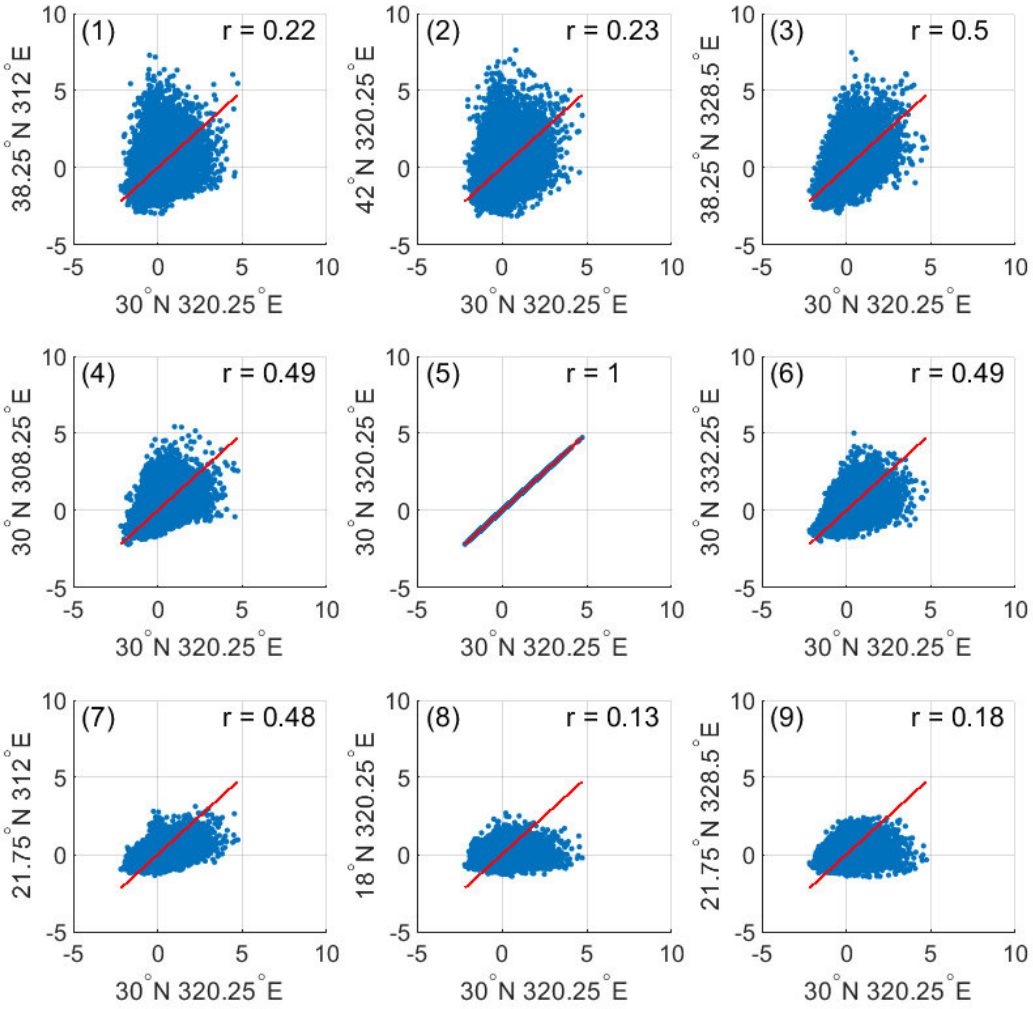

Figure 6.3: Scatter-plots of deseasonalised significant wave height $H_s(i,j) - \overline{H_s}$ between a location at 30° N, 320.25° E and locations surrounding that position at an approximate 12° radius; $\overline{H_s}$ was calculated as the monthly mean. Each panel shows the data scatter, a 1:1 linear relationship line, and the correlation coefficient $r(i,j)$. Data are obtained from ERA-Interim.

the more demanding test and is used in all future analysis.

To further illustrate the spatial variation of correlation, as represented by the CEs, data were considered at one selected CE in the North Atlantic. The location selected was centred on 30° N, 320.25° E. As shown in Figure 6.1, at this point the CE has its long axis aligned from southwest to northeast. Scatter-plots of the deseasonalised $H_s(i,j) - \overline{H_s}$ between this point and neighbouring points on an approximate 12° circle around the point are shown in Figure 6.3. Each

of the nine panels in this figure shows the scatter-plot for $H_s(i,j) - \overline{H_s}$, a 1:1 linear relationship line for the data and the value of $r(i,j)$. Consistent with Figure 6.1, the largest values of $r(i,j)$ lie along the southwest–northeast diagonal (Panels 7, 5, 3) and the smallest values along the northwest–southeast diagonal (Panels 1, 5, 9). The figure also clearly shows the reduction in the magnitude of extremes (variations from the seasonal mean) moving from north to south and the similarity of these extremes in the zonal direction (same latitude). It is also clear that the probability distribution of H_s is skewed, with maximum values further above the mean (zero value in the figure) then minimum values are below the mean.

To illustrate the decorrelation of the storm events at this same location, Figure 6.4 shows similar scatter-plots but for data above the 90th percentile. Panel 1 shows $r(i,j)$ between the location 30° N, 320.25° E and the location 30° N, 332.25° E (i.e., the location 12° east of the point). This corresponds to Panel 6 of Figure 6.3 for the mean conditions. Comparison of the figures shows that $r(i,j)$ reduces from 0.49 for the mean conditions to 0.19 for the storm conditions (i.e., data above 90th percentile). These correlation coefficient calculations consider data at the same times at each of the pairs of points under consideration. As storms propagate in time, it is possible that higher correlation coefficients may result if $r(i,j)$ is determined with a time lag applied at location j. This is investigated in Panel 2 of Figure 6.4. In this panel, the second location j has been lagged by 24 h, relative to location i. As expected, the value of $r(i,j)$ increases to 0.42 when the data are time lagged in this manner. Importantly, however, comparison of Figures 6.3 and 6.4 shows that the decorrelation scales of the storm waves are shorter than the mean conditions. (0.42 compared to 0.49). Testing at a range of locations showed that between points separated by 12°, as in Figures 6.3 and 6.4, a time lag of 24 h produced the largest values of $r(i,j)$. A lag time of 24 h corresponds to a storm propagation speed of approximately 50 km h^{-1}, which seems reasonable. Also, as shown in Figures 6.3 and 6.4, other locations showed that the storm waves are always more poorly correlated (smaller values of r) than the mean conditions.

There is no absolute level of $r(i,j)$ at which one can state that the regions are sufficiently decorrelated to pool. Following (Meucci et al., 2018), the criterion $r(i,j) < 0.5$ was adopted. Under this condition, all neighbouring locations in Figure 6.3, with the exception of locations 3 and 7 (long axis of the CE), can

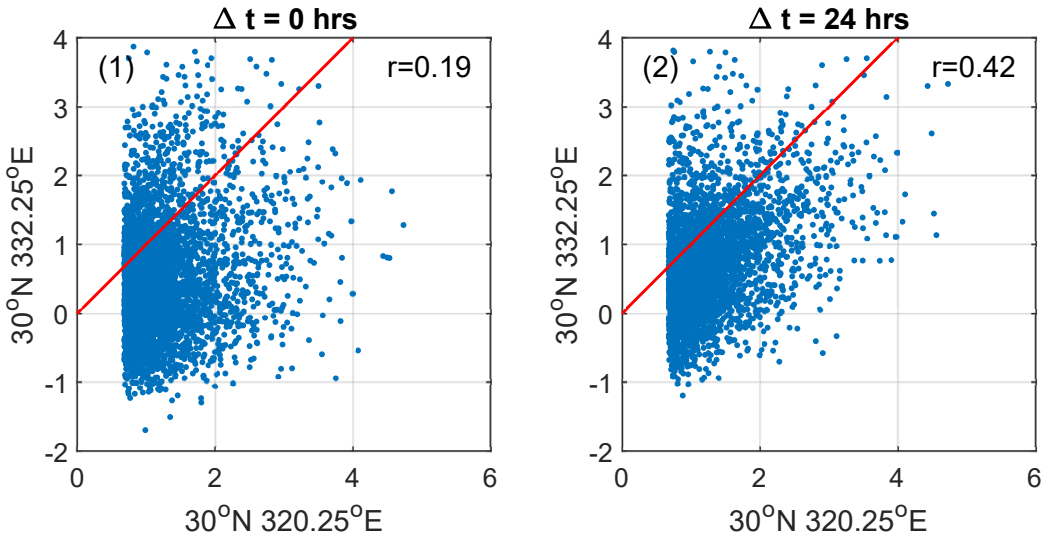

Figure 6.4: Scatter-plots of deseasonalised significant wave height $H_s(i,j) - \overline{H_s}$ between a locations 30° N, 320.25° E and 30° N, 332.25° E (same location as Panel 6 of Figure 6.3). Only data above the 90th percentile are included in the analysis to simulate storm conditions. The data at location 30° N, 332.25° E in Panel 2 have been time-lagged by 24 h to account for the time of storm propagation. Each panel shows the data scatter, a 1:1 linear relationship line, and the correlation coefficient $r(i,j)$. Data are obtained from ERA-Interim.

be potentially pooled with the central location 5. That is, they are deemed to be sufficiently decorrelated that they provide independent storm information. For criteria to determine whether the data are sufficiently decorrelated to pool, $r(i,j)$ was calculated from all the data, even though the interest is in storm conditions. This choice was made as this parameter is a more stable measure. As shown in Figure 6.4, this would generally result in values of $r(i,j) < 0.4$ when storm waves are considered. Hence, using the mean conditions produces a conservative result.

6.1.2 Spatial variation of wave climate

The second criterion for ensemble data pooling requires that areas which have low correlation still have a similar sea state (or wave climate). This was investigated by determining the relative percentage differences of both the mean monthly significant wave height and mean monthly 99th percentile significant wave height

between the two locations:

$$\overline{RPD}(i,j) = \frac{1}{12}\sum_{k=1}^{12}\frac{|\overline{H}_s(i,k) - \overline{H}_s(j,k)|}{\overline{H}_s(i,k)}, \tag{6.2}$$

$$RPD^{99}(i,j) = \frac{1}{12}\sum_{k=1}^{12}\frac{|H_s^{99}(i,k) - H_s^{99}(j,k)|}{H_s^{99}(i,k)}. \tag{6.3}$$

In (6.2) and (6.3), $\overline{RPD}(i,j)$ and $RPD^{99}(i,j)$ are the mean and 99th percentile relative percentage differences between locations i and j respectively; $\overline{H}_s(i,k)$ is the mean monthly significant wave height for location i and month k and $H_s^{99}(i,k)$ is the 99th percentile significant wave height for location i and month k. As the requirement is that there is a similar wave climate at locations i and j in order for them to be spatially pooled, the requirement has been set that both $\overline{RPD}(i,j)$ and $RPD^{99}(i,j)$ are less than 0.1 (this threshold is based on tests shown in Appendices A.6 to A.10). That is, both the mean and 99th percentile conditions differ by less than 10%. This ensures similarity of both the mean conditions and the extremes, which are obviously important for EVA.

Figure 6.5 shows quantile–quantile (QQ) plots between the same locations shown in Figure 6.3 (i.e., North Atlantic). In each panel a linear fit to the QQ data is shown and the values of $\overline{RPD}(i,j)$ and $RPD^{99}(i,j)$. The variation in both the mean wave climate and the extremes are clear in moving from south to north (meridional direction). Locations where the best-fit line to the QQ data is significantly different from 45° signify differing wave climate. Further deviation between the locations are also clear at the upper percentiles in the figure (i.e., extreme sea states differ). Under the conditions that $\overline{RPD}(i,j) < 0.1$ and $RPD^{99}(i,j) < 0.1$, only the locations in the zonal direction, locations 4 and 6, meet this criterion. The similarity of the wave climates between locations 4, 5, and 6 is also clear in the scatter-plot, Figure 6.3. As locations 4 and 6 meet all conditions set [$r(i,j) < 0.5$, $\overline{RPD}(i,j) < 0.1$, $RPD^{99}(i,j) < 0.1$] they could be pooled with location 5 to form a spatial ensemble for EVA. It is possible that further points in the zonal direction could also be pooled, making the spatial ensemble larger. Importantly, this would also further increase the effective duration of the ensemble pooled region. In this case, however, no points in the meridional direction can be pooled, given the changing wave climate in this direction.

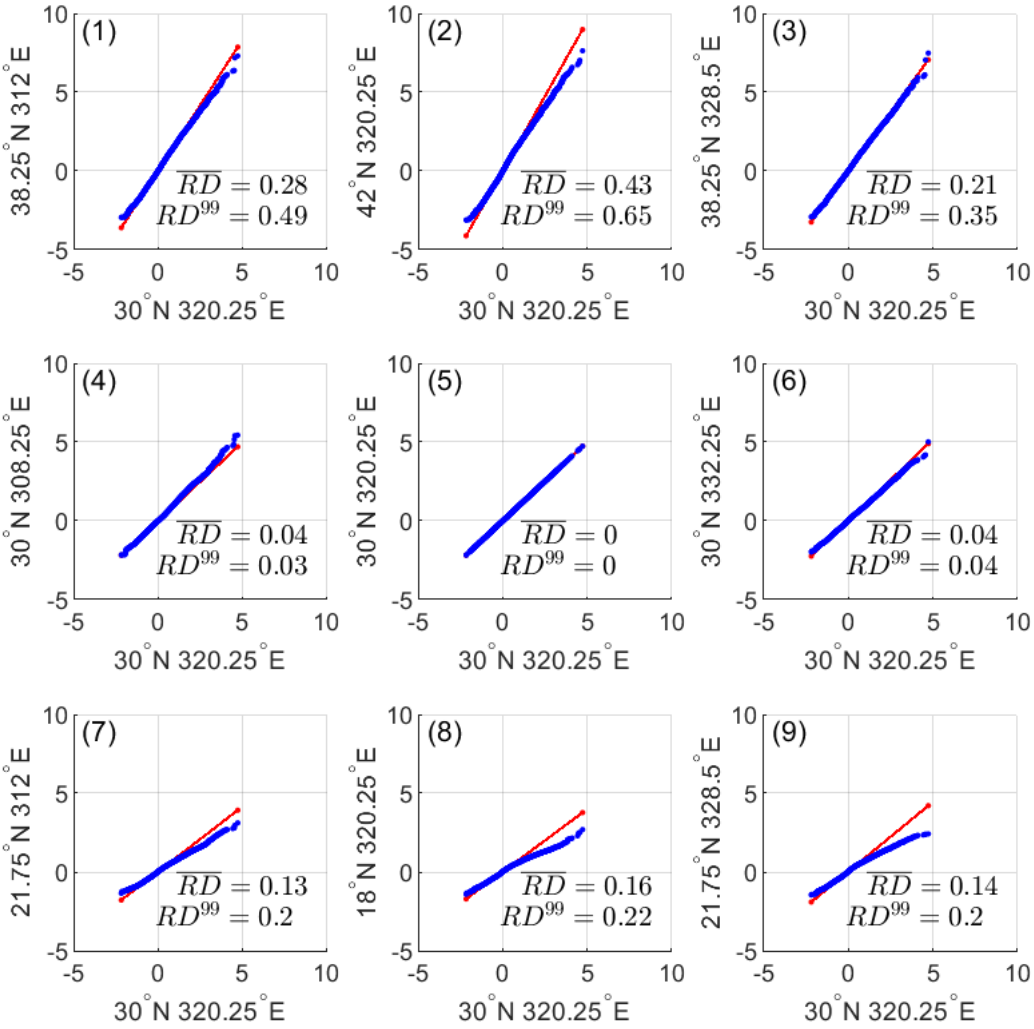

Figure 6.5: QQ-plots of deseasonalised significant wave height $H_s(i,j) - \overline{H_s}$ between a location at 30° N, 320.25° E and locations surrounding that position at an approximate 12° radius; $\overline{H_s}$ is calculated as the monthly mean. Each panel shows the QQ-plot, a least squares linear fit to the QQ data, and the relative percentage differences $\overline{RPD}(i,j)$ and $RPD^{99}(i,j)$. Data are obtained from ERA-Interim.

6.2 Determination of extreme wave height from selected spatial ensemble

With the information on the global spatial variation of $r(i,j)$ and $RPD(i,j)$ provided above, the aim is now to define regions that satisfy the criteria set for

both of these [i.e., $r(i,j) < 0.5$ and $RPD(i,j) < 0.1$]. Note that for simplicity, $RPD(i,j)$ is written to signify both $\overline{RPD}(i,j)$ and $RPD^{99}(i,j)$. With representative areas defined, the data can be pooled for these regions and extreme-value analysis undertaken on the pooled data.

6.2.1 Selection of spatial ensemble regions

The process used to define regions is shown diagrammatically in Figure 6.6. Note that this process to define areas for spatial pooling is based on ERAI reanalysis data. Once the regions are defined, however, it can be applied to either ERAI or altimeter data to determine extreme-value H_s.

(i) An initial location 1 is defined. The process continues in the zonal direction until a location, 2, is found for which $r(1,2) < 0.5$. Then $RPD(1,2) < 0.1$

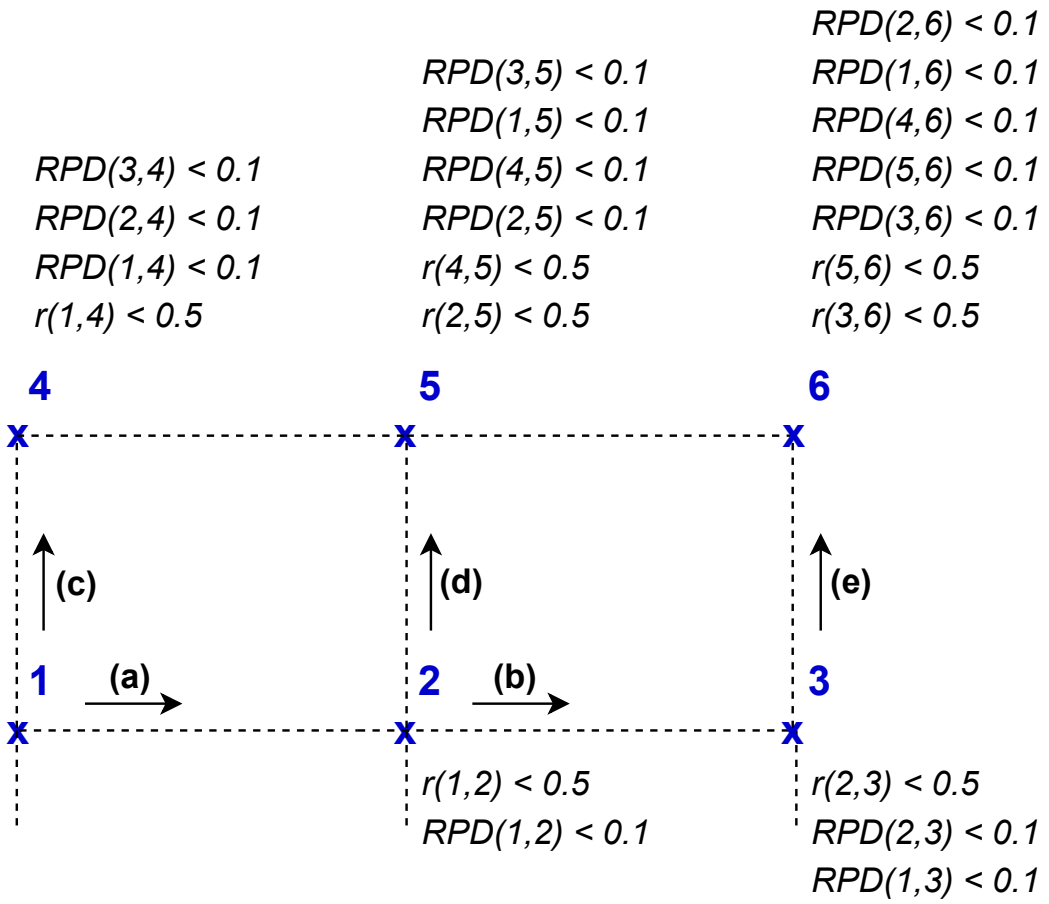

Figure 6.6: The schema used to define regions for spatial ensemble pooling for various oceanic basins.

is checked. If this condition is satisfied, locations 1 and 2 can be pooled for the analysis.

(ii) From location 2 the process continues to move in the zonal direction until location 3 is identified, where $r(2,3) < 0.5$. Then it will be checked that the conditions $RPD(2,3) < 0.1$ and $RPD(1,3) < 0.1$ are satisfied. If both of these conditions are met, then locations 1, 2, and 3 can be pooled. This process continues in the zonal direction until the conditions are no longer met.

(iii) With the extent of the region in the zonal direction defined, the extent in the meridional direction is then explored. Returning to location 1, the process moves in the meridional direction to location 4, where $r(1,4) < 0.5$ and $RPD(1,4) < 0.1$. However, the RPD criteria need to be met for the other combinations of locations, that is, $RPD(2,4) < 0.1$ and $RPD(3,4) < 0.1$. If all conditions are met, location 4 is added to the region.

(iv) Then returning to location 2, the process moves again in the meridional direction to identify 5, where $r(2,5) < 0.5$ and $r(4,5) < 0.5$. Again, all RPD values for all combinations of locations are checked.

(v) The process then returns to location 3, and location 6 is identified in the same manner.

(vi) Note that, for simplicity, the above description and Figure 6.6 consider only locations north of the origin point 1. In reality this same process is mirrored south of the point as well, with all cross-checks for $r(i,j)$ and $RPD(i,j)$ in the whole region considered.

As RPD increases much more rapidly in the meridional direction than the zonal direction, this process tends to define regions with a much greater zonal extent than meridional extent.

Figure 6.7 shows a selection of spatial regions for various oceanic basins that can be pooled using these criteria. As expected, the regions tend to be elongated in the zonal direction, reflecting the similar wave climates that are found at the same latitudes. That is, these shapes tend to be determined by the RPD criteria rather than the r condition. In addition, the spatial extent of the regions is larger at high latitudes, reflecting the greater spatial extent of meteorological systems at these latitudes. The region with the largest spatial

extent is the Southern Ocean, reflecting the relatively uniform wave climate in this area (Young, 1999; Young and Donelan, 2018; Semedo et al., 2011).

6.2.2 Spatial ensemble analysis of extremes

With representative areas defined by the above analysis, the aim is to pool the data for these regions and undertake extreme-value analysis on the pooled data to determine the 100-yr return period significant wave height H_s^{100}. This process was applied to both the ERAI reanalysis data and the altimeter data. In the case of the ERAI data, the total duration of the original dataset is 30 years (1984–2014). As each location to be pooled has a data duration of 30 years, the equivalent duration for the pooled regions will be integral multiples of 30 years. With the selection criteria used here, the pooled regions had an equivalent duration of between 60 and 210 years (mostly 90 years).

The process was also undertaken for the altimeter data. In this case, the original time series again spans 1984–2014, although the effective duration is 27 years, as no satellites were in operation from 1987 to 1990, effectively removing approximately 3 years from the analysis. As a result of the spatial pooling, the resulting effective duration of the pooled areas was between 54 years (two adjacent subareas pooled) and 189 years (seven adjacent subareas pooled).

Following Takbash et al. (2019), both sets of pooled data were analysed using a PoT analysis with a threshold set at the 90th percentile. A generalized Pareto distribution (GPD) was fitted to the data and extrapolated (or interpolated if the equivalent duration of the data was longer than 100 years) to the 100-yr return period probability level. Figure 6.7a shows values of H_s^{100} for each pooled region, calculated from ERAI data (for reference purposes, global values of H_s^{100} are shown contoured from the ERAI 1.5° x 1.5° data in Appendix A.11). The equivalent result from the altimeter data is shown in Figure 6.7b. For reference purposes, global values of H_s^{100} are shown contoured from the original altimeter 2° x 2° data, with each 2° region considered independently (i.e., no pooling) (Figure 6.7c). The values of H_s^{100} for all cases are comparable. Consistent with Section 5.1 and Takbash et al. (2019), the present results show the largest values of $H_s^{100} \approx 18\ m$ in the North Atlantic and North Pacific. The Southern Ocean shows extensive regions of extreme waves heights, with $H_s^{100} \approx 14\ m$ around the globe at latitudes greater than 40° S. Equatorial regions show much lower values with $H_s^{100} \approx 4\ m$. As pointed out by Takbash et al. (2019) both

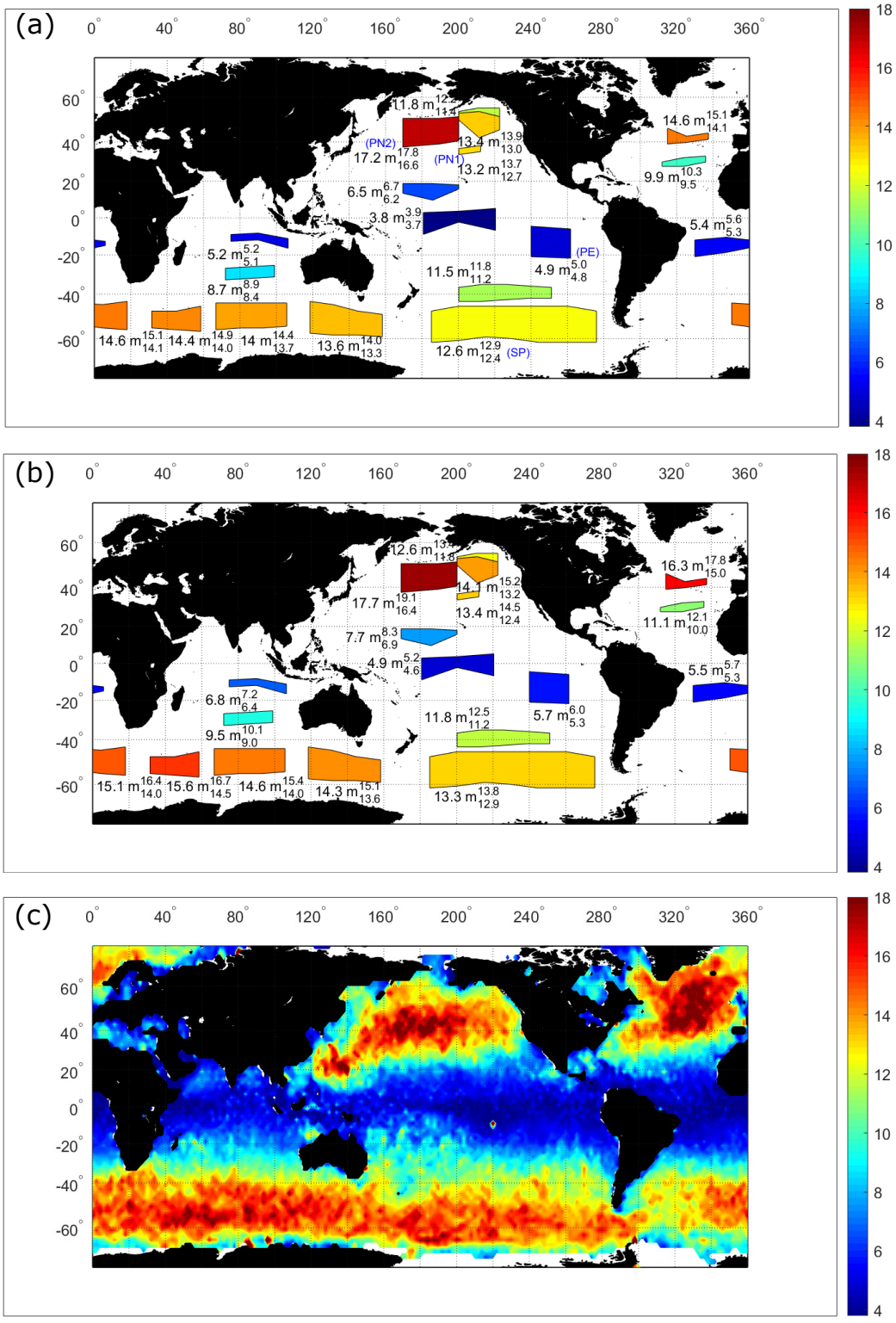

Figure 6.7: (a) Ensemble spatial regions for ERAI data with values of H_s^{100} (m) marked. The upper and lower confidence limits on values of H_s^{100} are shown by the superscripts and subscripts, respectively. (b) Ensemble spatial regions for altimeter data with values of H_s^{100} (m) marked. The upper and lower confidence limits on values of H_s^{100} are shown by the superscripts and subscripts, respectively. (c) Global values of H_s^{100} (m) obtained with a PoT analysis and a GPD distribution. Data are obtained from altimeter missions.

the altimeter data and the ERAI model reanalysis will underestimate tropical cyclone activity, and hence these equatorial values will be underestimated. The ERAI results are consistently lower than the altimeter data, consistent with previous studies which have shown that this dataset underestimates extremes (Stopa and Cheung, 2014). The pooled altimeter data (Figure 6.7b) produce very similar values of H_s^{100} to the 2° data (Figure 6.7c).

6.2.3 Confidence intervals

An examination of Figure 6.7c shows that there is clear statistical noise in the estimates of H_s^{100} brought about by the limited number of observations available to estimate the tail of the PDF and the need to extrapolate to the desired extreme probability level. This results in a relatively large confidence interval and the spatial variability evident in Figure 6.7c. The spatial ensembles shown in Figures 6.7a and 6.7b aimed at reducing these CIs.

To calculate the 95% CLs for the resulting estimates of H_s^{100} a bootstrap method (Efron, 1979; Caires, 2007, 2011; Qi, 2008; Breivik and Aarnes, 2017; Aarnes et al., 2012; Meucci et al., 2018) was applied. In this approach, a sample of 1,000 bootstrapped H_s^{100} estimates taken randomly from the original data sample was computed. For each sample, H_s^{100} was determined and 2.5 percentile and 97.5 percentile values calculated to give the lower and upper 95% confidence limits ($CL^{0.025}$ and $CL^{0.975}$), respectively. The confidence interval is given by $CI^{0.95} = CL^{0.975} - CL^{0.025}$. These values were calculated for each of the spatial ensemble regions and each of the subareas that were pooled to create the ensemble regions. The values of $CL^{0.025}$ and $CL^{0.975}$ are shown for each ensemble region in Figures 6.7a and 6.7b. Table 6.1 shows values of $CI^{0.95}$ for four selected ensemble areas, as well as the subareas that were pooled to create the ensemble regions. The ensemble areas considered in Table 6.1 are marked in Figure 6.7a for reference. Results are shown both for ERAI and altimeter data. Numerical values of H_s^{100}, together with the 95% lower and upper confidence limits ($CL^{0.025}$ and $CL^{0.975}$) are shown on Figures 6.7a and 6.7b for each ensemble region.

Table 6.1 shows that the values of $CI^{0.95}$ for the ERAI subarea data are smaller than for the corresponding altimeter data. This occurs because the ERAI time series is slightly longer (30 years compared to 27 years). In addition, there is less variability in the data from the model compared to the altimeter

measurements. This results in more stable estimates of the tail of the PDF with less variability and hence smaller CIs.

The spatial ensemble pooling results in CIs that are between 30% and 60% smaller than the original data. The magnitude of the reduction increases as the number of subareas making up the spatial ensemble increases. The Southern Ocean/Southern Pacific (SP) is the area where it was possible to pool the largest number of subareas to create the ensemble and this results in an approximately 60% reduction in the CI. In contrast, in the North Pacific (PN1) and Eastern Pacific (PE) it was possible to pool only two subareas, resulting in an approximately 30% reduction in the CI. Farther north in the Pacific (PN2), the spatial correlation scale increases and it is possible to pool four subareas, with a reduction in CI by 40%.

Although the spatial ensemble process can reduce the statistical variability in the extreme-value estimates, it has no impact on any tail bias in the PDF of the data used. As noted previously, the ERA-Interim data underestimate extremes and hence the values of H_s^{100} in Figure 6.7a are smaller than the corresponding altimeter values in Figure 6.7b. Bias correction techniques can be used to address such issues (e.g., Cannon et al., 2015); however, these have not been applied here, as this matter was beyond the scope of this work.

Table 6.1: Values of H_s^{100} (in parentheses) and 95% confidence intervals ($CI^{0.95}$; in italics) for four selected ensemble regions (see Figure 6.7a). The values of H_s^{100} and $CI^{0.95}$ for each of the individual subareas pooled to create the ensemble region are also shown. Values are shown of ERAI data in the left columns and altimeter data in the right columns.

	ERAI: (H_s^{100}) and $CI^{0.95}$ (m)				Altimeter: (H_s^{100}) and $CI^{0.95}$ (m)			
Ensemble region name	PN1	PN2	PE	SP	PN1	PN2	PE	SP
Subarea								
Area 1	(13.8) *1.6*	(17.8) *2.8*	(4.7) *0.3*	(13.1) *1.5*	(13.8) *2.9*	(17.9) *5.7*	(5.8) *1.3*	(13.3) *2.1*
Area 2	(12.5) *1.4*	(17.4) *2.4*	(5.0) *0.3*	(12.7) *1.1*	(12.7) *3.0*	(17.4) *5.2*	(5.5) *0.8*	(13.3) *2.5*
Area 3		(17.3) *2.2*		(12.3) *1.1*		(18.3) *5.4*		(15.1) *3.9*
Area 4		(15.3) *1.9*		(13.0) *1.3*		(16.0) *4.4*		(12.7) *1.7*
Area 5				(12.6) *1.0*				(12.9) *2.1*
Area 6				(12.6) *1.1*				(13.0) *2.2*
Area 7				(11.7) *1.1*				(12.3) *2.5*
Ensemble region	(13.2) *1.0*	(17.2) *1.2*	(4.9) *0.2*	(12.6) *0.5*	(13.4) *2.1*	(17.7) *2.7*	(5.7) *0.7*	(13.3) *0.9*
Percent reduction in $CI^{0.95}$	33%	50%	30%	58%	30%	50%	30%	61%

Chapter 7

Discussion and conclusion

7.1 Summary

The present analysis outlines the application of extreme-value analysis to long-duration (30-year) global altimeter and radiometer datasets. In contrast to previous extreme-value analyses of satellite data, the dataset is sufficiently long to enable a PoT analysis to be undertaken. When applied to altimeter data for U_{10} and H_s, this PoT analysis produces values consistent with buoy validation data and previous numerical model reanalysis datasets. The spatial distributions produced are also consistent with the model reanalysis data. However, the altimeter data show significant fine-scale structure (U_{10}^{100}), which is consistent with known tropical cyclone activity (not generally resolved by reanalysis model datasets). Although the altimeter must under-sample tropical cyclones to some extent, the present results are encouraging and, as the number of altimeter missions continues to increase and the data record expands, the quality of the extreme-value projections will improve further.

The greater data density provided by radiometer measurements offers the potential to address altimeter's under-sampling issues. However, issues associated with the radiometer inability to measure wind speed in heavy rain events appears to create an unacceptable "fair-weather" bias at extreme wind speeds. This renders the radiometer data of U_{10} largely unusable for PoT EVA.

Because of the relatively short duration of altimeter data, previous EVA studies have all used IDM analyses for EVA. The extended dataset presented here can now be successfully processed using the more theoretically sound

PoT approach. The present analysis shows that the IDM yields quite biased estimates of extreme values and their spatial distributions. As the PoT approach can now be successfully applied to the available longer satellite datasets, there seems little reason for IDM analyses to be used in the future.

Nevertheless, these results still show spatial variability of estimates as a result of relatively high statistical variability (i.e., large confidence intervals). Therefore, approaches were investigated to reduce potential errors and the size of confidence limits on the resulting estimates of extremes when applying the PoT approach to altimeter data. That is, the present work investigates further whether data from spatial areas can be pooled to create an ensemble data series, the equivalent length of which is longer than that of the individual areas. Such spatial ensembles of data are then subjected to extreme-value analysis to determine 100-yr return period significant wave height. Following Breivik et al. (2013, 2014) and Meucci et al. (2018) it is shown that in order to pool such data, the areas pooled must be independent and identically distributed. In the present context, independence is achieved by only considering regions that are poorly correlated (i.e., influenced by separate storms). The requirement that the data be identically distributed was assessed by requiring that both the monthly means and monthly 99th percentiles between the areas were in good agreement (comparable wave climate).

Spatial correlation and climate were assessed globally using ERAI reanalysis data, as the ERAI wave height data are available at 6-hourly intervals on a regular 0.75° spatial grid over a period of 30 years. This analysis showed that spatial regions with a long axis in the zonal direction could be pooled to form spatial ensembles. The size of these regions varies by geographic region, with the largest (longest) regions being in the Southern Ocean.

This technique of forming spatial ensembles was applied to both ERAI and altimeter data. The resulting 100-yr return period significant wave heights were similar in magnitude to conventional analyses but have confidence intervals that are reduced by between 30% and 60%. That is, there is greater statistical confidence in the resulting extreme-value estimates.

7.2 Discussion: Limitations and implications

For the case investigated above, it was assumed that the time series considered are stationary (see Section 5.5). That is, there is no change in the mean conditions over the approximately 30-yr measurement period. There is evidence to suggest that there have been changes in both wind and wave mean climate over this period (Young et al., 2011; Young and Ribal, 2019). Besides, there is also some evidence that extreme conditions have also changed over his period (Young et al., 2011, 2012; Zieger et al., 2014; Young and Ribal, 2019; Ribal and Young, 2019). Further, model studies (Hemer et al., 2013; Morim et al., 2019) indicate that the wave climate may also change in the future. At present, there is still a significant level of uncertainty in these trend estimations. To date, no reliable assessment of the potential impact on extreme conditions exists. That is, there is a necessity to use the existing extensive long-duration altimeter satellite dataset (Young et al., 2017; Ribal and Young, 2019) to investigate changes in extreme conditions – whilst accounting for the observed non-stationarity of the time series (Young and Ribal, 2019). That is, quantitative estimates of how global extreme values of wind speed and wave height have changed over the last 30 years need to be investigated.

In this study, it was shown that the resolution of the altimeter data in Tropical Cyclone Regions (TCR) is still limited. Such a condition should be addressed in future work, considering that changes in global extreme values of wind speed and wave height over the last 30 years could be directly related to changes in storm conditions in TCR and along potential coastlines of interest. This could be achieved by augmenting the satellite dataset with high-resolution TCR model data. With a higher resolved and more extensive dataset available, one of the most significant climate change questions – are storms becoming more intense? – could be further addressed. Consequently, changes in these extremes can be interpreted both as a long-term trend but also related to multi-decadal climate oscillations such as the Pacific Decadal Oscillation, El Niño and the Southern Annual Mode.

An additional limitation of the present analysis is the inhomogeneous sampling frequency due to the varying number of operating satellite platforms as a function of time (especially in the case of altimeter devices). Figure 3.1 (in Section 3.2) shows that the lowest sampling frequency of altimeter measurements was between approximately 1985 and 1992 due to the limited number of

operating altimeter systems. The sampling frequency has increased over time with the advent of additional satellite systems and reached the highest sampling frequency between approximately 2002 and 2006. The increase in the available data points over time is assumed to have a direct impact on the existing trends. That is, the more altimeter systems that are operating, the more extremes will be measured. This, in turn, affects the long-term trend of extremes in the time series. That is, the increasing number of satellites as a function of time may result in a spurious trend in observation of extreme conditions.

Furthermore, the relatively low and inhomogeneous global sampling rates of altimeter systems that were pointed out by Zieger et al. (2009), Zieger et al. (2014) and Young et al. (2017) could have a direct effect on fluctuations about the seasonal mean (storms) and any long-term trend (Young and Ribal, 2019), as the possibility that storm peaks are missed are heightened.

As mentioned above, the time series in this work was regarded as stationary. Applying the discussed EVA to determine probable extremes also assumes that mean conditions will not change in the future. Although the observed trends are relatively small, there is a need for a trend-based (i.e. non-stationary) extreme-value analysis to address changing ocean climates. Adopting the statistical approach of Mentaschi et al. (2016) and applying their transformed-stationary (TS) methodology for non-stationary EVA could present a solution to this limitation.

Another limitation of the analyses adopted here is the spatial resolution of the results. For the determination of the global distribution of extreme significant wave height and wind speed, data were aggregated into a 2° x 2° grid. This ensured there were sufficient data points in each 2° region to form stable statistics. Although Vinoth and Young (2011) showed that a coarser spatial resolution improves the results of global extreme-value estimation, especially when considering the PoT approach, the global contour maps presented here might be considered as best available “models” rather than the true representation of global distributions of extremes. From this perspective, creating a global ensemble of pooled data is also limited by the spatial resolution of the presented results. As might be expected, this limitation can only be addressed as the length and density of the altimeter data record increases.

Despite the limitations discussed above, the presented analyses have clearly shown the potential for altimeter data to provide high-quality estimates of global extreme wind speed and wave height.

The extensive, log-term, calibrated and validated altimeter satellite data used in this study are archived on the Australian Ocean Data Network [(AODN), `https://portal.aodn.org.au/`] and free for public access.

7.3 Conclusion and outlook

The achievements described above are original and represent a significant advance in the determination of oceanic design parameters. The present work shows, for the first time, that stable results can be achieved using PoT approaches and the altimeter dataset. In addition, both an understanding of the spatial coherence of wind/wave fields and the determination of extreme-value estimates using a spatial ensemble of satellite data represent a significant advance in the field. Both elements of the research were published in a high-quality international journal: The Journal of Climate.

The impacts of the changing climate signal on extremes represents a significant opportunity for future studies. This will be a relevant new field of research as, to date, no scientific consensus exists on whether extreme wind speeds and wave heights are increasing as a result of climate change.

Bibliography

Aarnes, O. J., Abdalla, S., Bidlot, J.-R., and Breivik, Ø. (2015). Marine wind and wave height trends at different ERA-Interim forecast ranges. *Journal of Climate*, 28(2):819–837. https://doi.org/10.1175/JCLI-D-14-00470.1.

Aarnes, O. J., Breivik, Ø., and Reistad, M. (2012). Wave extremes in the northeast Atlantic. *Journal of Climate*, 25(5):1529–1543. https://doi.org/10.1175/JCLI-D-11-00132.1.

Abdalla, S. (2007). Ku-band radar altimeter surface wind speed algorithm. *Proc. Envisat Symposium 2007*, Montreux, Switzerland, European Centre for Medium-Range Weather Forecasts, 463250. URL: https://earth.esa.int/envisatsymposium/proceedings/sessions/3E4/463250sa.pdf.

Alves, J. H. G. and Young, I. R. (2003). On estimating extreme wave heights using combined Geosat, Topex/Poseidon and ERS-1 altimeter data. *Applied Ocean Research*, 25(4):167–186. https://doi.org/10.1016/j.apor.2004.01.002.

Amrutha, M., Kumar, V. S., Sandhya, K., Nair, T. B., and Rathod, J. (2016). Wave hindcast studies using SWAN nested in WAVEWATCH III-comparison with measured nearshore buoy data off Karwar, eastern Arabian Sea. *Ocean Engineering*, 119:114–124. https://doi.org/10.1016/j.oceaneng.2016.04.032.

Anderson, C., Carter, D., and Cotton, P. (2001). Wave climate variability and impact on offshore design extremes. Shell International Report, 88 pp.

AODN (2020). Open Access to Ocean Data. The Australian Ocean Data Network. Viewed 10. February 2020. https://portal.aodn.org.au/.

Ardhuin, F., Aksenov, Y., Benetazzo, A., Bertino, L., Brandt, P., Caubet, E., Chapron, B., Collard, F., Cravatte, S., Delouis, J.-M., et al. (2018). Measuring currents, ice drift, and waves from space: the Sea surface KInemat-

ics Multiscale monitoring (SKIM) concept. *Ocean Science*, 14(3):337–354. https://doi.org/10.5194/os-14-337-2018.

Bender, L. C., III., Guinasso Jr., N., Walpert, J. N., and Howden, S. D. (2010). A comparison of methods for determining significant wave heights—Applied to a 3-m discus buoy during Hurricane Katrina. *Journal of Atmospheric and Oceanic Technology*, 27(6):1012–1028. https://doi.org/10.1175/2010JTECHO724.1.

Bitner-Gregersen, E. M., Ewans, K. C., and Johnson, M. C. (2014). Some uncertainties associated with wind and wave description and their importance for engineering applications. *Ocean Engineering*, 86:11–25. https://doi.org/10.1016/j.oceaneng.2014.05.002.

Breivik, Ø. and Aarnes, O. J. (2017). Efficient bootstrap estimates for tail statistics. *Natural Hazards and Earth System Sciences*, 17(3):357–366. https://doi.org/10.5194/nhess-17-357-2017.

Breivik, Ø., Aarnes, O. J., Abdalla, S., Bidlot, J.-R., and Janssen, P. A. (2014). Wind and wave extremes over the world oceans from very large ensembles. *Geophysical Research Letters*, 41(14):5122–5131. https://doi.org/10.1002/2014GL060997.

Breivik, Ø., Aarnes, O. J., Bidlot, J.-R., Carrasco, A., and Saetra, Ø. (2013). Wave extremes in the northeast Atlantic from ensemble forecasts. *Journal of Climate*, 26(19):7525–7540. https://doi.org/10.1175/JCLI-D-12-00738.1.

Bulgakov, K., Kuzmin, V., and Shilov, D. (2018). Evaluation of extreme wave probability on the basis of long-term data analysis. *Ocean Science*, 14(5):1321–1327. https://doi.org/10.5194/os-14-1321-2018.

Caires, S. (2007). Extreme wave statistics: confidence intervals. Tech. Rep., Delft Hydraulics, prepared for Rijkswaterstaat, Rijksinstituut voor Kust en Zee, 32 pp. http://resolver.tudelft.nl/uuid:8d38ef9c-ead4-4b9d-850c-d4dd2e71a34f.

Caires, S. (2011). Extreme value analysis: wave data. JCOMM Tech. Rep. 57, 33 pp. http://hdl.handle.net/11329/367.

Caires, S. and Sterl, A. (2003). Validation of ocean wind and wave data using triple collocation. *Journal of Geophysical Research: Oceans*, 108(C3):43/1–16. https://doi.org/10.1029/2002JC001491.

Caires, S. and Sterl, A. (2005). 100-year return value estimates for ocean wind

speed and significant wave height from the ERA-40 data. *Journal of Climate*, 18(7):1032–1048. https://doi.org/10.1175/JCLI-3312.1.

Cannon, A. J., Sobie, S. R., and Murdock, T. Q. (2015). Bias correction of GCM precipitation by quantile mapping: How well do methods preserve changes in quantiles and extremes? *Journal of Climate*, 28(17):6938–6959. https://doi.org/10.1175/JCLI-D-14-00754.1.

Castillo, E. (1988). *Extreme Value Theory in Engineering*. Academic Press, 389 pp.

Challenor, P., Wimmer, W., and Ashton, I. (2005). Climate change and extreme wave heights in the North Atlantic. *Proc. 2004 Envisat and ERS Symposium*, Salzburg, Austria, European Space Agency, Sp-572.

Chen, G., Bi, S.-W., and Ezraty, R. (2004). Global structure of extreme wind and wave climate derived from TOPEX altimeter data. *International Journal of Remote Sensing*, 25(5):1005–1018. https://doi.org/10.1080/01431160310001598980.

CMEMS (n.d.). Global Ocean Waves Reanalysis WAVERYS. Copernicus - Marine Environment Monitoring Service. Viewed 17. April 2020. https://resources.marine.copernicus.eu/?option=com_csw&task=results?option=com_csw&view=details&product_id=GLOBAL_REANALYSIS_WAV_001_032.

Coles, S. (2001). *An Introduction to Statistical Modeling of Extreme Values*. Springer, 208 pp.

Cooper, C. K. and Forristall, G. Z. (1997). The use of satellite altimeter data to estimate the extreme wave climate. *Journal of Atmospheric and Oceanic Technology*, 14(2):254–266. https://doi.org/10.1175/1520-0426(1997)014<0254:TUOSAD>2.0.CO;2.

Dee, D. P., Uppala, S., Simmons, A., Berrisford, P., Poli, P., Kobayashi, S., Andrae, U., Balmaseda, M., Balsamo, G., Bauer, d. P., et al. (2011). The ERA-Interim reanalysis: Configuration and performance of the data assimilation system. *Quarterly Journal of the royal meteorological society*, 137(656):553–597. https://doi.org/10.1002/qj.828.

ECMWF (n.d.). ERA5. European Centre for Medium-Range Weather Forecasts. Viewed 10. February 2020. https://www.ecmwf.int/en/forecasts/datasets/reanalysis-datasets/era5.

Efron, B. (1979). Bootstrap methods: another look at the jackknife annals of

statistics 7: 1–26. *The Annals of Statistics*, 7:1–26. https://doi.org/10.1214/aos/1176344552.

Embrechts, P., Klüppelberg, C., and Mikosch, T. (1997). *Modelling Extremal Events*. Springer, 648 pp.

Evans, D., Conrad, C., and Paul, F. (2003). Handbook of automated data quality control checks and procedures of the National Data Buoy Center. NOAA National Data Buoy Center Tech. Document 03–02, 44 pp.

Evans, M., Hastings, N., and Peacock, B. (2000). *Statistical Distributions*. John Wiley & Sons, 248 pp.

Ewans, K. and Jonathan, P. (2014). Evaluating environmental joint extremes for the offshore industry using the conditional extremes model. *Journal of Marine Systems*, 130:124–130. https://doi.org/10.1016/j.jmarsys.2013.03.007.

Ferreira, J. and Soares, C. G. (1998). An application of the peaks over threshold method to predict extremes of significant wave height. *Journal of Offshore Mechanics and Arctic Engineering*, 120(3):165–176. https://doi.org/10.1115/1.2829537.

Fisher, R. A. and Tippett, L. H. C. (1928). Limiting forms of the frequency distribution of the largest or smallest member of a sample. *Mathematical Proceedings of the Cambridge Philosophical Society*, volume 24, Cambridge University Press, 24:180–190. https://doi.org/10.1017/S0305004100015681.

Forbes, C., Evans, M., Hastings, N., and Peacock, B. (2011). *Statistical distributions*. John Wiley & Sons, 212 pp.

Gibson, J., Kållberg, P., Uppala, S., Hernandez, A., Nomura, A., and Serrano, E. (1997). ERA Description. ECMWF, 72 pp. URL: https://www.ecmwf.int/node/9584.

Goda, Y. (1988). On the methodology of selecting design wave height. *Proc. 21st Int. Conf. Coastal Eng.*, Malaga, Spain, American Society of Civil Engineers, 899–913.

Goda, Y. (1992). Uncertainty of design parameters from viewpoint of extreme statistics. *Journal of offshore mechanics and arctic engineering*, 114(2):76–82. https://doi.org/10.1115/1.2919962.

Goda, Y. (2010). *Random seas and design of maritime structures*. World scientific, 443 pp.

Greenslade, D. J. and Young, I. R. (2005). The impact of altimeter sampling patterns on estimates of background errors in a global wave model. *Journal of Atmospheric and Oceanic Technology*, 22(12):1895–1917. https://doi.org/10.1175/JTECH1811.1.

Hasselmann, S., Hasselmann, K., Bauer, E., Janssen, P., Komen, G., Bertotti, L., Lionello, P., Guillaume, A., Cardone, V., Greenwood, J., et al. (1988). The WAM Model – A 3rd generation ocean wave prediction model. *Journal of Physical Oceanography*, 18(12):1775–1810. https://doi.org/10.1175/1520-0485(1988)018<1775:TWMTGO>2.0.CO;2.

Hauser, D., Tison, C., Amiot, T., Delaye, L., Corcoral, N., and Castillan, P. (2017). SWIM: the first spaceborne wave scatterometer. *IEEE Transactions on Geoscience and Remote Sensing*, 55(5):3000–3014. https://doi.org/10.1109/TGRS.2017.2658672.

Hemer, M. A., Fan, Y., Mori, N., Semedo, A., and Wang, X. L. (2013). Projected changes in wave climate from a multi-model ensemble. *Nature climate change*, 3(5):471–476. https://doi.org/10.1038/nclimate1791.

Hogben, N. (1988). Experience from compilation of global wave statistics. *Ocean engineering*, 15(1):1–31. https://doi.org/10.1016/0029-8018(88)90017-0.

Howden, S., Gilhousen, D., Guinasso, N., Walpert, J., Sturgeon, M., and Bender, L. (2008). Hurricane Katrina winds measured by a buoy-mounted sonic anemometer. *Journal of Atmospheric and Oceanic Technology*, 25(4):607–616. https://doi.org/10.1175/2007JTECHO518.1.

Jensen, R., Swail, V., Bouchard, R., Riley, R., Hesser, T., Blaseckie, M., and MacIsaac, C. (2015). Field Laboratory for Ocean Sea State Investigation and Experimentation: FLOSSIE: Intra-measurement evaluation of 6N wave buoy systems. *14th Int. Workshop on Wave Hindcasting and Forecasting and Fifth Coastal Hazard Symposium*, Key West, FL, WMO/IOC JCOMM, A1. URL: http://www.waveworkshop.org/14thWaves/Papers/WW14%20FLOSSIE%20Jensen%20et%20al.pdf.

Jonathan, P. and Ewans, K. (2013). Statistical modelling of extreme ocean environments for marine design: a review. *Ocean Engineering*, 62:91–109. https://doi.org/10.1016/j.oceaneng.2013.01.004.

Jonathan, P., Ewans, K., and Randell, D. (2013). Joint modelling of extreme ocean environments incorporating covariate effects. *Coastal Engineering*, 79:22–31. https://doi.org/10.1016/j.coastaleng.2013.04.005.

Jonathan, P., Randell, D., Wu, Y., and Ewans, K. (2014). Return level estimation from non-stationary spatial data exhibiting multidimensional covariate effects. *Ocean Engineering*, 88:520–532. https://doi.org/10.1016/j.oceaneng.2014.07.007.

Jones, M., Randell, D., Ewans, K., and Jonathan, P. (2016). Statistics of extreme ocean environments: Non-stationary inference for directionality and other covariate effects. *Ocean Engineering*, 119:30–46. https://doi.org/10.1016/j.oceaneng.2016.04.010.

Knapp, K. R., Kruk, M. C., Levinson, D. H., Diamond, H. J., and Neumann, C. J. (2010). The international best track archive for climate stewardship (IBTrACS) unifying tropical cyclone data. *Bulletin of the American Meteorological Society*, 91(3):363–376. https://doi.org/10.1175/2009BAMS2755.1.

Kong, Y., Zhang, X., Sheng, L., and Chen, B. (2016). Validation and application of multi-source altimeter wave data in China's offshore areas. *Acta Oceanologica Sinica*, 35(11):86–96. https://doi.org/10.1007/s13131-016-0951-5.

Kumar, P., Min, S.-K., Weller, E., Lee, H., and Wang, X. L. (2016). Influence of climate variability on extreme ocean surface wave heights assessed from ERA-Interim and ERA-20C. *Journal of Climate*, 29(11):4031–4046. https://doi.org/10.1175/JCLI-D-15-0580.1.

Large, W., Morzel, J., and Crawford, G. (1995). Accounting for surface wave distortion of the marine wind profile in low-level ocean storms wind measurements. *Journal of Physical Oceanography*, 25(11):2959–2971. https://doi.org/10.1175/1520-0485(1995)025<2959:AFSWDO>2.0.CO;2.

Lee Rodgers, J. and Nicewander, W. A. (1988). Thirteen ways to look at the correlation coefficient. *The American Statistician*, 42(1):59–66. https://doi.org/10.1080/00031305.1988.10475524.

Lewis, J. M. (2005). Roots of ensemble forecasting. *Monthly weather review*, 133(7):1865–1885. https://doi.org/10.1175/MWR2949.1.

Lopatoukhin, L., Rozhkov, V., Ryabinin, V., Swail, V., Boukhanovsky, A., and Degtyarev, A. (2000). Estimation of extreme wind wave heights. WMO/TD-No. 1041, 84 pp.

Mathiesen, M., Goda, Y., Hawkes, P. J., Mansard, E., Martín, M. J., Peltier, E., Thompson, E. F., and Van Vledder, G. (1994). Recommended practice for extreme wave analysis. *Journal of Hydraulic Research*, 32(6):803–814.

https://doi.org/10.1080/00221689409498691.

Mazas, F. and Hamm, L. (2011). A multi-distribution approach to POT methods for determining extreme wave heights. *Coastal Engineering*, 58(5):385–394. https://doi.org/10.1016/j.coastaleng.2010.12.003.

Mazas, F. and Hamm, L. (2017). An event-based approach for extreme joint probabilities of waves and sea levels. *Coastal Engineering*, 122:44–59. https://doi.org/10.1016/j.coastaleng.2017.02.003.

Meade, B., Lafayette, L., Sauter, G., and Tosello, D. (2017). Spartan HPC-Cloud Hybrid: Delivering Performance and Flexibility. *University of Melbourne*. Online resource. https://doi.org/10.4225/49/58ead90dceaaa.

Mentaschi, L., Vousdoukas, M., Voukouvalas, E., Sartini, L., Feyen, L., Besio, G., and Alfieri, L. (2016). The transformed-stationary approach: a generic and simplified methodology for non-stationary extreme value analysis. *Hydrology & Earth System Sciences*, 20(9):3527–3547. https://doi.org/10.5194/hess-20-3527-2016.

Meucci, A., Young, I. R., and Breivik, Ø. (2018). Wind and wave extremes from atmosphere and wave model ensembles. *Journal of Climate*, 31(21):8819–8842. https://doi.org/10.1175/JCLI-D-18-0217.1.

Morim, J., Hemer, M., Wang, X. L., Cartwright, N., Trenham, C., Semedo, A., Young, I., Bricheno, L., Camus, P., Casas-Prat, M., et al. (2019). Robustness and uncertainties in global multivariate wind-wave climate projections. *Nature Climate Change*, 9(9):711–718. https://doi.org/10.1038/s41558-019-0542-5.

Muir, L. R. and El-Shaarawi, A. (1986). On the calculation of extreme wave heights: A review. *Ocean Engineering*, 13(1):93–118. https://doi-org.ezp.lib.unimelb.edu.au/10.1016/0029-8018(86)90006-5.

NOAA (n.d.). WAVEWATCH III® 30-year Hindcast Phase 2. The National Oceanic and Atmospheric Administration - Environmental Modeling Center / Marine Modeling and Analysis Branch. Viewed 17. April 2020. https://polar.ncep.noaa.gov/waves/hindcasts/nopp-phase2.php.

Ochi, M. K. (1992). New approach for estimating the severest sea state from statistical data. *Proc. Coastal Eng. Conf.*, New York, NY, American Society of Civil Engineers, 512–525.

Pearson, K. (1895). VII. Note on regression and inheritance in the case of two parents. *proceedings of the royal society of London*, 58(347-352):240–242.

https://doi.org/10.1098/rspl.1895.0041.

Ponce de León, S. and Bettencourt, J. (2019). Composite analysis of North Atlantic extra-tropical cyclone waves from satellite altimetry observations. *Advances in Space Research*, In Press. https://doi.org/10.1016/j.asr.2019.07.021.

Ponce de León, S. and Guedes Soares, C. (2014). Extreme wave parameters under North Atlantic extratropical cyclones. *Ocean Modelling*, 81:78–88. https://doi.org/10.1016/j.ocemod.2014.07.005.

Qi, Y. (2008). Bootstrap and empirical likelihood methods in extremes. *Extremes*, 11(1):81–97. https://doi.org/10.1007/s10687-007-0049-8.

Randell, D., Turnbull, K., Ewans, K., and Jonathan, P. (2016). Bayesian inference for nonstationary marginal extremes. *Environmetrics*, 27(7):439–450. https://doi.org/0.1002/env.2403.

Ranjha, R., Tjernström, M., Semedo, A., Svensson, G., and Cardoso, R. M. (2015). Structure and variability of the Oman coastal low-level jet. *Tellus A: Dynamic Meteorology and Oceanography*, 67(1):25285. https://doi.org/10.3402/tellusa.v67.25285.

Ribal, A. and Young, I. R. (2019). 33 years of globally calibrated wave height and wind speed data based on altimeter observations. *Scientific data*, 6(1):77. https://doi.org/10.1038/s41597-019-0083-9.

Semedo, A., Sušelj, K., Rutgersson, A., and Sterl, A. (2011). A global view on the wind sea and swell climate and variability from ERA-40. *Journal of Climate*, 24(5):1461–1479. https://doi.org/10.1175/2010JCLI3718.1.

Shanas, P. and Kumar, V. S. (2014). Temporal variations in the wind and wave climate at a location in the eastern Arabian Sea based on ERA-Interim reanalysis data. *Natural Hazards and Earth System Sciences*, 14(5):1371–1381. https://doi.org/10.5194/nhess-14-1371-2014.

Shanas, P. and Kumar, V. S. (2015). Trends in surface wind speed and significant wave height as revealed by ERA-Interim wind wave hindcast in the Central Bay of Bengal. *International Journal of Climatology*, 35(9):2654–2663. https://doi.org/10.1002/joc.4164.

Sterl, A. and Caires, S. (2005). Climatology, variability and extrema of ocean waves: The Web-based KNMI/ERA-40 wave atlas. *International Journal of Climatology*, 25(7):963–977. https://doi.org/10.1002/joc.1175.

Stopa, J. E. and Cheung, K. F. (2014). Intercomparison of wind and wave data

from the ECMWF Reanalysis Interim and the NCEP Climate Forecast System Reanalysis. *Ocean Modelling*, 75:65–83. https://doi.org/10.1016/j.ocemod.2013.12.006.

Takbash, A. and Young, I. R. (2019). Global Ocean Extreme Wave Heights from Spatial Ensemble Data. *Journal of Climate*, 32(20):6823–6836. https://doi.org/10.1175/JCLI-D-19-0255.1.

Takbash, A., Young, I. R., and Breivik, Ø. (2019). Global wind speed and wave height extremes derived from long-duration satellite records. *Journal of Climate*, 32(1):109–126. https://doi.org/10.1175/JCLI-D-18-0520.1.

Taylor, P. K. and Yelland, M. J. (2001). Comments on "On the effect of ocean waves on the kinetic energy balance and consequences for the inertial dissipation technique". *Journal of Physical Oceanography*, 31(8):2532–2536. https://doi.org/10.1175/1520-0485(2001)031<2532:COOTEO>2.0.CO;2.

Teng, C.-C. (1998). Long-term and extreme waves in the Gulf of Mexico. *Ocean Wave Kinematics, Dynamics and Loads on Structures*, Houston, TX, ASCE, 342–349.

Tucker, M. J. (1991). *Waves in Ocean Engineering*. Ellis Horwood, 431 pp.

Uppala, S. M., Kållberg, P., Simmons, A., Andrae, U., Bechtold, V. D. C., Fiorino, M., Gibson, J., Haseler, J., Hernandez, A., Kelly, G., et al. (2005). The ERA-40 Re-Analysis. *Quarterly Journal of the Royal Meteorological Society: A journal of the atmospheric sciences, applied meteorology and physical oceanography*, 131(612):2961–3012. https://doi.org/10.1256/qj.04.176.

Van den Brink, H. and Können, G. (2011). Estimating 10000-year return values from short time series. *International Journal of Climatology*, 31(1):115–126. https://doi.org/10.1002/joc.2047.

Van Gelder, P. and Vrijling, J. (1999). On the distribution function of the maximum wave height in front of reflecting structures. *Proc. Int. Conf. on Coastal Structures*, Santander, Spain, American Society of Civil Engineers, 37–46.

Vanem, E., Huseby, A. B., and Natvig, B. (2012a). A Bayesian hierarchical spatio-temporal model for significant wave height in the North Atlantic. *Stochastic environmental research and risk assessment*, 26(5):609–632. https://doi.org/10.1007/s00477-011-0522-4.

Vanem, E., Natvig, B., and Huseby, A. B. (2012b). Modelling the effect of climate change on the wave climate of the world's oceans. *Ocean Science Journal*, 47(2):123–145. https://doi.org/10.1007/s12601-012-0013-7.

Vinoth, J. (2011). *Statistical analysis of global estimates of extreme wind speed and wave height*. PhD thesis, Faculty of Engineering and Industrial Sciences, Swinburne University of Technology, Melbourne. Available from Swinburne Theses Collection. http://hdl.handle.net/1959.3/201965.

Vinoth, J. and Young, I. (2011). Global estimates of extreme wind speed and wave height. *Journal of Climate*, 24(6):1647–1665. https://doi.org/10.1175/2010JCLI3680.1.

WAMDI Group (1988). The WAM model—A third generation ocean wave prediction model. *Journal of Physical Oceanography*, 18(12):1775–1810. https://doi.org/10.1175/1520-0485(1988)018<1775%3ATWMTGO>2.0.CO%3B2.

Wikle, C. K., Berliner, L. M., and Cressie, N. (1998). Hierarchical Bayesian space-time models. *Environmental and Ecological Statistics*, 5(2):117–154. https://doi.org/10.1023/A:1009662704779.

Wimmer, W., Challenor, P., and Retzler, C. (2006). Extreme wave heights in the North Atlantic from altimeter data. *Renewable Energy*, 31(2):241–248. https://doi.org/10.1016/j.renene.2005.08.019.

Young, I. (1993). An estimate of the Geosat altimeter wind speed algorithm at high wind speeds. *Journal of Geophysical Research: Oceans*, 98(C11):20275–20285. https://doi.org/10.1029/93JC02117.

Young, I. (1994). Global ocean wave statistics obtained from satellite observations. *Applied Ocean Research*, 16(4):235–248. https://doi.org/10.1016/0141-1187(94)90023-X.

Young, I. (1999). Seasonal variability of the global ocean wind and wave climate. *International Journal of Climatology: A Journal of the Royal Meteorological Society*, 19(9):931–950. https://doi.org/10.1002/(SICI)1097-0088(199907)19:9<931::AID-JOC412>3.0.CO;2-O.

Young, I., Babanin, A. V., and Zieger, S. (2013). The decay rate of ocean swell observed by altimeter. *Journal of Physical Oceanography*, 43(11):2322–2333. https://doi.org/10.1175/JPO-D-13-083.1.

Young, I. and Donelan, M. (2018). On the determination of global ocean wind and wave climate from satellite observations. *Remote sensing of environment*,

215:228–241. https://doi.org/10.1016/j.rse.2018.06.006.

Young, I. and Holland, G. (1996). *Atlas of the Oceans: Wind and Wave Climate*. Pergamon, 241 pp.

Young, I., Sanina, E., and Babanin, A. (2017). Calibration and cross validation of a global wind and wave database of altimeter, radiometer, and scatterometer measurements. *Journal of Atmospheric and Oceanic Technology*, 34(6):1285–1306. https://doi.org/10.1175/JTECH-D-16-0145.1.

Young, I., Vinoth, J., Zieger, S., and Babanin, A. V. (2012). Investigation of trends in extreme value wave height and wind speed. *Journal of Geophysical Research: Oceans*, 117(C00J06). https://doi.org/10.1029/2011JC007753.

Young, I., Zieger, S., and Babanin, A. V. (2011). Global trends in wind speed and wave height. *Science*, 332(6028):451–455. https://doi.org/10.1126/science.1197219.

Young, I., Zieger, S., and Babanin, A. V. (2015). Development and application of a global satellite database of wind and wave conditions. *Proceedings of the 34th International Conference on Ocean, Offshore and Arctic Engineering*, Newfoundland, Canada, American Society of Mechanical Engineers Digital Collection, 1–10.

Young, I. R. and Ribal, A. (2019). Multiplatform evaluation of global trends in wind speed and wave height. *Science*, 364(6440):548–552. https://doi.org/10.1126/science.aav9527.

Zeng, L. and Brown, R. A. (1998). Scatterometer observations at high wind speeds. *Journal of Applied Meteorology*, 37(11):1412–1420. https://doi.org/10.1175/1520-0450(1998)037<1412:SOAHWS>2.0.CO;2.

Zieger, S., Babanin, A. V., and Young, I. (2014). Changes in ocean surface wind with a focus on trends in regional and monthly mean values. *Deep Sea Research Part I: Oceanographic Research Papers*, 86:56–67. https://doi.org/10.1016/j.dsr.2014.01.004.

Zieger, S., Vinoth, J., and Young, I. (2009). Joint calibration of multiplatform altimeter measurements of wind speed and wave height over the past 20 years. *Journal of Atmospheric and Oceanic Technology*, 26(12):2549–2564. https://doi.org/10.1175/2009JTECHA1303.1.

Appendices

A.1 The effect of the data quality and the number of available data points on global extreme wave heights

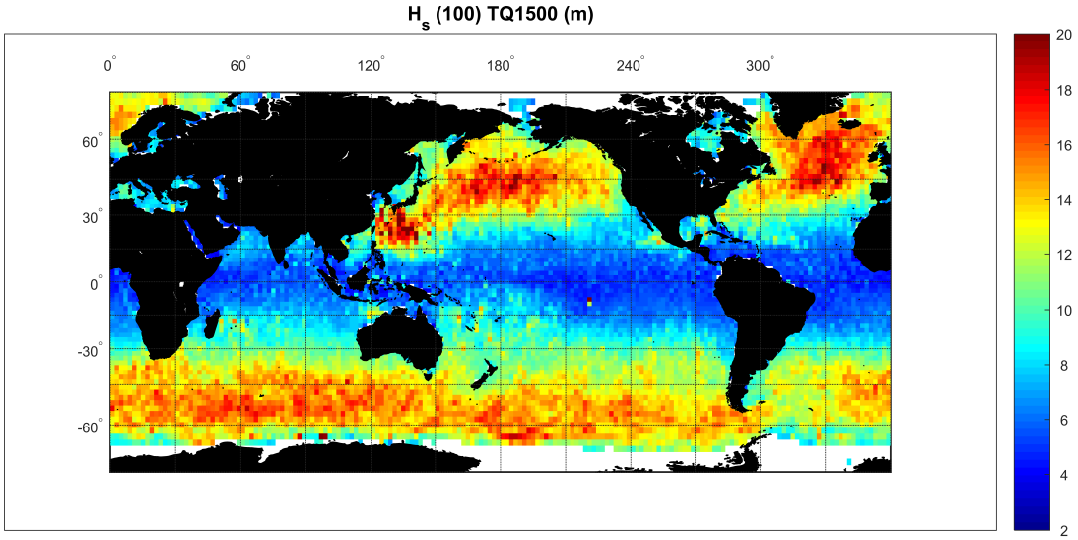

Figure A.1: Data quality test on global values of H_s^{100} obtained with a PoT analysis and a GPD distribution. Data obtained from altimeter data. Including more data with a lower quality level for EVA, leads to an increase of H_s^{100}-values in some region, for example in West Pacific north of the Equator. This is most probably due to a larger number of data points in the PDF fitting process rather than the quality of the data itself.

A.2 Threshold sensitivity test on global extreme wave heights

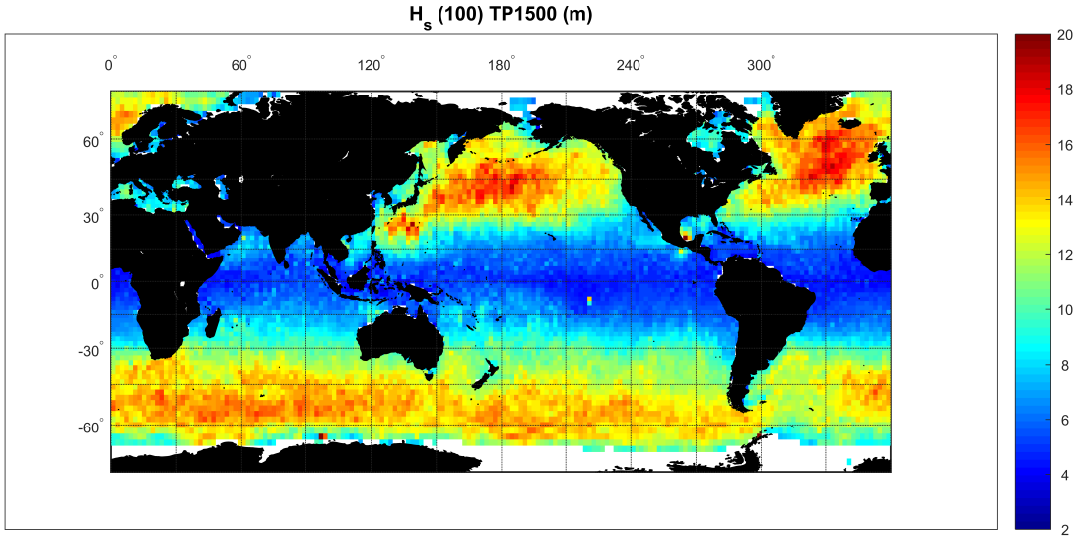

Figure A.2: Threshold sensitivity test (70th percentile) on global values of H_s^{100} obtained with a PoT analysis and a GPD distribution. Data obtained from altimeter data. The inclusion of more lower values of wave height, not surprisingly results in a general decrease in extreme values on the global scale. Notably, reducing the threshold reduces the extreme waves predicted in the tropical cyclone regions in South-East Asia.

A.3 Global distribution of extreme wind speed and extreme wave height with a GEV distribution

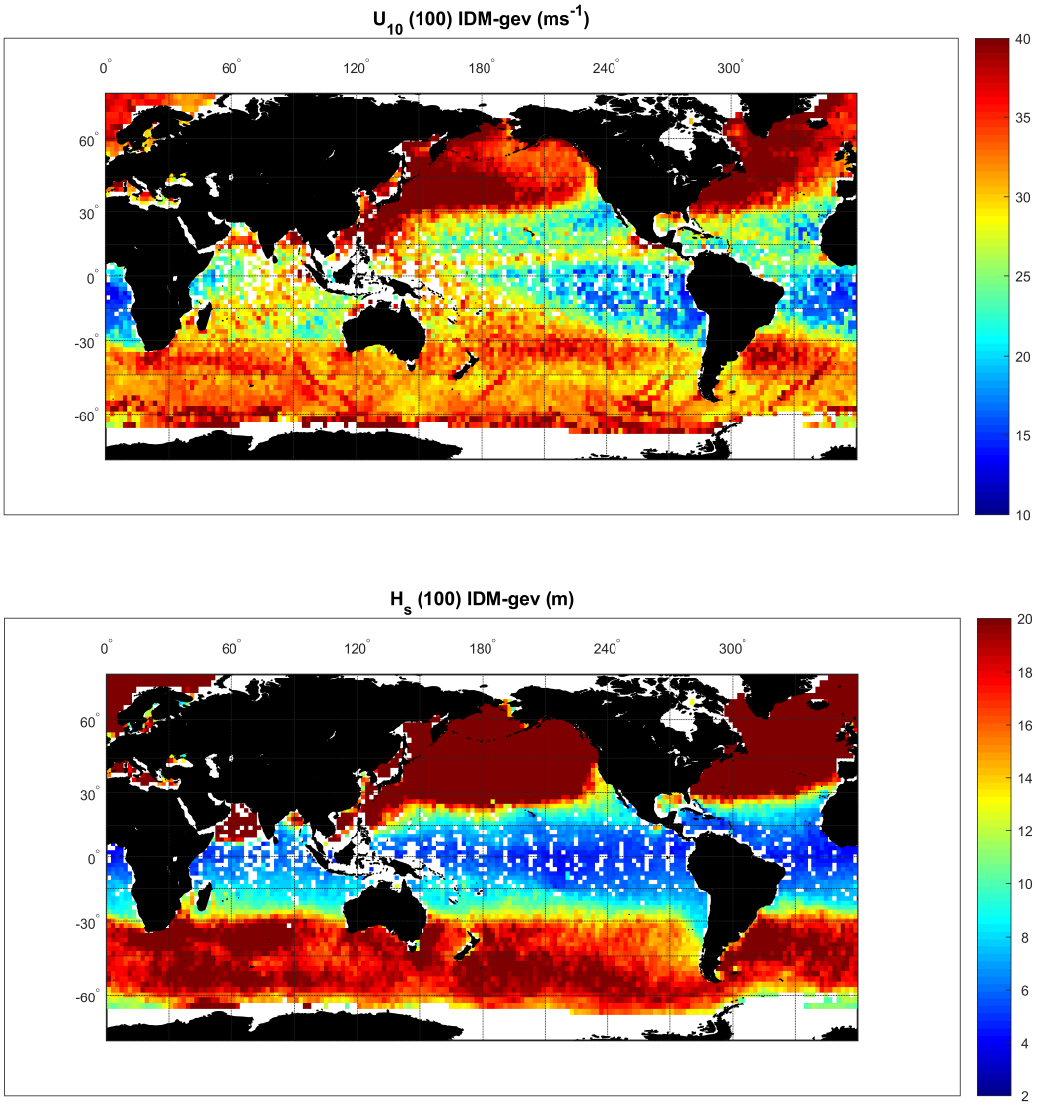

Figure A.3: Global values of (top) U_{10}^{100} (m s^{-1}) and (bottom)H_s^{100} (m) obtained with a GEV distribution. Data obtained from altimeter missions.

A.4 Global values of extreme wind speed and extreme wave height on a 0.75° x 0.75° spatial grid from ERAI data

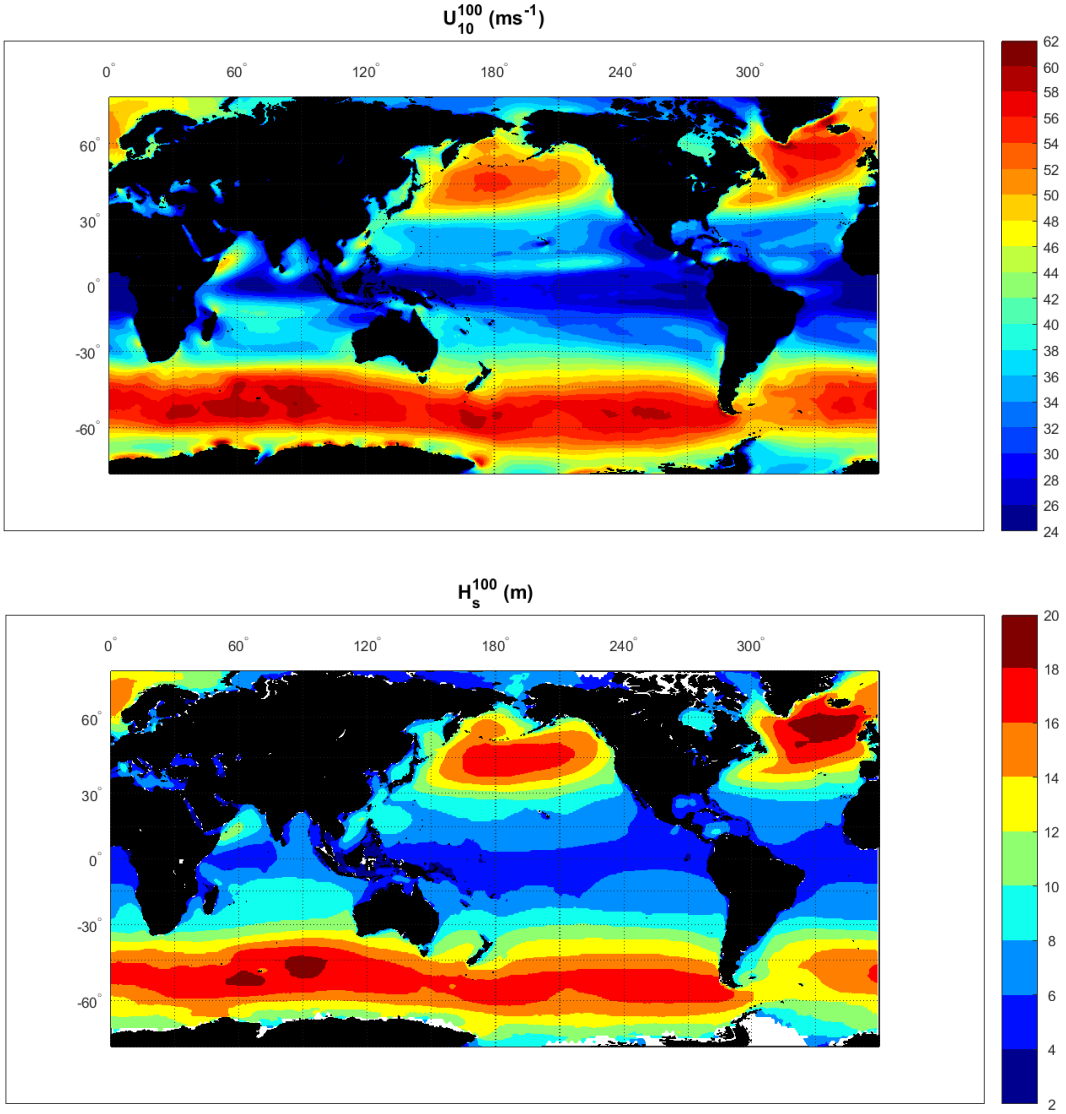

Figure A.4: Global values of (top) U_{10}^{100} and (bottom) H_s^{100} obtained with a IDM analysis and a Gumbel distribution on a 0.75° x 0.75° spatial grid. Data obtained from ERAI data.

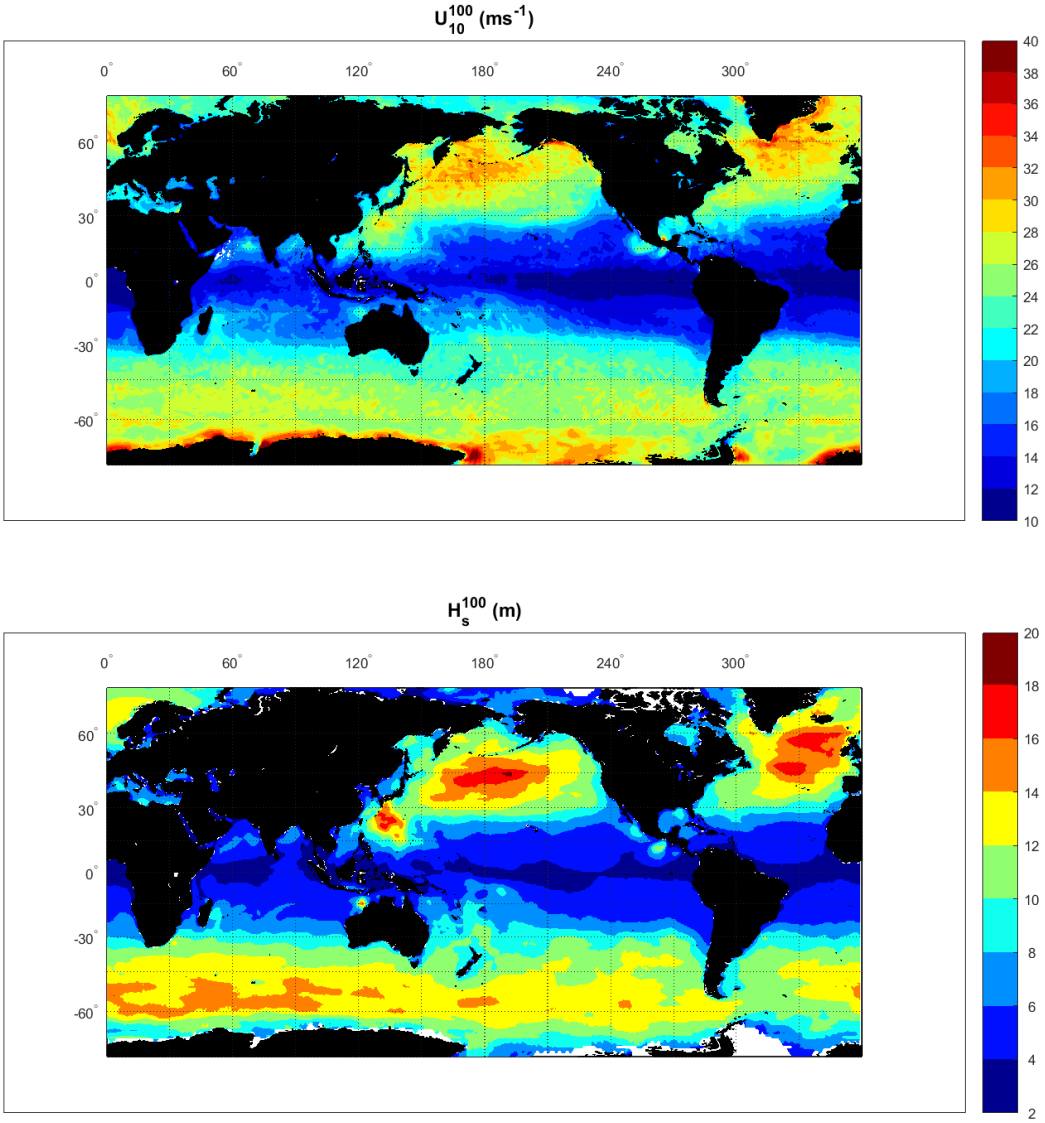

Figure A.5: Global values of (top) U_{10}^{100} and (bottom) H_s^{100} obtained with a PoT analysis and a GPD distribution on a 0.75° x 0.75° spatial grid. Data obtained from ERAI data.

A.5 Correlation ellipses calculated at specified locations for extreme wave heights

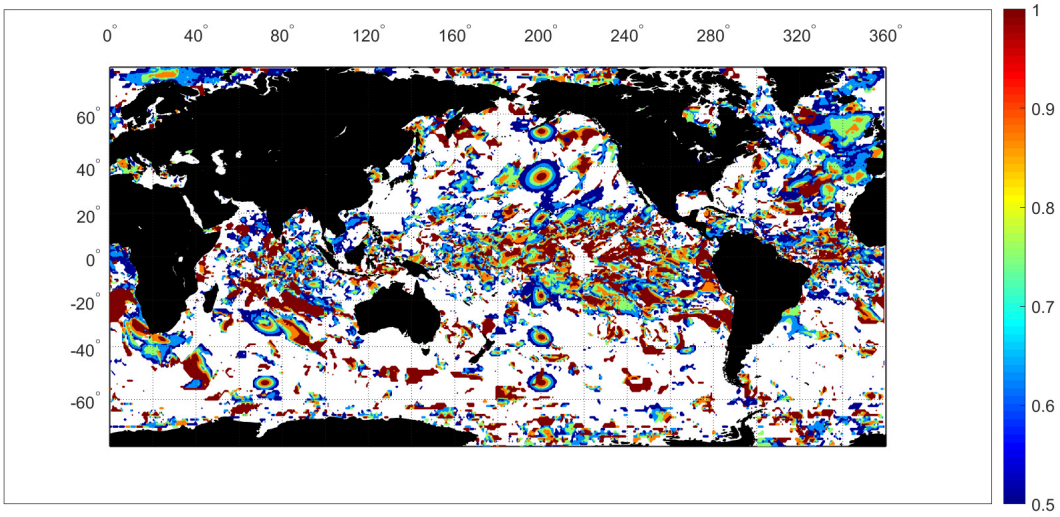

Figure A.6: Correlation ellipses calculated at specified locations [monthly means subtracted from the time series (H_s) greater than the 90th percentile) for application in (6.1)].

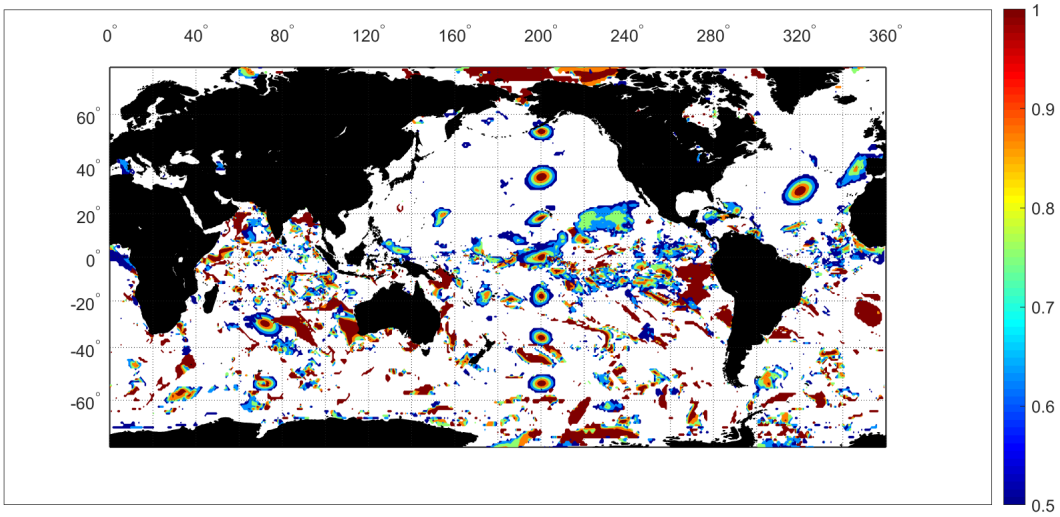

Figure A.7: Correlation ellipses calculated at specified locations [long-term means subtracted from the time series (H_s) greater than the 90th percentile) for application in (6.1)].

A.6 Wave climate tests for point AN (North Atlantic)

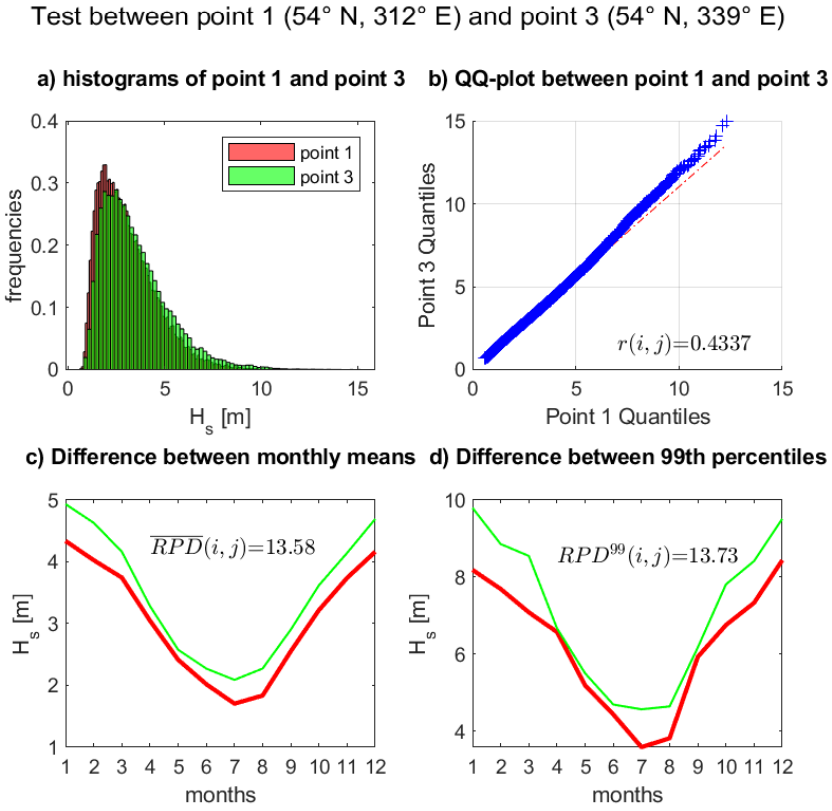

Test between point 1 (54° N, 312° E) and point 2 (45° N, 312° E)

a) histograms of point 1 and point 2 **b) QQ-plot between point 1 and point 2**

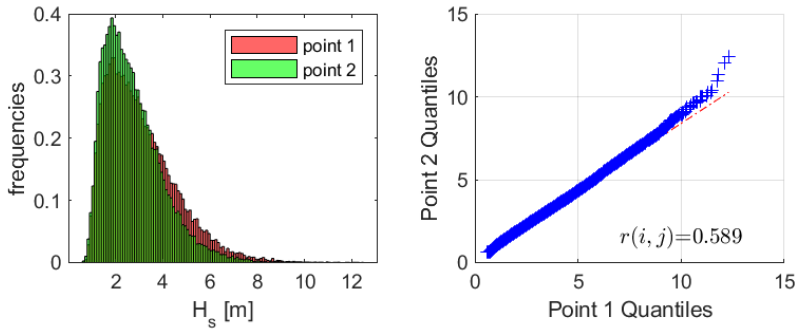

c) Difference between monthly means **d) Difference between 99th percentiles**

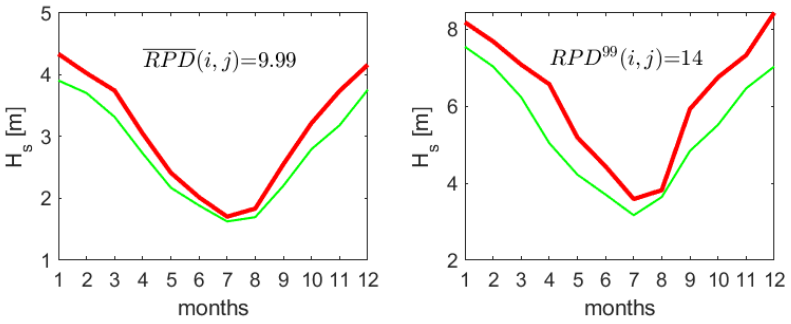

Test between point 1 (54° N, 312° E) and point 4 (45° N, 339° E)

a) histograms of point 1 and point 4 **b) QQ-plot between point 1 and point 4**

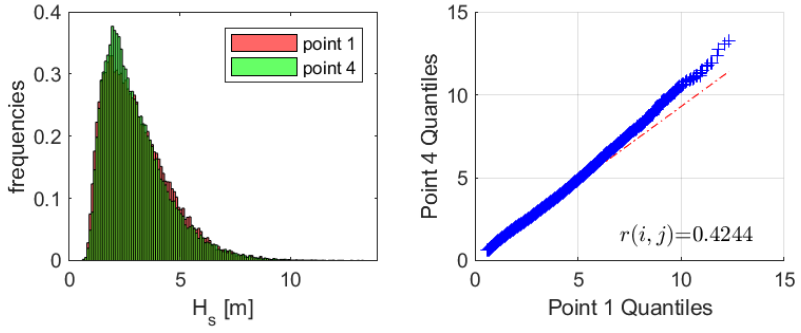

c) Difference between monthly means **d) Difference between 99th percentiles**

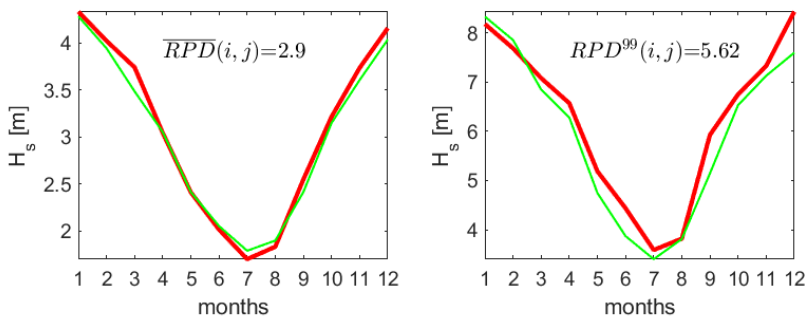

Test between point 2 (45° N, 312° E) and point 4 (45° N, 339° E)

a) histograms of point 2 and point 4 **b) QQ-plot between point 2 and point 4**

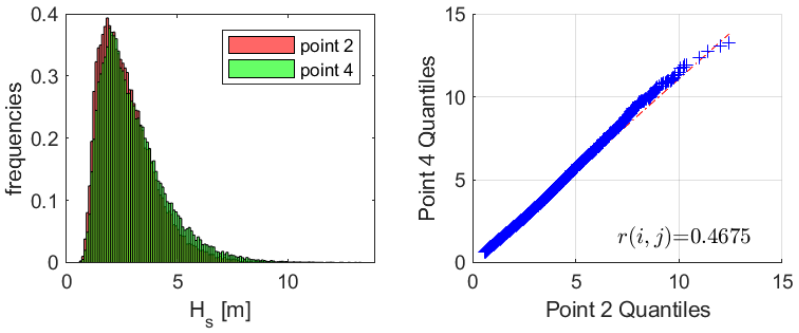

c) Difference between monthly means **d) Difference between 99th percentiles**

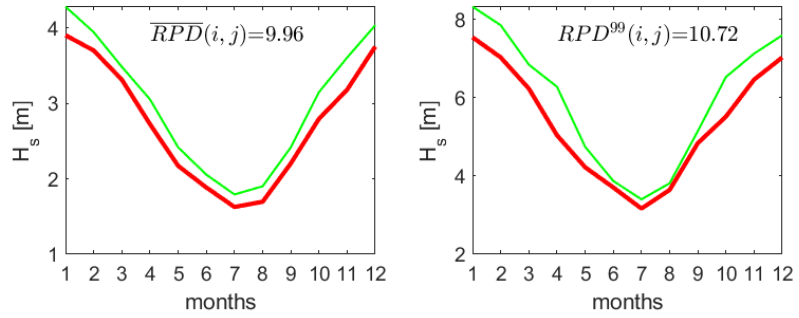

Test between point 2 (45° N, 312° E) and point 3 (54° N, 339° E)

a) histograms of point 2 and point 3 **b) QQ-plot between point 2 and point 3**

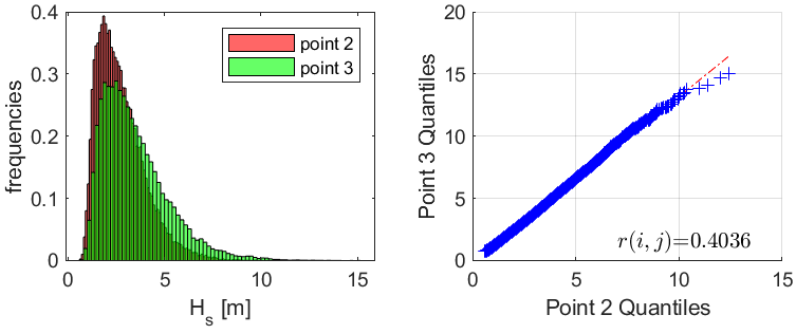

c) Difference between monthly means **d) Difference between 99th percentiles**

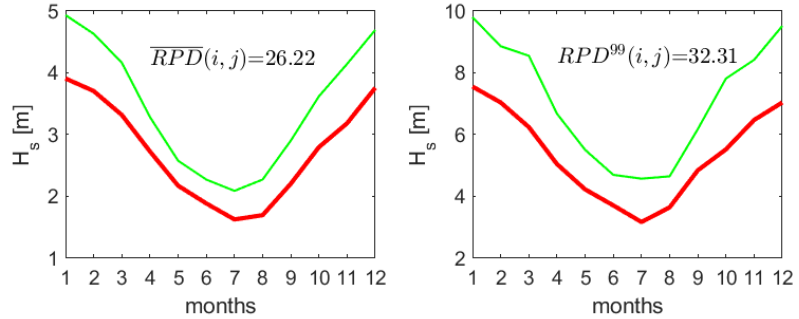

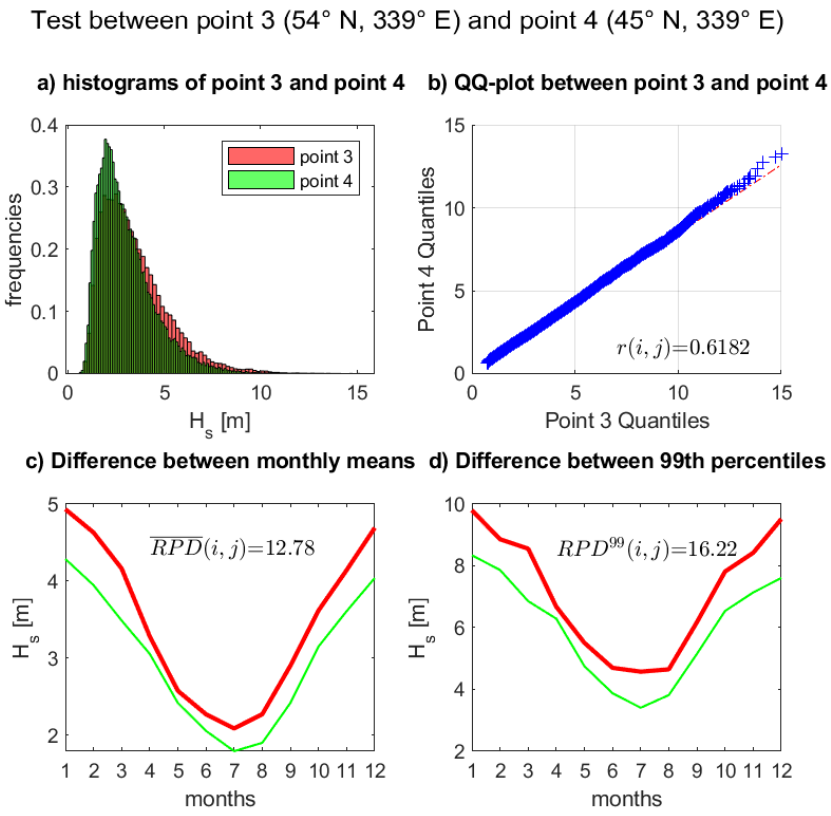

Figure A.8: Wave climate tests on a) histograms, b) QQ-plots and a least squares linear fit to the QQ data, c) monthly means, and d) 99th percentiles for region AN (North Atlantic). The tests are based on four selected points in this region as indicated. The correlation coefficient $[r(i,j)]$, the relative difference between monthly means $[\overline{RPD}(i,j)]$ and the 99th percentiles $[RPD^{99}(i,j)]$ are shown in the plot boxes b), c), and d). The full geographical extent of the region where the selected points lie is defined by Young (1999; Table 1).

A.7 Wave climate tests for region PN (North Pacific)

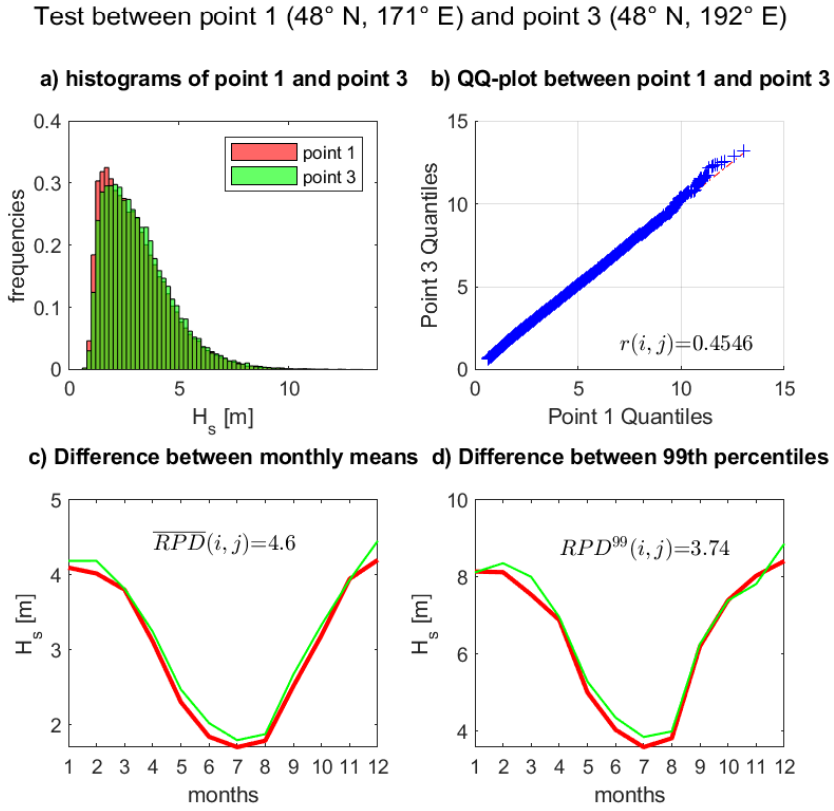

Test between point 1 (48° N, 171° E) and point 2 (39° N, 171° E)

a) histograms of point 1 and point 2 **b) QQ-plot between point 1 and point 2**

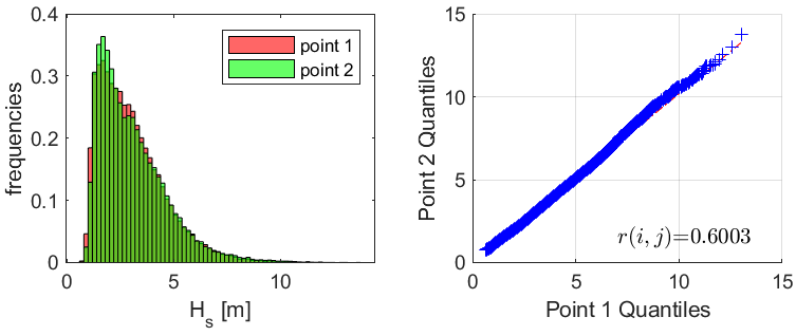

c) Difference between monthly means **d) Difference between 99th percentiles**

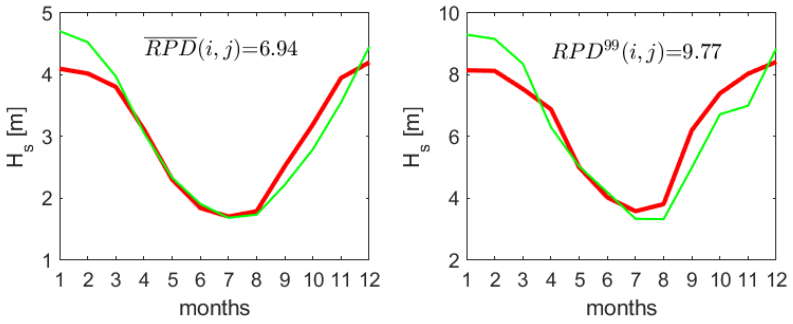

Test between point 1 (48° N, 171° E) and point 4 (39° N, 192° E)

a) histograms of point 1 and point 4 **b) QQ-plot between point 1 and point 4**

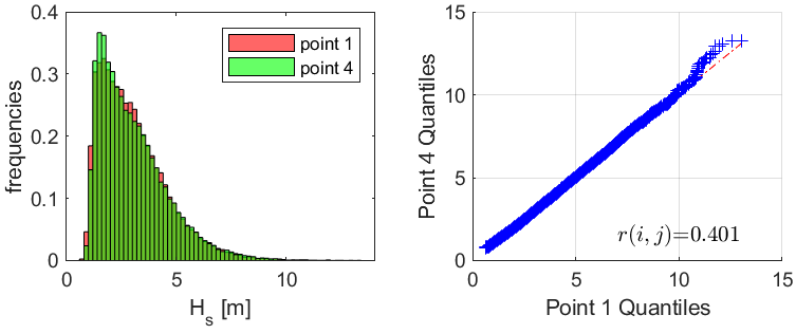

c) Difference between monthly means **d) Difference between 99th percentiles**

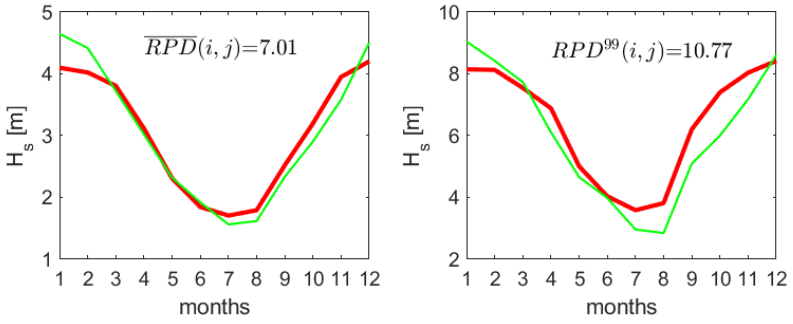

Test between point 2 (39° N, 171° E) and point 4 (39° N, 192° E)

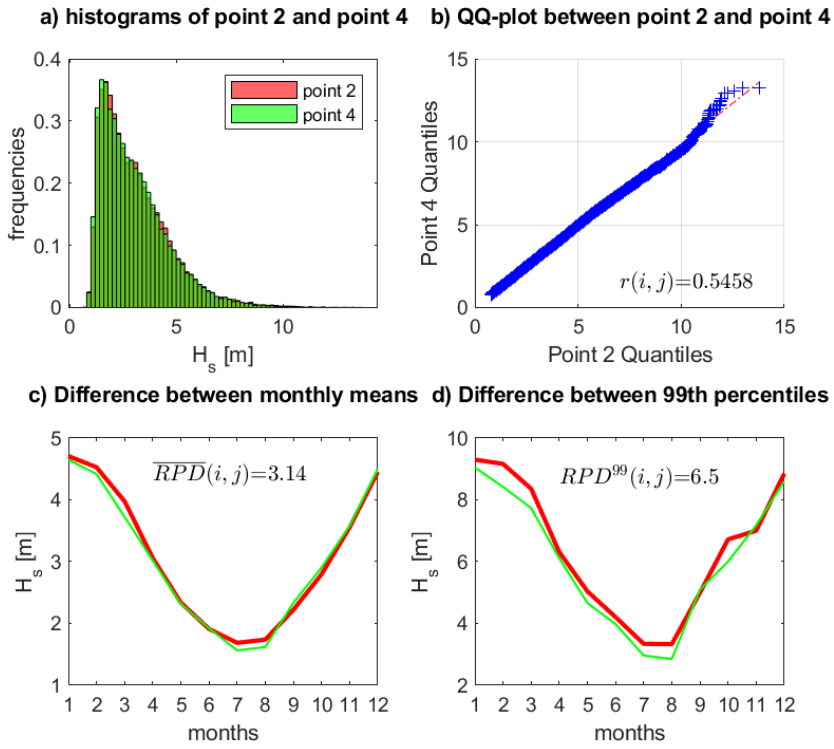

Test between point 2 (39° N, 171° E) and point 3 (48° N, 192° E)

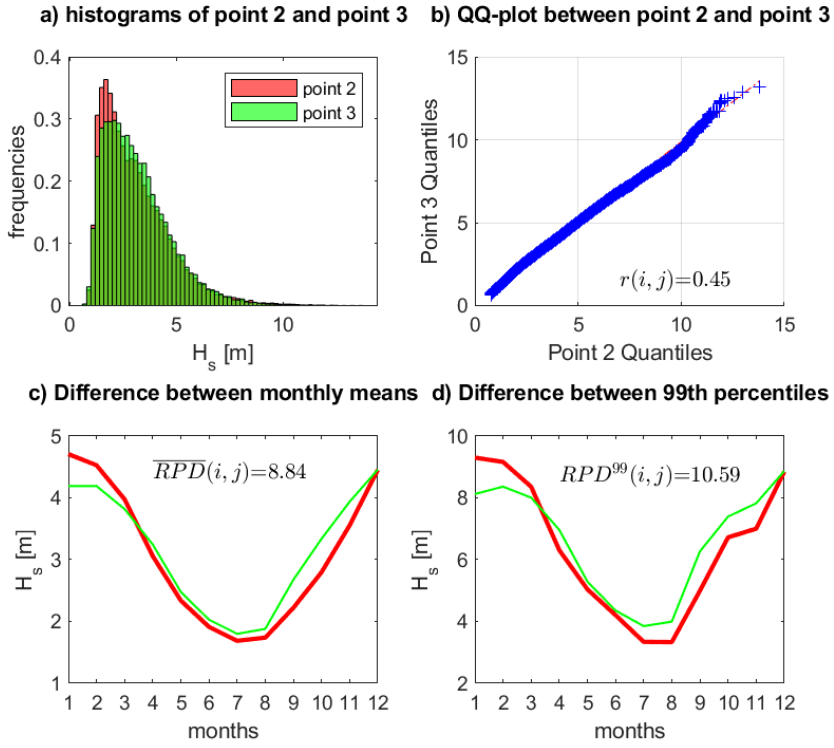

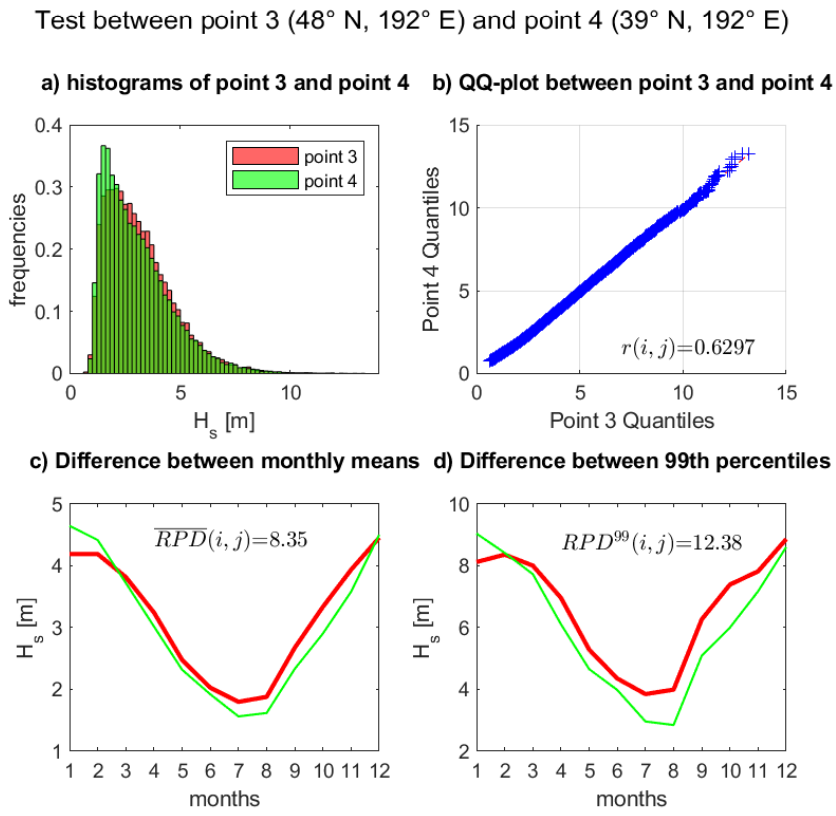

Figure A.9: Wave climate tests on a) histograms, b) QQ-plots and a least squares linear fit to the QQ data, c) monthly means, and d) 99th percentiles for region PN (North Pacific). The tests are based on four selected points in this region as indicated. The correlation coefficient $[r(i,j)]$, the relative difference between monthly means $[\overline{RPD}(i,j)]$ and the 99th percentiles $[RPD^{99}(i,j)]$ are shown in the plot boxes b), c), and d). The full geographical extent of the region where the selected points lie is defined by Young (1999; Table 1).

A.8 Wave climate tests for point SP [Southern Ocean (Pacific)]

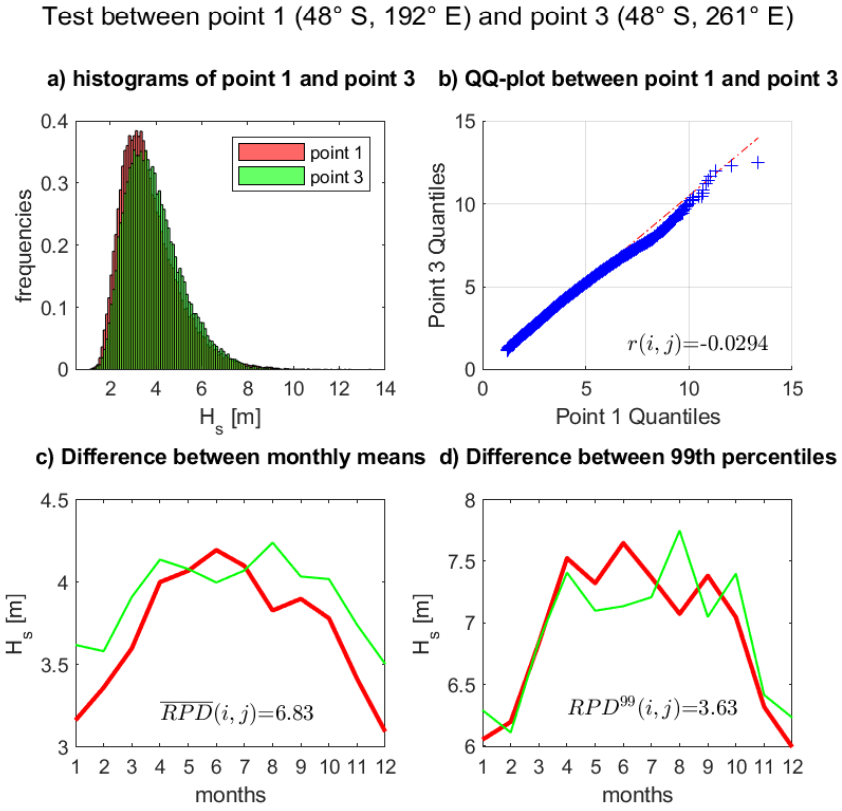

Test between point 1 (48° S, 192° E) and point 2 (57° S, 192° E)

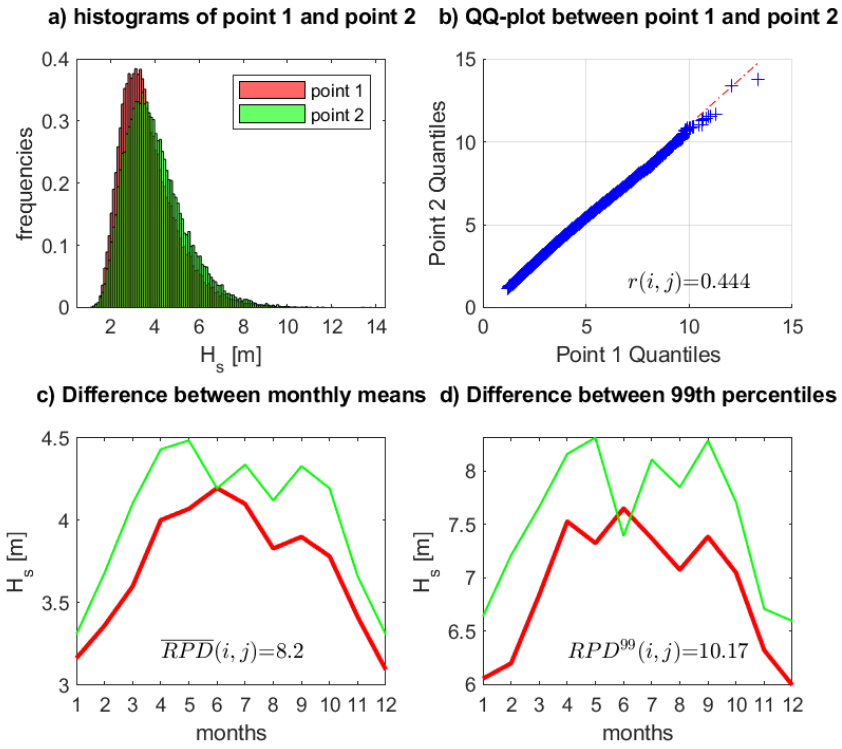

Test between point 1 (48° S, 192° E) and point 4 (57° S, 261° E)

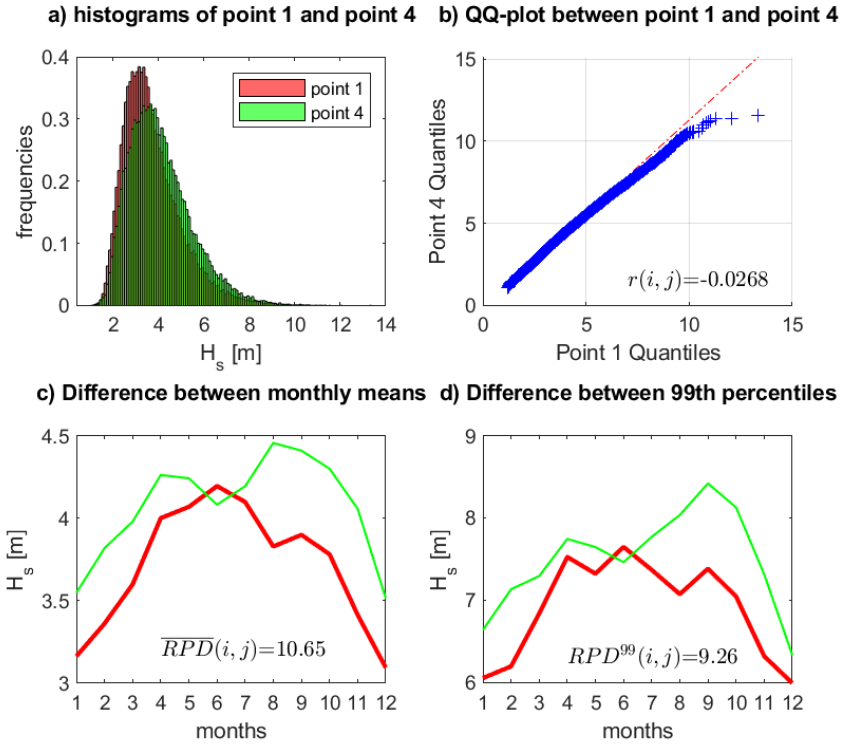

Test between point 2 (57° S, 192° E) and point 4 (57° S, 261° E)

a) histograms of point 2 and point 4 **b) QQ-plot between point 2 and point 4**

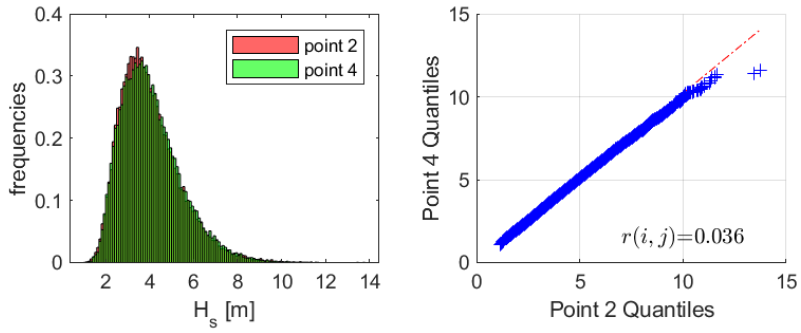

c) Difference between monthly means **d) Difference between 99th percentiles**

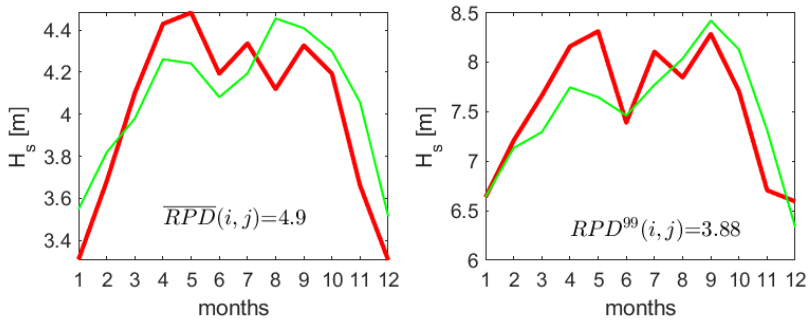

Test between point 2 (57° S, 192° E) and point 3 (48° S, 261° E)

a) histograms of point 2 and point 3 **b) QQ-plot between point 2 and point 3**

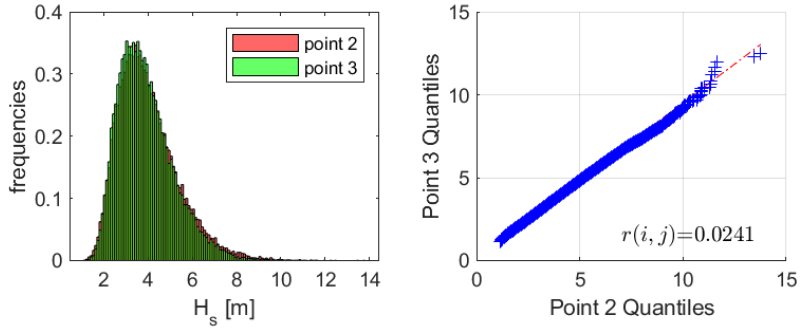

c) Difference between monthly means **d) Difference between 99th percentiles**

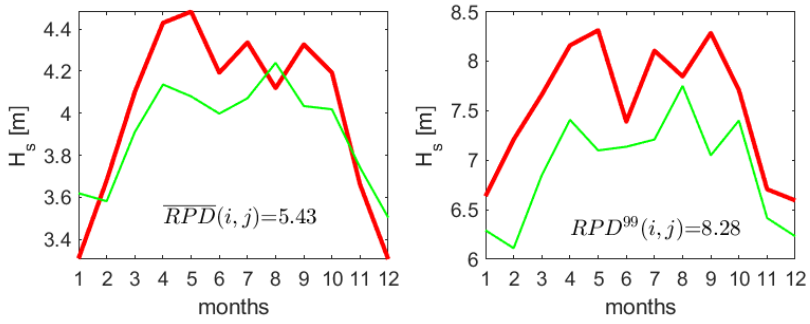

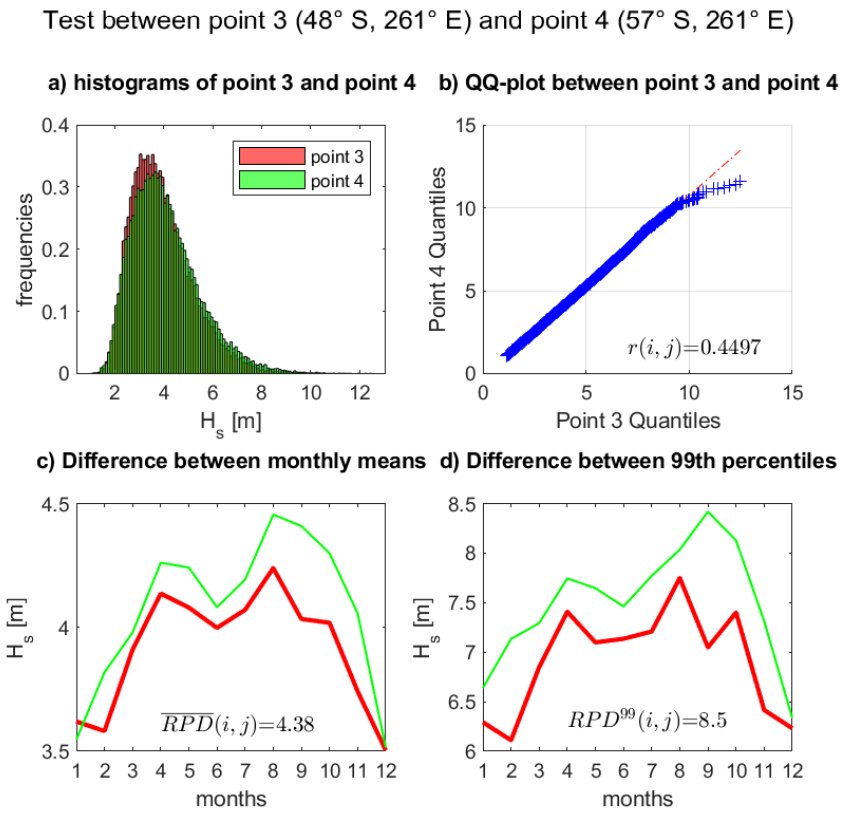

Figure A.10: Wave climate tests on a) histograms, b) QQ-plots and a least squares linear fit to the QQ data, c) monthly means, and d) 99th percentiles for region SP [Southern Ocean (Pacific)]. The tests are based on four selected points in this region as indicated. The correlation coefficient $[r(i,j)]$, the relative difference between monthly means $[\overline{RPD}(i,j)]$ and the 99th percentiles $[RPD^{99}(i,j)]$ are shown in the plot boxes b), c), and d). The full geographical extent of the region where the selected points lie is defined by Young (1999; Table 1).

A.9 Wave climate tests for point SI [Southern Ocean (Indian)]

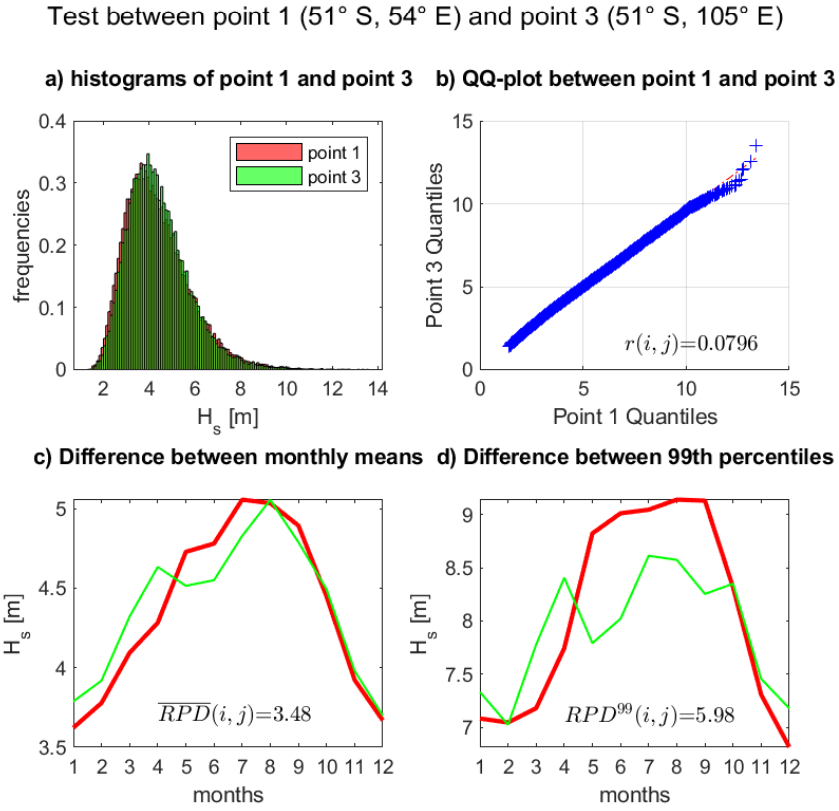

Test between point 1 (51° S, 54° E) and point 2 (58.5° S, 54° E)

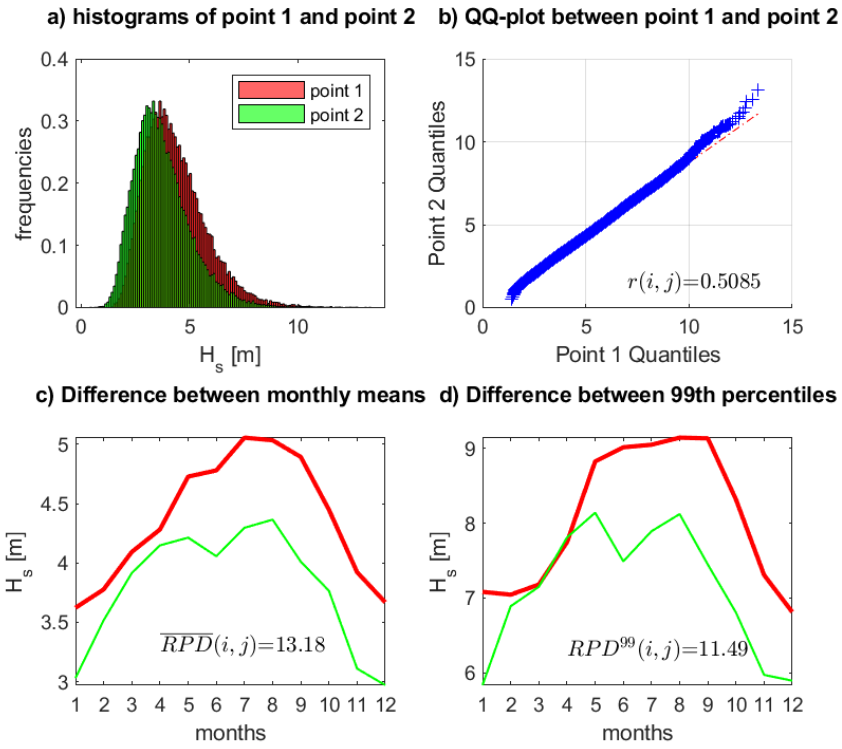

Test between point 1 (51° S, 54° E) and point 4 (58.5° S, 105° E)

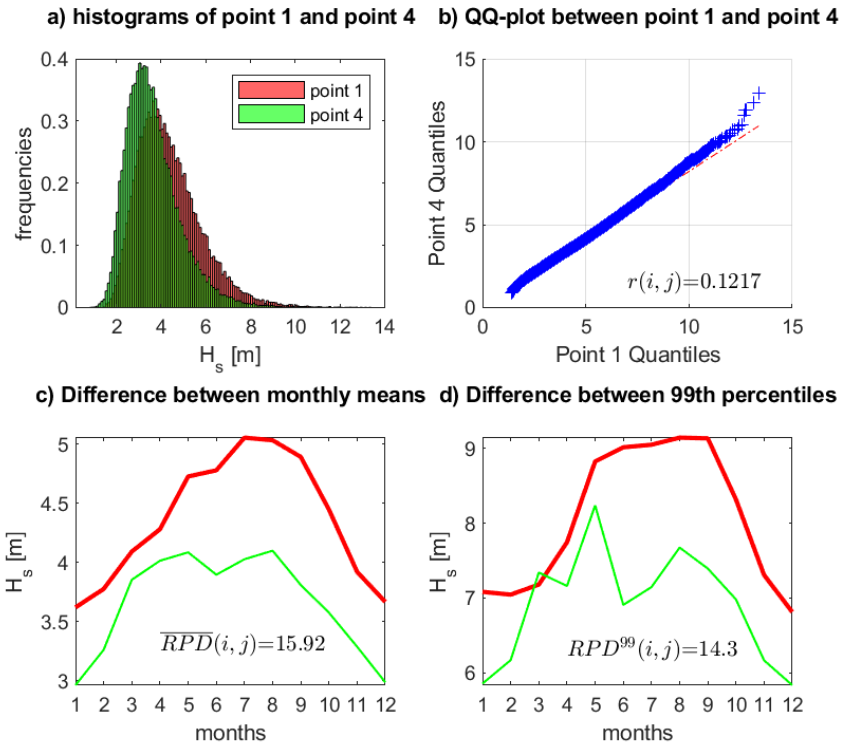

Test between point 2 (58.5° S, 54° E) and point 4 (58.5° S, 105° E)

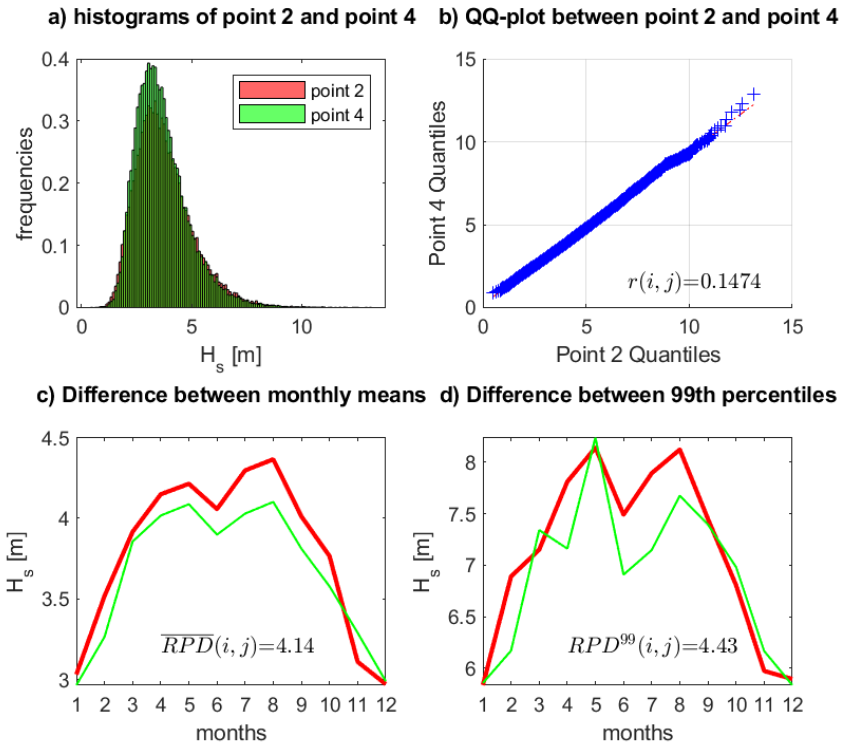

Test between point 2 (58.5° S, 54° E) and point 3 (51° S, 105° E)

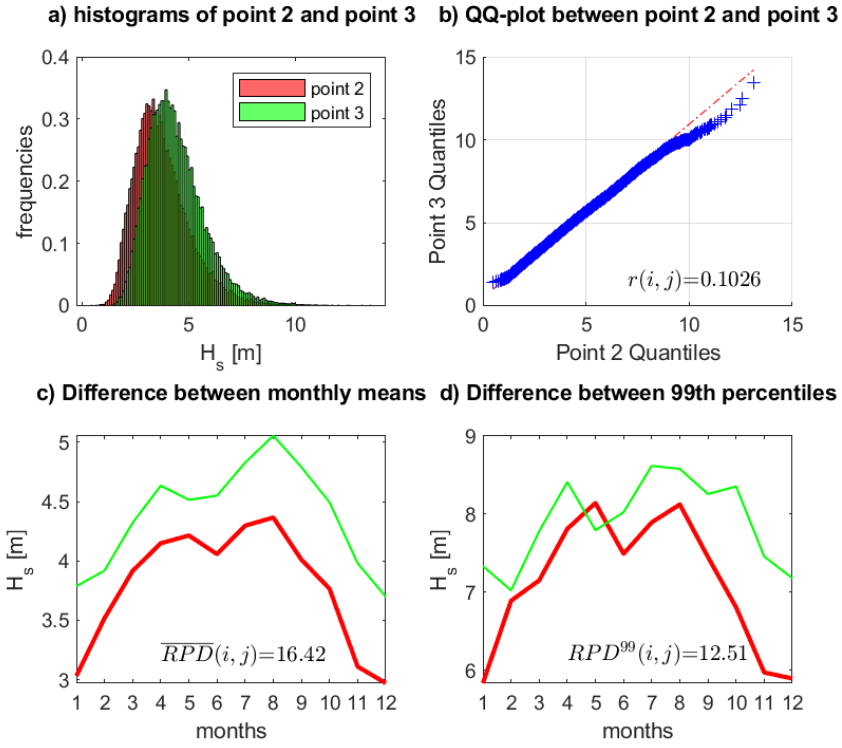

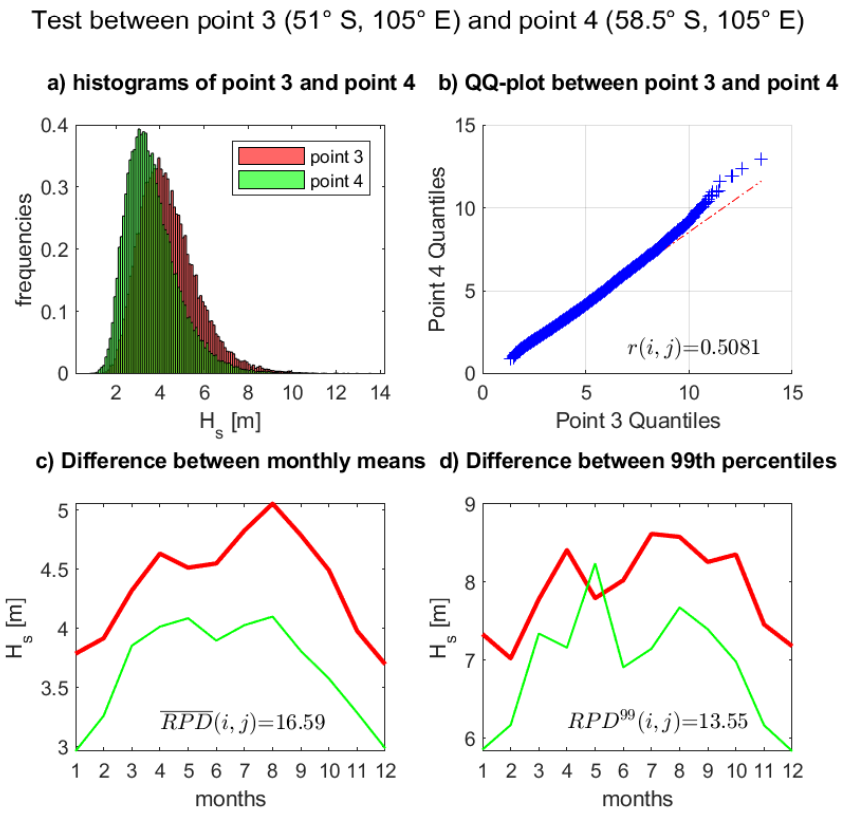

Figure A.11: Wave climate tests on a) histograms, b) QQ-plots and a least squares linear fit to the QQ data, c) monthly means, and d) 99th percentiles for region SI [Southern Ocean (Indian)]. The tests are based on four selected points in this region as indicated. The correlation coefficient $[r(i,j)]$, the relative difference between monthly means $[\overline{RPD}(i,j)]$ and the 99th percentiles $[RPD^{99}(i,j)]$ are shown in the plot boxes b), c), and d). The full geographical extent of the region where the selected points lie is defined by Young (1999; Table 1).

A.10 Wave climate tests for point ISTS (South Subtropical Indian)

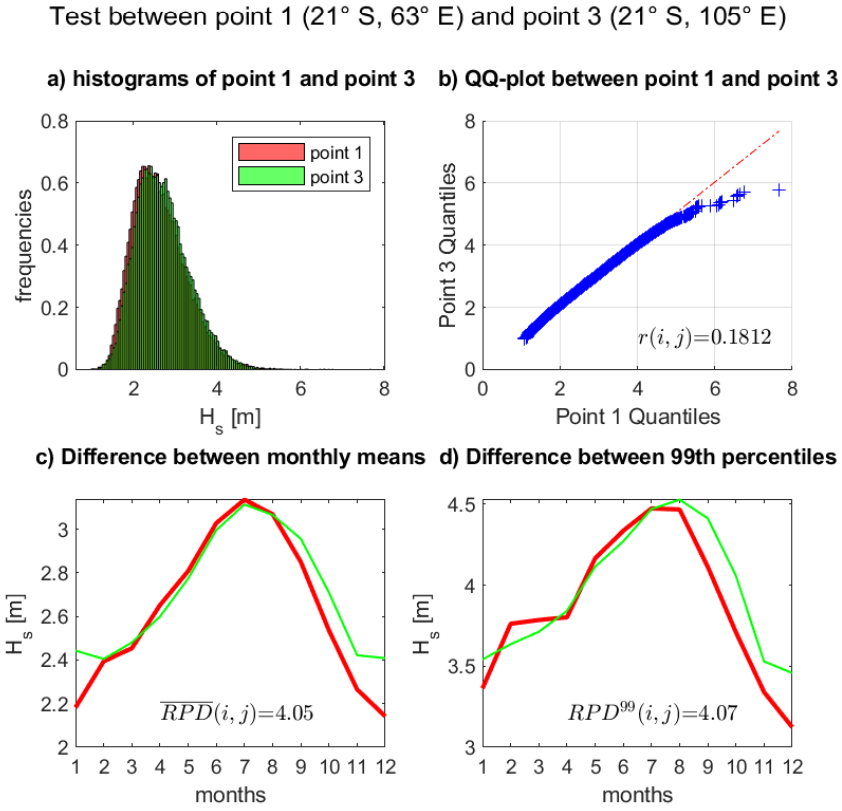

Test between point 1 (21° S, 63° E) and point 2 (33° S, 63° E)

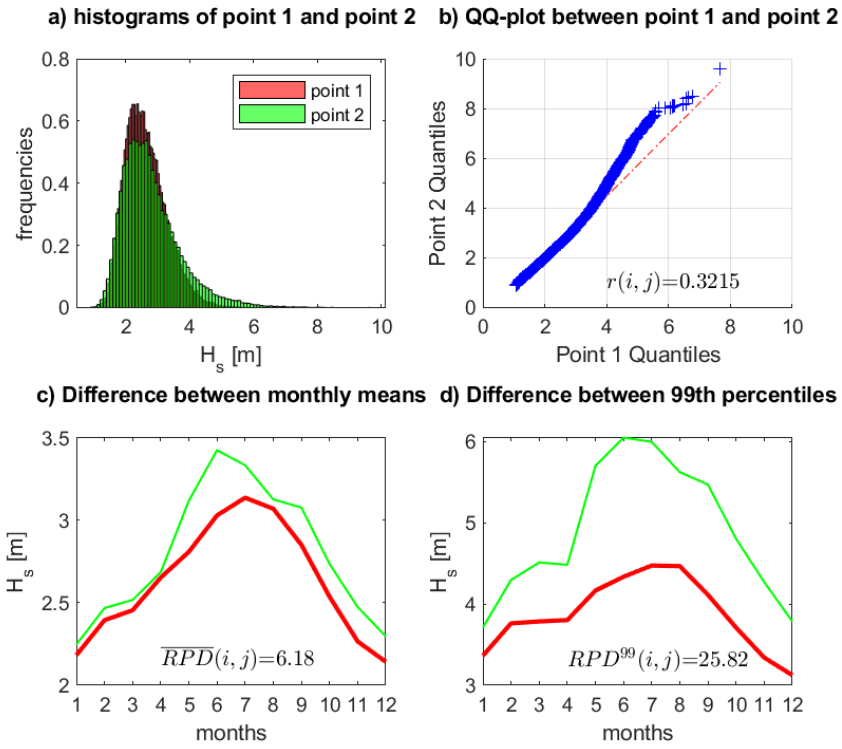

Test between point 1 (21° S, 63° E) and point 4 (33° S, 105° E)

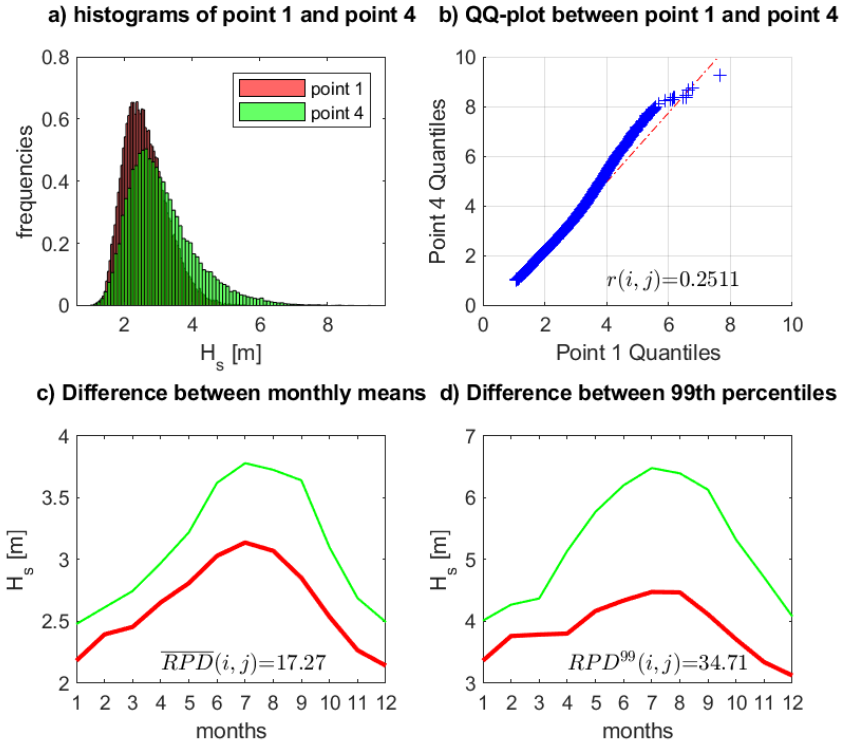

Test between point 2 (33° S, 63° E) and point 4 (33° S, 105° E)

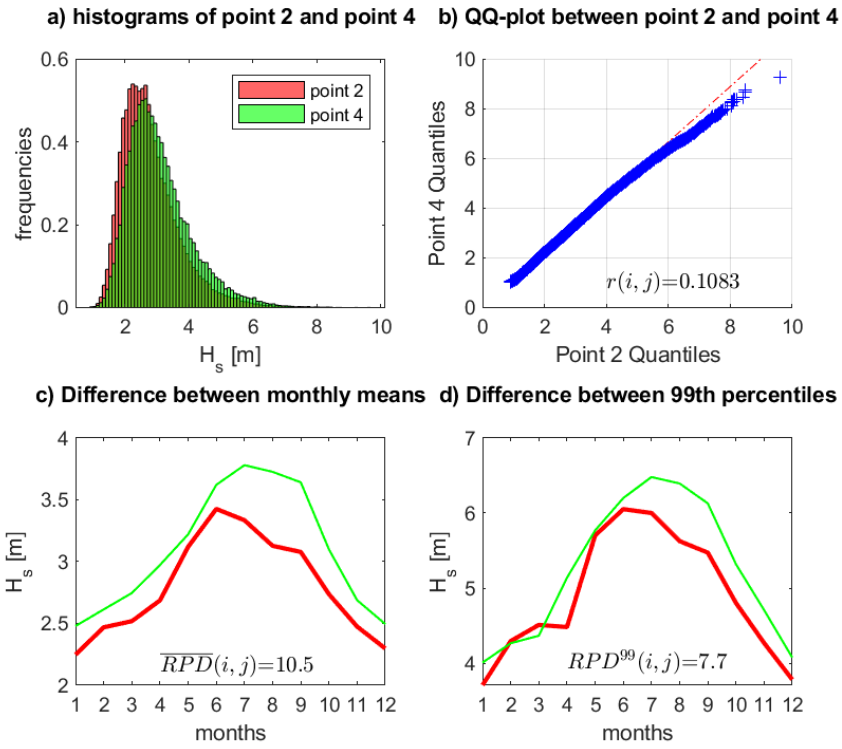

Test between point 2 (33° S, 63° E) and point 3 (21° S, 105° E)

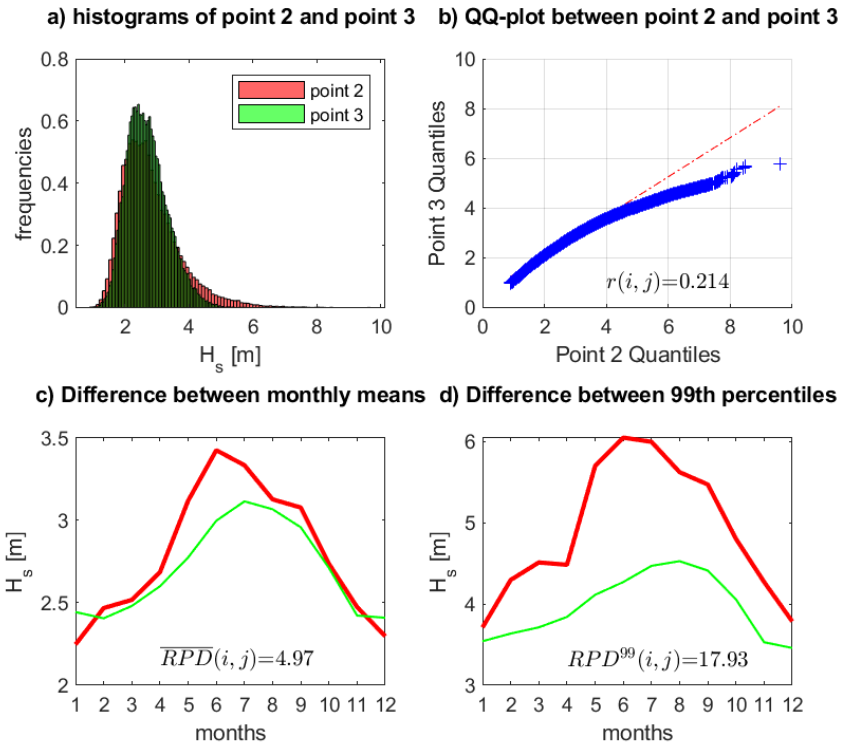

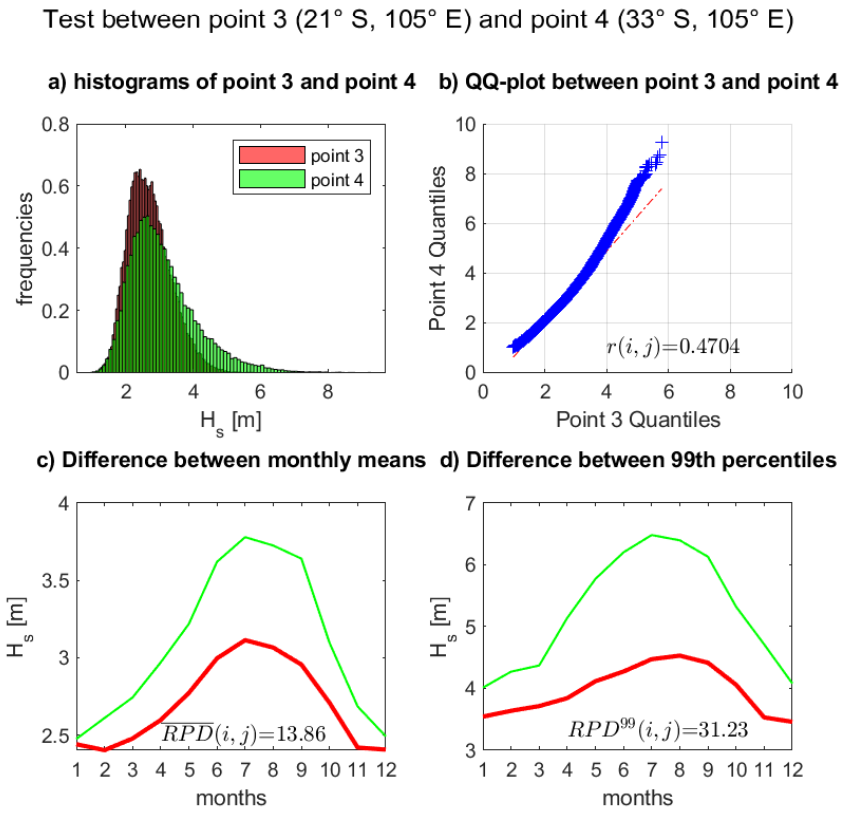

Figure A.12: Wave climate tests on a) histograms, b) QQ-plots and a least squares linear fit to the QQ data, c) monthly means, and d) 99th percentiles for region ISTS (South Subtropical Indian). The tests are based on four selected points in this region as indicated. The correlation coefficient $[r(i,j)]$, the relative difference between monthly means $[\overline{RPD}(i,j)]$ and the 99th percentiles $[RPD^{99}(i,j)]$ are shown in the plot boxes b), c), and d). The full geographical extent of the region where the selected points lie is defined by Young (1999; Table 1).

A.11 Global values of extreme wave height on a 1.5° x 1.5° spatial grid with a PoT analysis using ERAI data

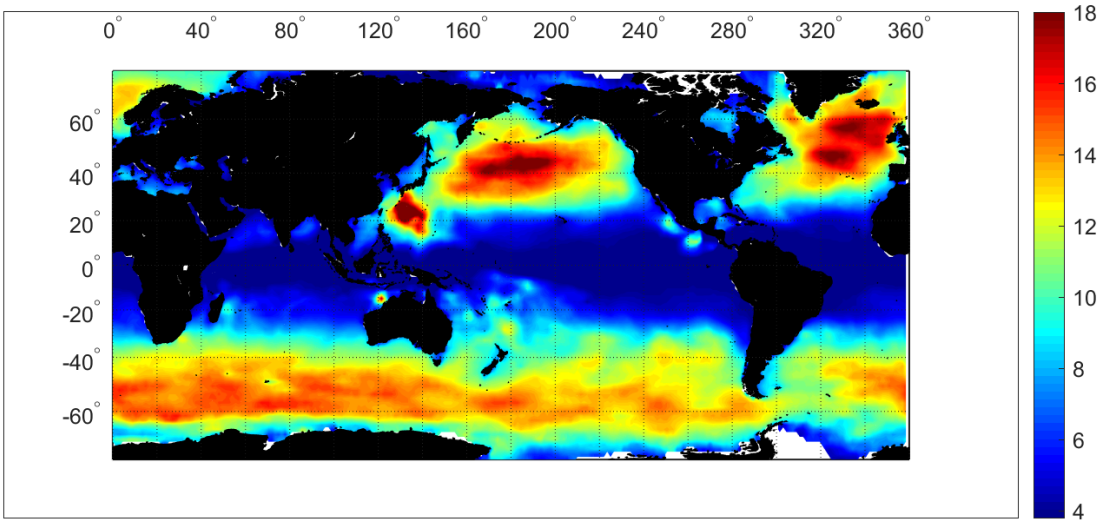

Figure A.13: Global values of H_s^{100} obtained with a PoT analysis and a GPD distribution on a 1.5° x 1.5° spatial grid. Data obtained from ERAI data.